Identification of Civil Structural Parameters Using the Extended Kalman Filter

by

Kevin Foun

B.S., Civil Engineering
National Cheng Kung University, 2007

Submitted to the Department of Civil and Environmental Engineering
in partial fulfillment of the requirements for the degree of

Master of Science in Civil and Environmental Engineering

at the

MASSACHUSETTS INSTITUTE OF TECHNOLOGY

February 2010

Author .....
Department of Civil and Environmental Engineering
December 21, 2009

Certified by .....
Jerome J. Connor
Professor of Civil and Environmental Engineering
Thesis Supervisor

Accepted by .....
Daniele Veneziano
Chairman, Departmental Committee for Graduate Students

Identification of Civil Structural Parameters Using the Extended Kalman Filter

by

Kevin Foun

Submitted to the Department of Civil and Environmental Engineering
on December 21, 2009, in partial fulfillment of the
requirements for the degree of
Master of Science in Civil and Environmental Engineering

Abstract

In the context of civil and industrial structures, structural control and damage detection have recently become an area of great interest. The safety of a structure is always the most important issue for structural engineers, and to achieve this goal, the discipline of Structural Health Monitoring (SHM) was introduced. SHM records real-time information concerning structural conditions and performances. In order to evaluate the health conditions of structures, identifying the structural parameters is needed. Research activities of this area are increasing due to the availability of computation and wireless technologies.

The objective of this thesis is to evaluate the tracking ability of the Kalman filter for identifying civil structural parameters based on measured vibration data which usually are earthquake accelerations. For linear elastic structures, the ordinary Kalman filter was used, but for nonlinear elastic structures, we implemented the extended Kalman filter. For simulating damage occurrence in structures, a sudden change of stiffness was introduced, and an adaptive extended Kalman filter was utilized to estimate the time-varying parameters. In this thesis, linear and nonlinear structures with single-degree-of-freedom and multi-degree-of-freedom were simulated. Measurements having different levels of white noise were considered in order to evaluate the effects of noise on parametric estimations. In addition, the impacts of different levels of noise covariance were also discussed. Simulation results from different structural models were presented to demonstrate the effectiveness of the Kalman filter.

Thesis Supervisor: Jerome J. Connor
Title: Professor of Civil and Environmental Engineering

"The best and most beautiful things in the world cannot be seen or even touched.

They must be felt with the heart."

Helen Keller

Acknowledgments

My research advisor, Prof. Jerome J. Connor, is not simply a teacher but a friend to me. He certainly provided invaluable advice to my thesis work, and his experiences regarding research and life also influenced me deeply. He has the passion of an innovator, a mentor, and an educator. It is a pleasure to have Prof. Connor as my advisor.

I am also grateful to have Prof. Franz-Josef Ulm as my academic advisor. He always gave me helpful instructions on selecting classes and assistances on finical aid issues. I deeply appreciate his kind help during my studies at MIT.

My education at MIT was made possible by the Hao Ran Foundation from Taiwan and the Dickson fellowship from the CEE Department at MIT. I am extremely lucky to be funded by them and to have the chance to study at this amazing place.

I would also like to thank my group buddies: Cory, Pierre F., Pierre G., Rory, Simon, and Todd. They always built a joyful atmosphere in each group meeting. Meanwhile, I am glad to have André and Lei in helping me edit this thesis.

During my studies at MIT, my family gave me the biggest support with encouragement, patience, and unwavering love. Although I was far away from my home, my heart was always fulfilled by their endless care. In addition, I owe my greatest thanks to Choi Hong, who always stands beside me.

Dedicated to my mother, who raised me on her own.

Yuh-Ruey Wang

Contents

List of Figures

List of Tables

Chapter 1

Introduction

The main functionality of civil structures is to provide a safe place for human beings in which people can be protected from the natural hazards such as storms, hurricanes, and floods. However, structures may be damaged or even collapse due to these external forces. Therefore, monitoring the performances of structures in real-time is essential for structural maintenance and the protection of human lives. This thesis presents the Kalman filter's ability to estimate structural parameters, which indicate the structural integrity, for evaluating the conditions of a structure. In this chapter, a brief introductory background of the main research of this thesis will be stated along with the motivation, objectives, and thesis outline.

1.1 Damage Prognosis

Preventing structures from reaching their operational limits so that they can retain a safe condition with expected performances is the goal of all structural engineering. However, structures experience extreme events such as earthquakes and hurricanes. The ability to detect damage in structures at an early stage can not only cut down the maintenance costs but also avoid loss of human life. Research related to damage detection has always been active. The traditional approach is visual inspection which relies upon the human eye and human memory. With the understanding of many physical phenomena, nondestructive testing techniques which rely upon the applica-

tion of electromagnetics, radiation, capillary action, ultrasonics, etc. were developed. To date, due to the development of sensing and computation technologies, monitoring the whole lifespan of a structure in real-time is a recent trend in damage prognosis. The approaches stated above are discussed as follows:

1.1.1 Visual Inspection

Visual inspection mainly relies on human eye and human memory when conducting damage detection [7]. In order to overcome the human physical limits, technical devices such as borescopes and fiberscopes were developed to enhance the performances on visual inspection [7, 33]. Although proper optical devices augment human eyesight, accurate results still depended on well-trained technician and suitable operation conditions.

Borescopes are devices that can remotely view surfaces or cavities and allow people to keep away from possible harmful substances. They consist of a rigid or flexible optical viewing tube with objective lens and eyepiece lens on each end. Borescopes provide clear images, and they are much cheaper than fiberscopes. As a result, borescopes have gained wide use throughout the industry. In civil engineering aspects, borescopes are used in inspection of cavity walls, beam ends, girder sections, etc.

Fiberscopes improve the deficiency of borescopes with a smaller size and ability to access deeper area. Fiberscopes are composed of two fiber optic bundles within a flexible tube. The fiber bundles are composed of tens of thousands of glass fibers which transduce the image information. The fiberscopes are usually equipped with video record system for providing a longspan and real-time inspection. Fiberscopes are mostly used in medicine, aerospace, and ship industries.

Holography can also be used for inspection of structural flaws. The holograms record the information of electromagnetic waves such as amplitudes and phases; and the flaws can be detected by comparing the two holograms (one from the original state; another from the damaged state). Producing holograms needs to utilize laser lights and the process to record electromagnetic properties is very sensitive to external disturbance; therefore, a vibration-free and light-free environment is required. In

this regard, holography is not a suitable method for detecting damage of large scale structures.

With the rise of digital technology, structures can be monitored by digital cameras, but it is only suitable for small areas. A digital camera records images of a particular area at different time intervals, and the possible damage location can be indicated by comparing these images.

A common drawback of the visual inspection methods is that all devices have their own limitations and that makes it impossible to detect all the flaws. In addition, visual inspection is highly time and labor consuming; therefore, more effective and systematic techniques were developed to have better performances on damage detection.

1.1.2 Nondestructive Testing

Nondestructive testing (NDT) is a method used to evaluate the mechanical properties of materials and examine the potential flaws or cracks in materials without alteration of the portion being tested. The development of NDT can be traced back to late 19th century. The main NDT methods will be presented in the order of development as fellows [46].

Radiography is one of the earliest NDT techniques used for medical and industrial applications. Radiographys are shadow images providing two dimensional information and they are obtained using radiation penetration such as X-rays and γ -rays. The contrast of the images is caused by different levels of absorption of radiation. The flaws, discontinuities, chemical composition, dimensions, densities, etc. are the possible reason leading the contrast, and people can detect damage or obtain materials properties from the contrast. One concerned issue of radiography is the safety during the operations. The U.S. Nuclear Regulatory Commission provides proper procedures to manipulate radiography, and radiographers have to receive complete training on radiographic techniques.

Researchers have already discovered that the magnetic fields of a magnet can be displayed by filing iron powder. Magnetic particle inspection was developed based on

this concept and has been applied to industry. The flaws and cracks in a magnetized object disturb the magnetic fields and result in magnetic lines of force that are highly distorted. The possible damage location is where the magnetic lines of force are nonsymmetric or eerie. The magnetic particle inspection has the best performance when the suspected damage is perpendicular to the magnetic field; therefore, the choice of direction impacts the results.

Eddy current testing is a defect inspection technique for conductive materials. An alternating electric current in a circular coil generates a varying magnetic field, and the interaction between this varying magnetic field and a nearby conductor results in eddy current on the conductor. Flaws or defects in the conductor will change the induced eddy current, and they can be detected by placing a inspection coil which examine its current generated by the conductor. Generally, eddy current testing is portable and easy to implement, but the surface accessibility and penetration ability of magnetic field have to be considered.

Liquid penetrant testing is a simple and effective method for detecting surface damage. A liquid dye penetrant is firstly applied to the suspected surface and left for a suitable dwell time. The dye penetrant will be absorbed into the surface cracks due to the capillary action. After the dwell time has passed, the surface need to be wiped gently. Finally, a developer is sprayed onto the surface indicating possible damage of the surface. The selected dye has to be highly visible, washable, and insensitive to the tested materials. The liquid penetrant method is less time consuming and less expensive among most NDT techniques.

As presented above, there are many NDT techniques developed to detect damage, but the wave-based techniques are the most promising ones and attract much attention from researchers and engineers. Waves can propagate at a long distance so that the whole structure including the surface and body can be examined. Based on the frequency ranges, waves can be classified as ultrasonic, sonic, and subsonic waves. Ultrasonic waves, which have frequency above $20k$Hz, are used for NDT, and can be carried out in two ways: active inspection and passive inspection. For active inspection, an actuator and a receiver are mounted on the suspected surface. The

receiver receives the altered signals, which are caused by passing through damage area, and the damage location can be identified by data processing techniques. For passive inspection, two receivers are mounted on the suspected surface. When any part of the structure is damaged, the receivers receive the signals generated by the disturbance. After analyzing the two received signals, the location of damage can be identified. Ultrasonics inspection involves many disciplines such as sensing and signal processing techniques; it is an active research area nowadays.

In recent years, incorporating NDT with structural health monitoring (SHM) has been a topic of great interest. SHM firstly provides a real-time global level monitoring and then NDT will be employed to detect local damage of structures. Simply put, as shown in Figure 1-1, SHM narrows the possible damage location from global to local, and NDT is used to find the exactly position and quantify damage.

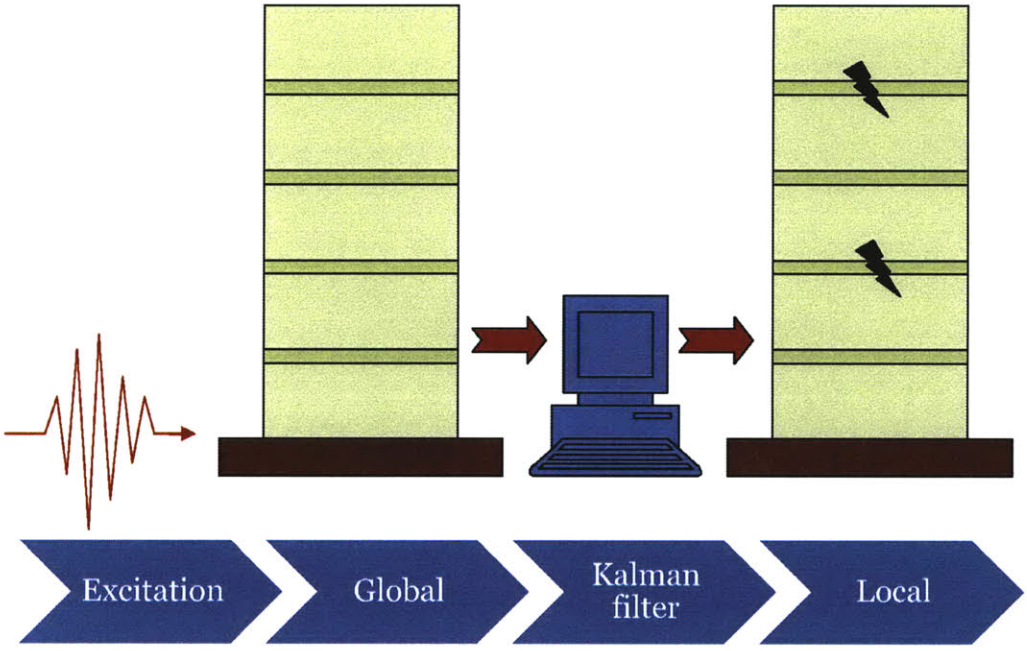

Figure 1-1: General process of implementing SHM.

1.1.3 Structural Heath Monitoring

Structural Health Monitoring (SHM) has been studied intensively in recent years due to the rapid rise of wireless and computation technologies, and it has been already applied to field works [34, 16, 31]. SHM aims to diagnose the health conditions of a structure, including damage location, damage quantification, and remaining service life. We can refer SHM to a hierarchy process as shown in Figure 1-2. SHM provides an integrity monitor on a real-time basis over the whole lifespan of structures, and a complete SHM strategy allows an optimal use of structures, reduces the maintenance costs, and avoids catastrophic failures. SHM can be classified as global monitoring and local monitoring. At the global level, monitor techniques mainly rely on the measurement of vibration data. For local monitoring, eddy current, magnetic field, and ultrasonics are the main tools [17]. Sensors technology, data analysis techniques, and health condition evaluation are needed to access a completed SHM process.

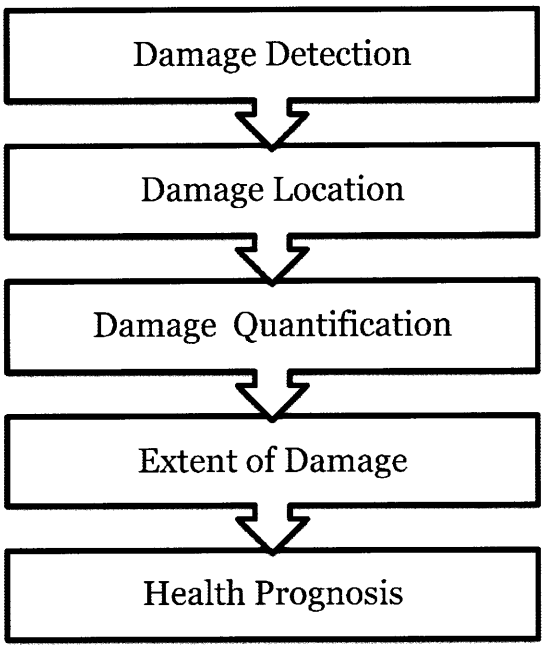

Figure 1-2: Hierarchy of damage detection.

Service life prognosis is highly related to the cost of civil structures, and the accuracy of prognoses is based on system identification techniques. Therefore, system identification becomes an important issue in SHM. Many system identification techniques in earthquake engineering were proposed to analyze and interpret the vibration data which are measured before and after a severe event such as an earthquake or a hurricane. Structural parameters such as mass, stiffness, and damping coefficient may degrade when damage occurs, and a common way to evaluate the health conditions of a structure is to compare the changes of these identified structural parameters.

The parameters to be monitored depend on different factors. If a structure is located at a highly seismic area, stiffness, deformation, or stress may need to be monitored. If a structure is built for refrigeration industry, temperature and humidity may be the parameters to be monitored. Hence, the locations and the functionalities of a structure are the key factor to decide which parameters to be monitored.

There is no such an approach that can identify all the structural systems because of the complexity of real structures. As a result, plenty of system identification techniques were proposed to deal with different structural systems. In general, we can identify the structural parameters in either frequency domain or time domain. Frequency domain approaches such as the peak-picking method and the circle-fit method mainly rely on measured data of frequency-response-function [3]. A critical issue for SHM is "monitoring" the structures in real-time; therefore, the time domain analysis techniques may be the preferred ones. Several techniques in time domain have been studied for SHM such as the Recursive Least Squares method, the Parity Equation method, the Neural Networks, and the Kalman filter. In this thesis, the Kalman filter is adopted to evaluate the health of structures.

1.2 Motivations

Civil and industrial infrastructures such as buildings, bridges, roads, railways, harbors, and airports are the essential elements composing a society, and apparently, people cannot live without them. Structures affect not only human beings but also

environment, climate, creatures and so on. In addition, structures are costly and are always related to the assets of countries. Therefore, building a safe, durable, and cost effective structure is always the goal for civil engineers.

However, structures deteriorate due to physical aging and natural hazards, and that will result in serious consequences. Human victims, ecological pollution, and economy crushing are always involved in the accidents. To prevent this sort of event, revealing the health conditions of structures becomes a critical issue. Hence, safety and economics are the main motivation for carrying out this research.

The vibration data of a structure that has undergone an extreme event such as earthquake can be used to determine whether the structure is damaged or not. Unfortunately, these data often contain noise so that the useful information is corrupted. Hence, signal processing techniques are required to deal with this problem. The Kalman filter is a promising way to filter out noise and extract the useful information because theoretically it provides the best estimation among all the linear filters. Therefore, the Kalman filter was used for identifying structural parameters throughout this thesis.

1.3 Objectives

The main objective in this thesis is to evaluate the Kalman filter's ability to estimate structural parameters, so that, as mentioned above, we can narrow the possible damage location from a whole building to a specific floor (global to local) . We will develop different structural models to represent different types of buildings, and apply the Kalman filter to each model. The measured data may be affected by external (environment) or internal (sensors) noise; therefore, the capability of the Kalman filter to predict unknown parameters is desirable. The process noise covariance and measurement noise covariance affect the estimation results as well; hence, the influences of different levels of noise covariance are also discussed.

1.4 Thesis Outline

This thesis is organized as follows:

Following this introduction, Chapter 2 of this thesis provides a brief literature review on the Structural Health Monitoring including sensors and actuators issue used for sensing the structures, the data analysis techniques used for processing the vibration data involved in damage events, and health condition evaluation used for examining the functionalities of structures.

In Chapter 3, the Kalman filter algorithm, which is used throughout the simulation part in this thesis, is derived. In general, the Kalman filter can be classified into two categories: (1) the ordinary Kalman filter, which can deal with linear system, and (2) the extended Kalman filter, which is able to tackle nonlinear system. Both of them are described in great detail. Meanwhile, an adaptive extended Kalman filter used for estimating abrupt changes of structural parameters of a dynamical system is also presented in this chapter.

In Chapter 4, the capability of the Kalman filter to estimate the structural parameters is discussed. Linear and nonlinear single-degree-of-freedom elastic structures are considered firstly, followed by two multi-degree-of-freedom elastic structures with linear and nonlinear properties. In order to simulate damage of a real civil structure, structural parameters are changed suddenly at a particular time slice. All the simulation cases are carried out with different levels of noise and noise covariance.

Finally, in Chapter 5, the main findings and contributions are summarized. The possible future research directions and extension works of this thesis are suggested at the end of this chapter.

Chapter 2

Literature Review

The way architectures and civil engineers design, build, operate, and maintain a building has been changed into a new stage. Technologies such as high performance materials, intelligent sensing systems, and adaptive control systems are merged together and lead to a so-called "Smart Structure" stage. Smart Structure is a structure that has the ability to detect the disturbance or damage by itself and adopts an adequate mechanism to recover to its original state. Structural Health Monitoring (SHM) provides a comprehensive monitor on structures, and it is the essential component of Smart Structure. In general, SHM can be divided into three parts: (1) sensors and actuators placement, (2) sensing technology, (3) data processing and health evaluation. In this chapter, the past works of all these parts are presented.

2.1 Sensors and Actuators Placement

To effectively investigate damage, a dense array of sensors and actuators is envisioned for large-scale structures. For global damage detection, the accelerograms, which can be obtained from accelerometers, in each floor are essential for vibration-based techniques. For local damage detection, the optimal placement of the sensors and actuators need to be evaluated because it impacts the performances of SHM. Benefits from the optimal placement are described as follows [36]:

- use minimal sensors and actuators to reduce the cost of devices and implemen-

tation;

- obtain accurate signal information from noisy data;
- monitor efficiently the structural behavior;
- repair or remove easily the sensors and actuators.

An intuitive optimal placement based on the knowledge of structural analysis is a solution to this problem. However, more systematic optimization methods are desired to be developed. Lim [22] adopted an effective independence algorithm to evaluate the contribution of each sensor so that the less contributed sensors can be eliminated. The Genetic Algorithms (GAs) are probabilistic search algorithms initially proposed by Holland (1975) inspired by Darwin's theory of evolution. The GAs can efficiently find the optimal solution from the discontinuous solution space, and they have been widely applied to evaluate the optimal placement of sensors for discrete structures like civil structures [1, 24]. In order to find the optimal placement and number of sensors and actuators, minimizing the system norms is also a promising approach. Different norms can be chosen as the objective function for different situations. A comprehensive study was carried out in [27].

2.2 Sensing Technology

Sensors are devices mounted in or on an object to attain desired information of the object and have the ability to transform the information into electrical signals. Sensors, in general, consist of three parts: (1) sensing elements, (2) signal processing algorithms, and (3) sensor interface [21]. When manufacturing a sensor, the sizes and costs have to be considered because usually a large amount of sensors are required for a sensing system. A sensor with small size, low cost, high quality, and reliable outputs is the one that researchers and engineers are looking for [43].

The most radical issue needed to be addressed when developing a sensing system for SHM is to accurately capture the structural responses (signals). Wired sensors

are the traditional ones which are linked together to the central computer. But for global damage detection, wired sensors are inconvenient, particularly for large-scale structures. As a result, wireless sensors are desired for global monitoring. However, wireless sensors can be unreliable. For example, external or internal noise, path losses, and hardware components reduce the accuracy of acquired signals resulting in delayed transmission of data and packet, or even transmitted data missing[37]. Applications of wireless sensors on civil structures with investigation on loss of signals has been studied in [38, 6, 29].

Indeed, much more attention has been focused on 'Smart Sensors' in recent years. Sensors with embedded systems such as microprocessors provide self-diagnosis and self-adaptation are called Smart Sensors. The first application of Smart Sensors for civil structures was carried out by Straser and Kiremidjian [44]. They developed sensors with real-time damage detection ability during extreme events and long time health monitoring. The ability to manufacture high quality microprocessors allows sensors producing accurate signals and processing data in high speed. The increasing volume of data storage provides larger processing space. The switch of waiting mode and operational mode of sensors reduces the batteries consumption. With these rising technologies, Smart Sensors have received great improvements in rapid speed and many proprietary smart sensing platforms have been created and applied to industry. Tomonori and Spencer provided [45] a summary of recent development of Smart Sensors for SHM in great detail.

2.3 Data Processing and Health Evaluation

Signals more or less contain noise in an open environment; hence, signal processing techniques become essential to mitigate noise and identify useful information from the noise-contaminated signals. The identified or filtered signals are the basis for evaluating the health conditions of a structure. Accurate signals allow the SHM system to correctly detect, measure, and evaluate the performances of a structure over its service life. The monitored structure could be a delicate aircraft, a civil infrastruc-

ture, or any mechanical system. A fully-developed SHM system enhances the safety level and reduces the maintenance cost of a structure. Damage detection is the core of SHM and it relies mainly on the signal processing techniques. In general, the processing techniques can be classified into two types: frequency domain techniques and time domain techniques. These two approaches are discussed respectively as follows.

2.3.1 Frequency Domain Approaches

Frequency domain approaches extract modal parameters such as modal frequencies, modal damping, and mode shapes from frequency response function data which are derived from vibration data [8]. The earliest method incorporates the finite element method with linear modal properties to detect possible damage [35, 25]. The peak-picking method identifies the eigenfrequencies as the peaks of a spectrum, and this method is broadly used in many area due to its simplicity [4]. The circle-fit method, which adopts the circularity property of a frequency response function, is a common yet effective technique to attain modal information [10, 15, 18]. Other methods such as the inverse frequency response function method and the Dobson's method are also extensively used for damage detection [15]. A integrated review of the damage detection and health monitoring using frequency domain analysis can be found in [8].

However, the modal parameters are easily changed due to external disturbances such as light wind and operational vibration. As a result, it is difficult to distinguish whether the structure is truly damaged or just disturbed by the environment. Moreover, these approaches cannot detect the onset of damage [30]. Hence, research has focused on time domain analysis in recent days.

2.3.2 Time Domain Approaches

Time domain approaches mainly utilize their stochastic properties to filter out noise and, further, identify the system. The Parity Equation method was developed to evaluate the residuals obtained from measured data which indicate the behavior of the monitored system. Basically, this method provides a proper check of the consistency

of measurement outputs which are acquired from the structural model and the real system. Fritzen et al. [13] proposed a robust algorithm to determine the residuals so that damage can be detected.

The Recursive Least Squares (RLS) method estimates parameters in real-time by minimizing the overall squared errors. The RLS algorithm is one of the most traditional methods to recursively update estimated parameters, and it was originally developed by Carl Friedrich Gauss. Since it was developed, the RLS has been widely used in various fields because it is simple to implement and does not need to store the whole observed data [2]. In civil engineering, especially in the area of system identification and damage detection, the RLS is used to identify structural properties and parameters for both linear and nonlinear systems. Loh et al. [26] adopted the RLS method to identify time-variant system and a system with abrupt changes of modal parameters. Lin [23] incorporated a variable forgetting factor approach with the RLS algorithm to identify nonlinear multi-degree-of-freedom structural systems with only acceleration measurements. Yang [50] proposed a RLS estimation with unknown inputs to identify structural parameters when the external excitations are not available.

The Neural Networks are another well-known time domain signal processing techniques which are capable of modeling relations of input-output functions. It was firstly developed in the fields of brain and cognitive science, showing the massively parallel distributed processing functionality of neurons. When the Neural Networks are applied in artificial intelligence, a simplified neuron model is used to perform certain tasks such function approximation and data processing. The Neural Networks can be trained based on observed data and they operate as black boxes and adaptive tools. Applications of the Neural Networks in civil engineering became popular in late 1980s due to the development of backpropagation [40]. The basic idea of backpropagation is that the synapses of a neuron model collect many weighted inputs, and the weights (parameters to be estimated) are changed in gradient descent so that the error between predicted outputs and real outputs can be reduced. In general, most Neural Networks applications in civil engineering are based on backpropagation because of

its simplicity. Flood [12, 11] applied the Neural Networks to optimize construction operation and process problems. Wong et al. [47] performed the hazard prediction of a structure due to earthquake loads. In concrete engineering, Yeh [51] optimized the workability of high performance concrete mixture. Elkordy et al. [9] proposed a diagnostic system based on the Neural Networks for detecting damage for a five story steel frame model. Based on acceleration data obtained from earthquake excitations, Qian and Mita [39] evaluated the structural parameters using the artificial Neural Network emulators.

The Kalman filter has been received extensively attention since R. E. Kalman [19] published a paper describing the recursive solutions of predicting state variables for linear systems in 1960. The advances in computing technology allow huge amounts of computation and make the Kalman filter be applied practically. The Kalman filter provides real-time estimations on state variables based on minimizing the mean squared error. The Kalman filter generates the best estimation if the optimal filter is linear among all the linear observers because it minimizes the error covariance. Since the Kalman filter only works for linear system, the extended Kalman filter was developed to deal with nonlinear system in which the system has been linearized. The Kalman filter is mainly used in the areas of aeronautics and robotics for navigation applications. In civil engineering, the Kalman filter has been mostly studied for SHM and on-line damage detection. Xia et al. [48] proposed a technique to solve the stability and divergence problems of the Kalman filter. Maruyama and Hoshiya [32] proposed a method which incorporates a weighted global iteration procedure with the extended Kalman filter to obtain stable parametric estimations and fast convergence. Yang et al. [49] proposed an adaptive extended Kalman filter algorithm to estimate damaged structural parameters with abrupt stiffness changes. Zhou et al. [52] performed an experimental study on identifying structural parameters of a damage structure. Soyoz and Feng [42] verified the capability of the extended Kalman filter on detecting instantaneous damage of a concrete bridge by using large-scale shaking table test.

2.4 Chapter Summary

In this chapter, we reviewed the essential elements and available algorithms for performing Structural Health Monitoring which provides continuous information about the health conditions of a structure. The idea of merging Smart Structure with sensing technology and signal processing techniques was carried out as well. Due to the needs of safe space and better structural performances, there is no doubt that the increase applications and research activities on Smart Structure and SHM will be continued.

Chapter 3

The Kalman Filter

Filtering is a process that eliminates noise from electrical signals and returns valuable information from which we can identify or even control a system or an object. Among many filter algorithms, the Kalman filter provides the best estimation on unknown variables if we assume the optimal filter is linear as it minimizes the error covariance throughout the process.

The development of the Kalman filter can be traced back to 1960s. In 1960, R. E. Kalman published a famous paper proposing a new approach to predict random signals of a linear system, and that approach has been called the "Kalman filter" [19]. In 1961, R. E. Kalman and R. S. Bucy published a paper in which they solved the nonlinear differential equation of the Riccati type used in continuous-time domain [20]. With the rapid rise of computation technology, the Kalman filter has been extensively studied and developed. A brief yet clear introduction of the theory of the Kalman filter with some simple examples was carried out in [41].

In this chapter, the theory of Kalman filter would be stated [2]. In general, we classify the Kalman filter into three parts: the ordinary Kalman filter, the extended Kalman filter, and the adaptive extended Kalman filter. The ordinary Kalman filter can be applied to linear system, the extended Kalman filter can tackle with nonlinear system, and the adaptive extended Kalman filter was developed for specific purpose such as estimating time-varying parameters or dealing with highly nonlinear systems.

3.1 Ordinary Kalman Filter

State space representation is used in the Kalman filter algorithm; therefore, the common usages and conventions of this representation are firstly presented. General speaking, the Kalman filter can be described in two types: discrete type and continuous type. In this section, both of them are derived.

3.1.1 State Space Estimation

Consider a linear discrete-time dynamical system which can be written as

$$x_{t+1} = A_t x_t + B_t u_t \tag{3.1}$$

where x_{t+1} and x_t are state vectors; u_t is an input vector; and A_t, B_t are transition matrices. The output measurements of this dynamical system can be represented as

$$y_t = H_t x_t \tag{3.2}$$

where H_t is a measurement transition matrix. If a dynamical system is represented as Equation 3.1 and 3.2, we say it is described in a state space representation.

One radical concept of the Kalman filter is that the state estimation is recursively corrected by the actual physical system outputs:

$$\hat{x}_{t+1} = A_t \hat{x}_t + B_t u_t + K_t(y_t - \hat{y}_t) \tag{3.3}$$

$$\hat{y}_t = H_t \hat{x}_t \tag{3.4}$$

where hat means estimation states and K_t is a feedback gain matrix. Figure 3-1 shows the block diagram of Equation 3.3 and 3.4.

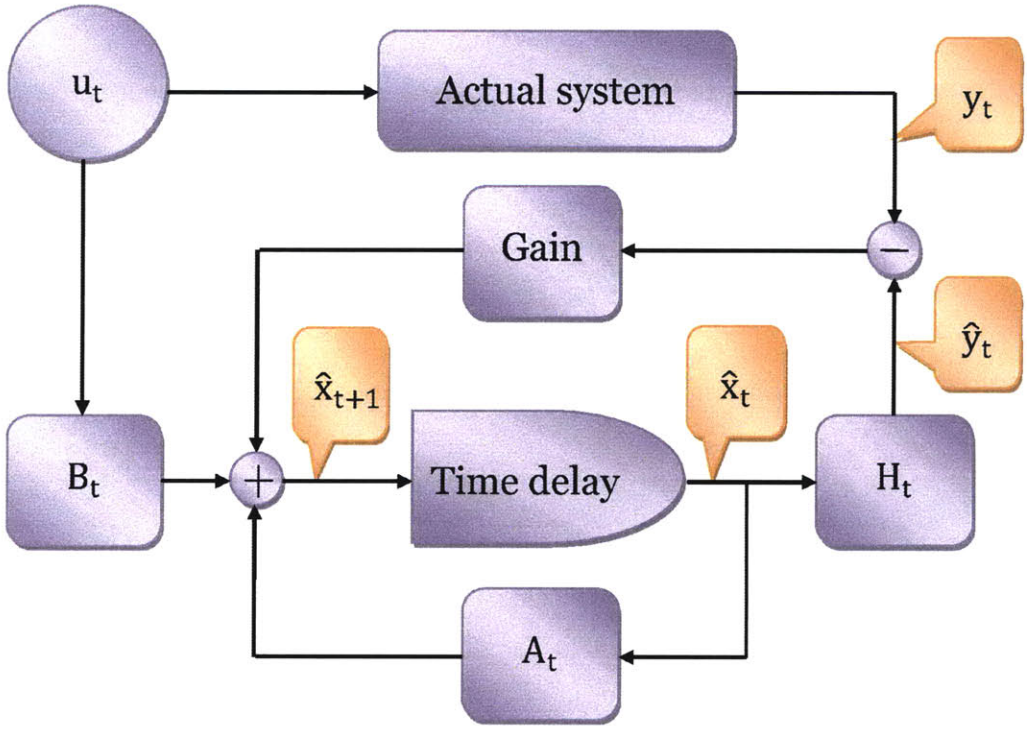

Figure 3-1: Block diagram of the Kalman filter.

Now we consider a dynamical system added by a noise term making this system a random process. Some basic concepts of random process can be found in [5, 28, 14].

$$x_{t+1} = A_t x_t + B_t u_t + G_t w_t \tag{3.5}$$

where w_t is process noise and G_t is a process noise transition matrix. When measuring the responses of a dynamical system, the signals produced by sensors would be contaminated by noise due to internal manufacturing defects or external environmental disturbances. Therefore, the contaminated output measurements can be described as

$$y_t = H_t x_t + v_t \tag{3.6}$$

where v_t is measurement noise. Note that the Kalman filter assumes every measurement from the physical sensors contains noise; therefore, if measurement noise is zero, then the Kalman filter collapses. Setting the mean of noise to be zero is a common practice as shown in Equation 3.7 and 3.8.

$$E[w_t] = 0 \tag{3.7}$$

$$E[v_t] = 0 \tag{3.8}$$

The process noise covariance and measurement noise covariance can be expressed as

$$Cov[w] = E[w_t w_s^T] \tag{3.9}$$

$$Cov[v] = E[v_t v_s^T] \tag{3.10}$$

where t and s are different time instances. If the noise signals of any two time instances are uncorrelated, then we call this kind of noise as "white noise." In general, covariance of process noise and measurement noise is zero:

$$Cov[w, v] = E[w_t v_s^T] = 0 \tag{3.11}$$

Since the state variables and output measurements contain process noise and measurement noise, respectively, the system can be described as a random process. The deterministic term $B_t u_t$ makes no influence on the state variables in the stochastic estimation process; therefore, the $B_t u_t$ term could be eliminated during the whole process without losing generality. Suppose a dynamical system is given by Equation 3.12 and 3.13, and it has the stochastic properties as shown from Equation 3.14 through 3.17.

$$x_{t+1} = A_t x_t + G_t w_t \tag{3.12}$$

$$y_t = H_t x_t + v_t \tag{3.13}$$

$$E[w_t] = E[v_t] = 0 \tag{3.14}$$

$$E[w_t w_s^T] = \begin{cases} 0, & \text{if } t \neq s \\ Q_t, & \text{if } t = s \end{cases} \tag{3.15}$$

$$E[v_t v_s^T] = \begin{cases} 0, & \text{if } t \neq s \\ R_t, & \text{if } t = s \end{cases} \tag{3.16}$$

$$E[w_t v_s^T] = 0 \ \ \forall t, s \tag{3.17}$$

where Q_t is process noise covariance and R_t is measurement noise covariance. As

mentioned before, the basic assumption of the Kalman filter is that all sensors contain noise; therefore, matrix Q_t is positive semi-definite and matrix R_t is positive definite. The Kalman filter produces the optimal estimation by minimizing the mean squared error based on the measurements:

$$J_t = E[(\hat{x}_t - x_t)^T(\hat{x}_t - x_t)] \tag{3.18}$$

3.1.2 Discrete Kalman Filter

The discrete Kalman filter provides recursive solutions by minimizing Equation 3.18. Suppose $\hat{x}_{t|t-1}$ represents a priori state estimation at time t based on $\hat{x}_{t-1}$ which is the state estimation at time $t-1$. Then, $\hat{x}_{t|t-1}$ can be expressed as

$$\hat{x}_{t|t-1} = E[x_t|x_{t-1}] \tag{3.19}$$

By substituting Equation 3.12 into 3.19, we obtain

$$\begin{aligned} \hat{x}_{t|t-1} &= E[A_{t-1}x_{t-1} + G_{t-1}w_{t-1}] \\ &= A_{t-1}\hat{x}_{t-1} + G_{t-1}E[w_{t-1}] \\ &= A_{t-1}\hat{x}_{t-1} \end{aligned} \tag{3.20}$$

Similarly, the output measurements can be derived as

$$\begin{aligned} \hat{y}_t &= E[H_t\hat{x}_{t|t-1} + v_t] \\ &= H_t\hat{x}_{t|t-1} + E[v_t] \\ &= H_t\hat{x}_{t|t-1} \end{aligned} \tag{3.21}$$

The state estimation can be updated in real-time by the predicted error which is the difference between real and estimated measurements.

$$\begin{aligned} \hat{x}_t &= \hat{x}_{t|t-1} + K_t(y_t - \hat{y}_t) \\ &= \hat{x}_{t|t-1} + K_t(y_t - H_t\hat{x}_{t|t-1}) \end{aligned} \tag{3.22}$$

where K_t is called the Kalman gain. The mean squared error in Equation 3.18 can be minimized by optimizing the Kalman gain. Figure 3-2 shows the outline of the Kalman filter.

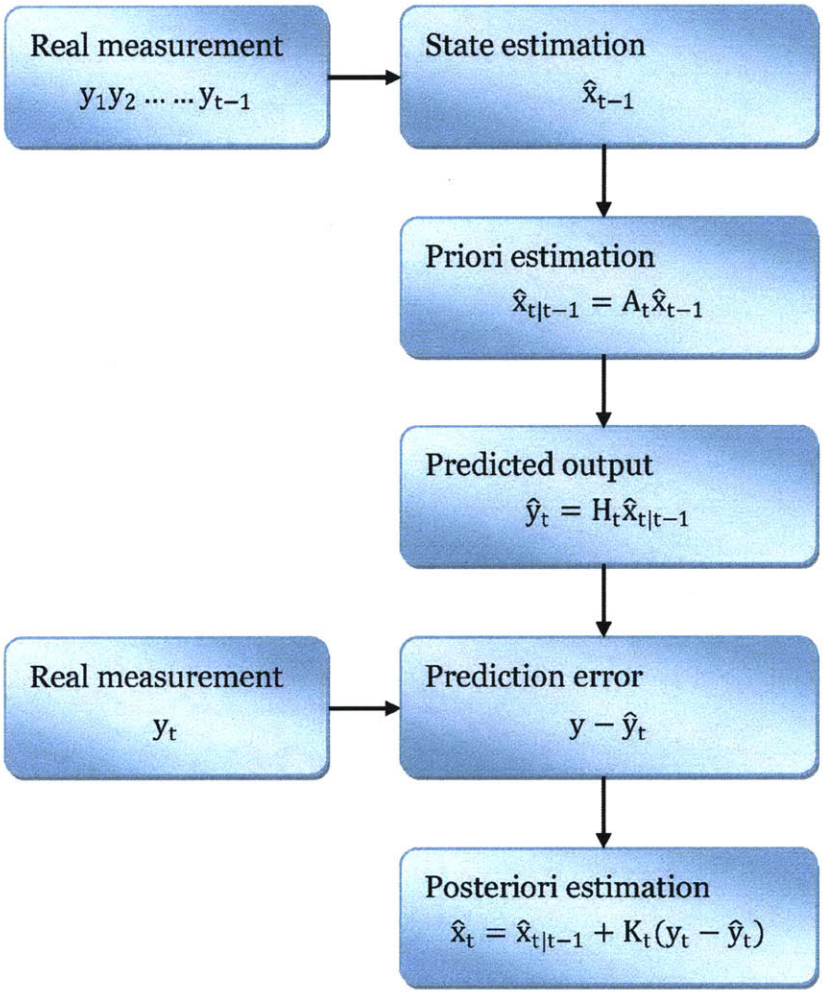

Figure 3-2: Process flow of the Kalman filter.

Define ϵ_t as a priori estimation error and γ_t as a posteriori estimation error, namely:

$$\epsilon_t \equiv \hat{x}_{t|t-1} - x_t \tag{3.23}$$

$$\begin{aligned} \gamma_t \equiv \hat{x}_t - x_t &= \hat{x}_{t|t-1} + K_t(y_t - \hat{y}_t) - x_t \\ &= (\hat{x}_{t|t-1} - x_t) - K_t H_t(\hat{x}_{t|t-1} - x_t) + K_t v_t \\ &= (I - K_t H_t)\epsilon_t + K_t v_t \end{aligned} \tag{3.24}$$

As stated before, the optimal estimation is based on minimizing the mean squared error with respect to the Kalman gain K_t:

$$J_t = E[\gamma_t^T \gamma_t] \tag{3.25}$$

$$\frac{dJ_t}{dK} = 0 \tag{3.26}$$

To access this, the following calculation is needed. Note that all terms in Equation 3.27 are symmetric because they are scalar functions.

$$\begin{aligned} \gamma_t^T \gamma_t &= [(I - K_t H_t)\epsilon_t + K_t v_t]^T [(I - K_t H_t)\epsilon_t + K_t v_t] \\ &= \epsilon_t^T \epsilon_t + \epsilon_t^T H_t^T K_t^T K_t H_t \epsilon_t - 2\epsilon_t^T K_t H_t \epsilon_t \\ &\quad + 2\epsilon_t^T K_t v_t - 2v_t^T K_t^T K_t H_t \epsilon_t + v_t^T K_t^T K_t v_t \end{aligned} \tag{3.27}$$

$$\frac{dE[\gamma_t^T \gamma_t]}{dK} = 0 \tag{3.28}$$

$$2E[K_t H_t \epsilon_t \epsilon_t^T H_t^T - K_t H_t \epsilon_t v_t^T - K_t v_t \epsilon_t^T H_t + K_t v_t v_t^T + \epsilon_t v_t^T - \epsilon_t \epsilon_t^T H_t^T] = 0 \quad (3.29)$$

Note that random variables in Equation 3.29 are only ϵ_t and v_t; therefore, K_t and H_t can be factored out when taking expected values.

$$\begin{aligned} K_t H_t E[\epsilon_t \epsilon_t^T] H_t^T &- K_t H_t E[\epsilon_t v_t^T] - K_t E[v_t \epsilon_t^T] H_t^T \\ &+ K_t E[v_t v_t^T] + E[\epsilon_t v_t^T] - E[\epsilon_t \epsilon_t^T] H_t^T = 0 \end{aligned} \quad (3.30)$$

Using Equation 3.20 and 3.23, we obtain $E[\epsilon_t v_t^T] = E[v_t \epsilon_t^T] = 0$. In addition, define $P_{t|t-1}$ as a priori state estimation error covariance:

$$P_{t|t-1} = E[\epsilon_t \epsilon_t^T] \quad (3.31)$$

Note that $E[\epsilon_t \epsilon_t^T] \neq E[\epsilon_t^T \epsilon_t]$ because the former one is a matrix but the later one is a scalar. Then Equation 3.30 can be rewritten as

$$K_t H_t P_{t|t-1} H_t^T + K_t R_t - P_{t|t-1} H_t^T = 0 \quad (3.32)$$

$$K_t = P_{t|t-1} H_t^T [H_t P_{t|t-1} H_t^T + R_t]^{-1} \quad (3.33)$$

Now, define P_t as a posteriori state estimation error covariance:

$$P_t = E[\gamma_t \gamma_t^T] \quad (3.34)$$

From Equation 3.24, P_t can be computed as

$$
\begin{aligned}
P_t &= E[((I - K_t H_t)\epsilon_t + K_t v_t)((I - K_t H_t)\epsilon_t + K_t v_t)^T] \\
&= E[(I - K_t H_t)\epsilon_t \epsilon_t^T (I - K_t H_t)^T + (I - K_t H_t)\epsilon_t v_t^T K_t^T \\
&\quad + K_t v_t \epsilon_t^T (I - K_t H_t)^T + K_t v_t v_t^T K_t^T] \\
&= (I - K_t H_t) E[\epsilon_t \epsilon_t^T](I - K_t H_t)^T + (I - K_t H_t) E[\epsilon_t v_t^T] K_t^T \\
&\quad + K_t E[v_t \epsilon_t^T](I - K_t H_t)^T + K_t E[v_t v_t^T] K_t^T
\end{aligned} \tag{3.35}
$$

We know $E[\epsilon_t v_t^T] = E[v_t \epsilon_t^T] = 0$; therefore, Equation 3.35 can be rewritten as

$$
\begin{aligned}
P_t &= (I - K_t H_t) E[\epsilon_t \epsilon_t^T](I - K_t H_t)^T + K_t E[v_t v_t^T] K_t^T \\
&= (I - K_t H_t) P_{t|t-1} (I - K_t H_t)^T + K_t Q_t K_t^T
\end{aligned} \tag{3.36}
$$

Substituting Equation 3.33 into Equation 3.36 yields

$$
P_t = (I - K_t H_t) P_{t|t-1} \tag{3.37}
$$

In order to produce a recursive form of state estimation error covariance, we aim to compute the values of $P_{t+1|t}$.

$$
\begin{aligned}
P_{t+1|t} &= E[\epsilon_{t+1} \epsilon_{t+1}^T] \\
&= E[(\hat{x}_{t+1|t} - x_{t+1})(\hat{x}_{t+1|t} - x_{t+1})^T] \\
&= E[(A_t \hat{x}_t - A_t x_t - G_t w_t)(A_t \hat{x}_t - A_t x_t - G_t w_t)^T] \\
&= E[(A_t \gamma_t - G_t w_t)(A_t \gamma_t - G_t w_t)^T] \\
&= A_t E[\gamma_t \gamma_t^T] A_t^T - G_t E[w_t w_t^T] G_t^T
\end{aligned} \tag{3.38}
$$

Note that $E[w_t \gamma_t^T] = E[\gamma_t w_t^T] = 0$ (can be proved by Equation 3.12). Substituting P_t and Q_t into Equation 3.38, we obtain $P_{t+1|t}$ based on P_t.

$$P_{t+1|t} = A_t P_t A_t^T - G_t Q_t G_t^T \tag{3.39}$$

Hence, a recursive formula of error covariance $P_{t|t-1} \rightarrow P_t \rightarrow P_{t+1|t} \rightarrow P_{t+1}$ is obtained. A flow chart of the Discrete Kalman filter is shown in Figure 3-3.

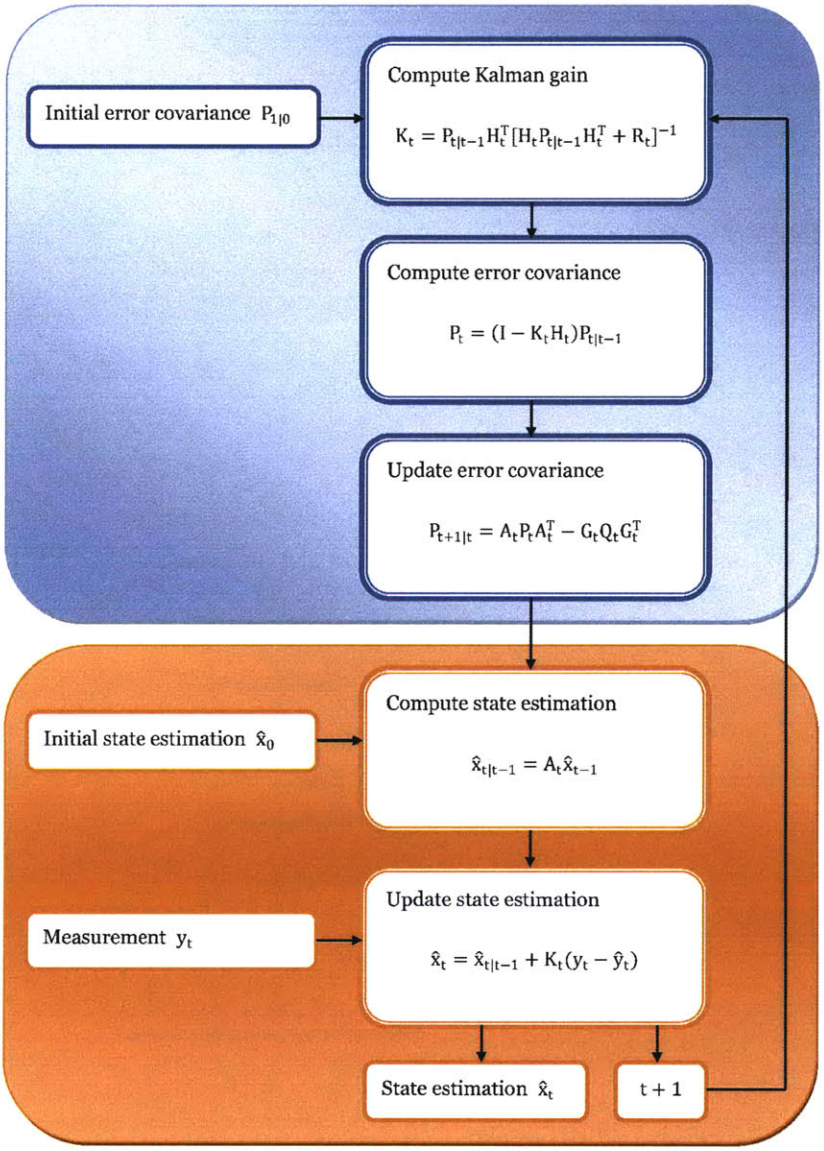

Figure 3-3: Flow chart of the discrete Kalman filter.

3.1.3 Continuous Kalman Filter

The continuous Kalman filter, also known as the Kalman-Bucy filter, is used in linear, continuous-time dynamical system. The state space representation can be described as

$$\dot{x} = Fx + Gw(t) \tag{3.40}$$

$$y = Hx + v(t) \tag{3.41}$$

where F and H are state and measurement transition matrices; $w(t)$ and $v(t)$ are process and measurement noise, which have the following properties:

$$E[w(t)w^T(s)] = Q\delta(t-s) \tag{3.42}$$

$$E[v(t)v^T(s)] = R\delta(t-s) \tag{3.43}$$

$$E[v(t)w^T(s)] = 0 \tag{3.44}$$

where $\delta(t-s)$ is Dirac delta function. Note that Q_t and R_t in the discrete Kalman filter represent noise for a specific time slice, but in the continuous-time domain we just need to use Q and R to represent noise. Q and R have the relations with Q_t and R_t as [5]

$$Q = \frac{Q_t}{\Delta t} \tag{3.45}$$

$$R = R_t \Delta t \tag{3.46}$$

where Δt is a time interval. Substituting Equation 3.45 and 3.46 into 3.33, we obtain

$$\begin{aligned} K_t &= \Delta t P_{t|t-1} H_t^T (\Delta t H_t P_{t|t-1} H_t^T + R)^{-1} \\ &= \Delta t P_{t|t-1} H_t^T R^{-1} + O(2) \end{aligned} \tag{3.47}$$

Note that $K = \frac{K_t}{\Delta t}$. Neglecting the higher order terms, K can be rewritten as

$$K = P_{t|t-1} H_t^T R^{-1} \tag{3.48}$$

In order to compute the error covariance, substituting Equation 3.45, 3.46, and 3.37 into 3.39 leads to

$$P_{t+1|t} = A_t (I - \Delta t K H_t) P_{t|t-1} A_t^T + G_t \Delta t Q G_t^T \tag{3.49}$$

Note that A_t is obtained by eliminating higher order terms as

$$\frac{x_{t+1} - x_t}{\Delta t} = F x_t + O(2) \tag{3.50}$$

$$x_{t+1} = (I + F\Delta t) x_t + O(2) \tag{3.51}$$

$$A_t = I + F\Delta t \tag{3.52}$$

The error covariance in continuous-time domain can be described by using Equation 3.49 and 3.48:

$$P_{t+1|t} = P_{t|t-1} + \Delta t F P_{t|t-1} + \Delta t P_{t|t-1} F^T - \Delta t K H_t P_{t|t-1} + G_t \Delta t Q G_t^T \tag{3.53}$$

$$\frac{P_{t+1|t} - P_{t|t-1}}{\Delta t} = F P_{t|t-1} + P_{t|t-1} F^T - P_{t|t-1} H_t^T R^{-1} H_t P_{t|t-1} + G_t Q G_t^T \tag{3.54}$$

Note that for small time intervals, $\frac{P_{t+1|t} - P_{t|t-1}}{\Delta t}$ is the derivative of $P_{t|t-1}$. Therefore, the error covariance in continuous-time domain can be derived as shown in Equation 3.55, and it is also called the Matrix Riccati Equation.

$$\dot{P} = FP + PF^T - PH^T R^{-1} HP + GtQGt^T \tag{3.55}$$

The Matrix Riccati Equation can be solved by using special techniques such as Matrix Fraction Decomposition. Compared with the discrete Kalman filter, the continuous Kalman filter needs higher observability to predict state variables. Hence, if the error covariance blows up when using the continuous Kalman filter, checking the observability is needed. Usually, poor observability can be solved by adding additional sensors onto the dynamical system. A flow chart of the continuous Kalman filter is shown in Figure 3-4.

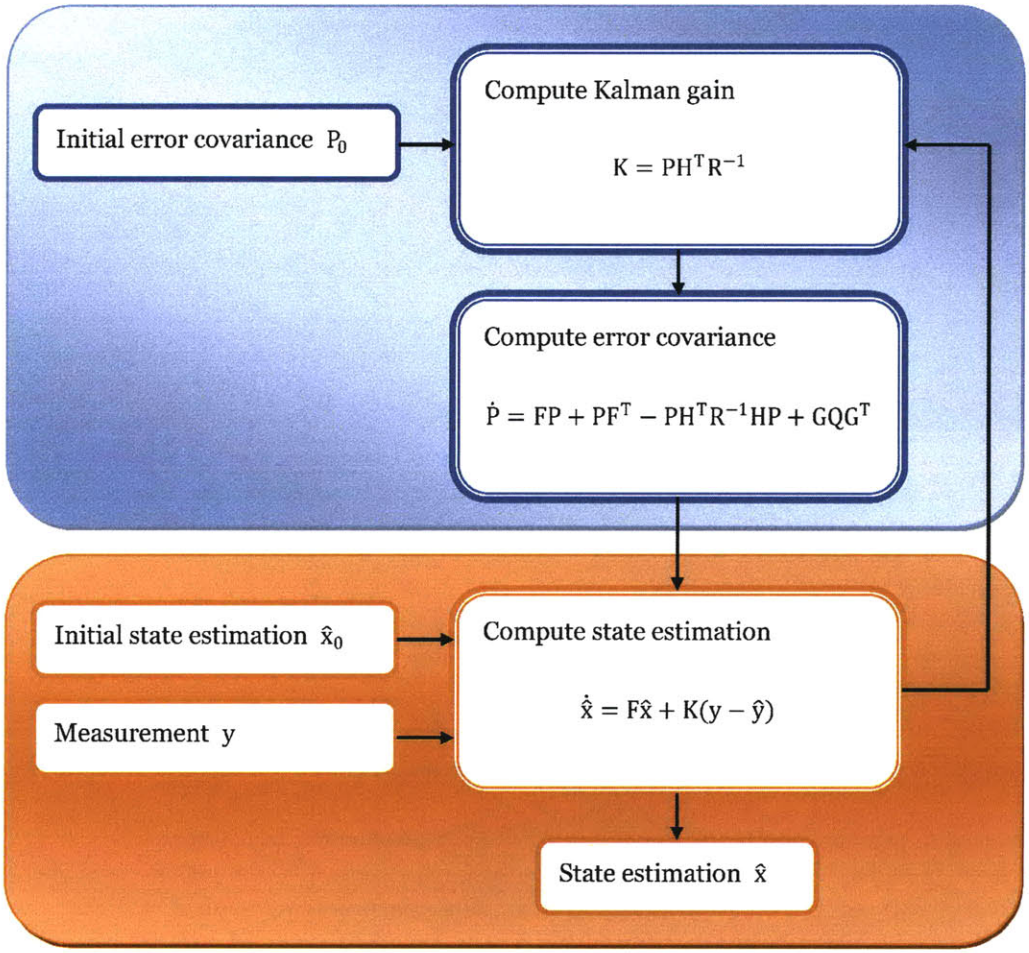

Figure 3-4: Flow chart of the continuous Kalman filter.

3.2 Extended Kalman Filter

Mathematically, engineers like to describe a physical system using a linear model. However, if a real system is complicated so that it is difficult to describe the system by just using a simple linear model, a nonlinear model may be needed [2]. The extension of the ordinary Kalman filter, called the extended Kalman filter, is developed to deal with nonlinear system. In general, the extended Kalman filter has two types: the continuous extended Kalman filter and the continuous-discrete extended Kalman filter. Both of them will be derived as follows.

3.2.1 Continuous Extended Kalman Filter

In continuous-time form, a nonlinear and differentiable dynamical system is given by

$$\dot{x} = f(x, u, t) + w(t) \tag{3.56}$$

$$y = h(x, u, t) + v(t) \tag{3.57}$$

where $f(x, u, t)$ and $h(x, u, t)$ are nonlinear vectors with state vector x and input vector u; $w(t)$ and $v(t)$ are process noise and measurement noise with the same stochastic properties as stated in the continuous Kalman filter. Because the input term u is deterministic and it won't affect the state estimation x under stochastic process, we can ignore it without loss of generality. An important step of the extended Kalman filter is to linearize the nonlinear term, and the procedures are described as below.

Consider x as an actual trajectory in a nonlinear dynamical system; $\tilde{x}$ is a nominal trajectory with no process noise in the same system. They can be written as

$$\dot{x} = f(x,t) + w(t) \tag{3.58}$$

$$\dot{\tilde{x}} = f(\tilde{x},t) \tag{3.59}$$

As shown in Figure 3-5, δx is the discrepancy between the actual trajectory and the nominal trajectory, and we can describe the relation in a mathematical form:

$$x = \tilde{x} + \delta x \tag{3.60}$$

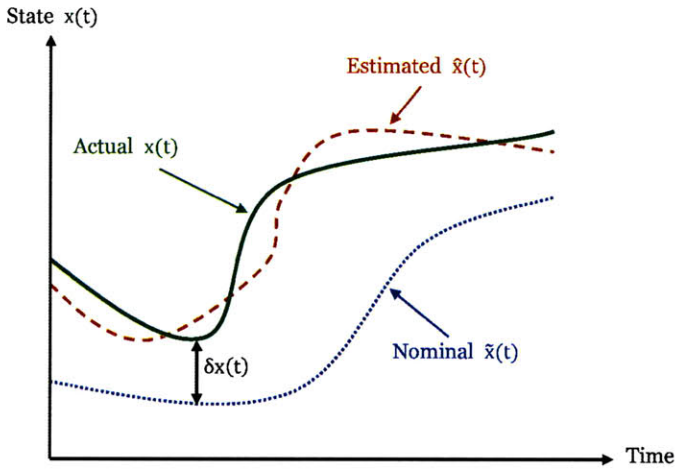

Figure 3-5: Actual and nominal trajectory of state estimation in a dynamical system.

Substituting Equation 3.60 into $f(x,t)$ and adopting Taylor expansion, $f(x,t)$ can be expressed as

$$\begin{aligned} f(x,t) &= f(\tilde{x} + \delta x, t) \\ &= f(\tilde{x},t) + \frac{\partial f}{\partial x}\Big|_{x=\tilde{x}} \delta x + O(2) \end{aligned} \tag{3.61}$$

Neglecting the higher order terms of Equation 3.61 and substituting into Equation 3.58 leads to

$$\dot{x}(t) = f(\tilde{x}, t) + \left.\frac{\partial f}{\partial x}\right|_{x=\tilde{x}} \delta x + w(t) \tag{3.62}$$

We know the $\dot{x} = \dot{\tilde{x}} + \delta\dot{x}$ and $f(\tilde{x}, t) = \dot{\tilde{x}}$; therefore, Equation 3.62 can be rewritten as

$$\dot{\tilde{x}} + \delta\dot{x} = \dot{\tilde{x}} + \left.\frac{\partial f}{\partial x}\right|_{x=\tilde{x}} \delta x + w(t) \tag{3.63}$$

Canceling out $\dot{\tilde{x}}$ on both sides and replacing δx by x and $\left.\frac{\partial f}{\partial x}\right|_{x=\tilde{x}}$ by $F(t)$, we obtain a linearized form:

$$\dot{x} = F(t)x + w(t) \tag{3.64}$$

As for linearizing the measurement outputs, similar steps are utilized:

$$y = h(x, t) + v(t) \tag{3.65}$$

$$\tilde{y} = h(\tilde{x}, t) \tag{3.66}$$

$$y = \tilde{y} + \delta y \tag{3.67}$$

Applying the Taylor expansion to $h(x, t)$ and ignoring the higher order terms, we

obtain

$$\begin{aligned} h(x,t) &= h(\tilde{x}+\delta x,t) \\ &= h(\tilde{x},t)+\left.\frac{\partial h}{\partial x}\right|_{x=\tilde{x}}\delta x \end{aligned} \tag{3.68}$$

Substituting Equation 3.67 and 3.68 into 3.65 leads to

$$\tilde{y}+\delta y=\tilde{y}+\left.\frac{\partial h}{\partial x}\right|_{x=\tilde{x}}\delta x+v(t) \tag{3.69}$$

Canceling out $\tilde{y}$ on both sides and replacing δy by y and $\left.\frac{\partial h}{\partial x}\right|_{x=\tilde{x}}$ by $H(t)$, a linearized form of the measurement outputs is derived

$$y=H(t)x+v(t) \tag{3.70}$$

Apparently the linearized form has the same state space representation as that of the ordinary Kalman filter, but note that $F(t)=\left.\frac{\partial f}{\partial x}\right|_{x=\tilde{x}}$ and $H(t)=\left.\frac{\partial h}{\partial x}\right|_{x=\tilde{x}}$. $F(t)$ and $H(t)$ can be described as

$$F(t)=\left.\frac{\partial f}{\partial x}\right|_{x=\tilde{x}}=\begin{bmatrix} \frac{\partial f_1}{\partial x_1} & \frac{\partial f_1}{\partial x_2} & \cdots & \frac{\partial f_1}{\partial x_n} \\ \frac{\partial f_2}{\partial x_1} & \frac{\partial f_2}{\partial x_2} & & \vdots \\ \vdots & & \ddots & \vdots \\ \frac{\partial f_n}{\partial x_1} & \cdots & \cdots & \frac{\partial f_n}{\partial x_n} \end{bmatrix} \tag{3.71}$$

$$H(t)=\left.\frac{\partial h}{\partial x}\right|_{x=\tilde{x}}=\begin{bmatrix} \frac{\partial h_1}{\partial x_1} & \frac{\partial h_1}{\partial x_2} & \cdots & \frac{\partial h_1}{\partial x_n} \\ \frac{\partial h_2}{\partial x_1} & \frac{\partial h_2}{\partial x_2} & & \vdots \\ \vdots & & \ddots & \vdots \\ \frac{\partial h_m}{\partial x_1} & \cdots & \cdots & \frac{\partial h_m}{\partial x_n} \end{bmatrix} \tag{3.72}$$

The extended Kalman filter is derived by linearizing the nonlinear dynamical equations at current estimation $\hat{x}_t$ which can be written as

$$F(t) = \left.\frac{\partial f}{\partial x}\right|_{x=\hat{x}} = F(\hat{x}, t) \tag{3.73}$$

$$H(t) = \left.\frac{\partial h}{\partial x}\right|_{x=\hat{x}} = H(\hat{x}, t) \tag{3.74}$$

Because the measurement outputs will correct the state estimation in real-time, the estimated trajectory is more accurate than the nominal trajectory as shown in Figure 3-5. The extended Kalman filter needs to update both state estimation and error covariance; therefore, all the processes are in real-time. A flow chart of the extended Kalman filter process is shown in Figure 3-6.

3.2.2 Continuous-Discrete Extended Kalman Filter

Due to the high level of observability required and the complexity of solving the Riccati Equation, the continuous extended Kalman filter can be simplified as a continuous-discrete extended Kalman filter. This filter is basically similar to the ordinary Kalman filter, but the linearizing procedures are added to it. A flow chart of the continuous-discrete Extended Kalman filter algorithm is shown in Figure 3-7.

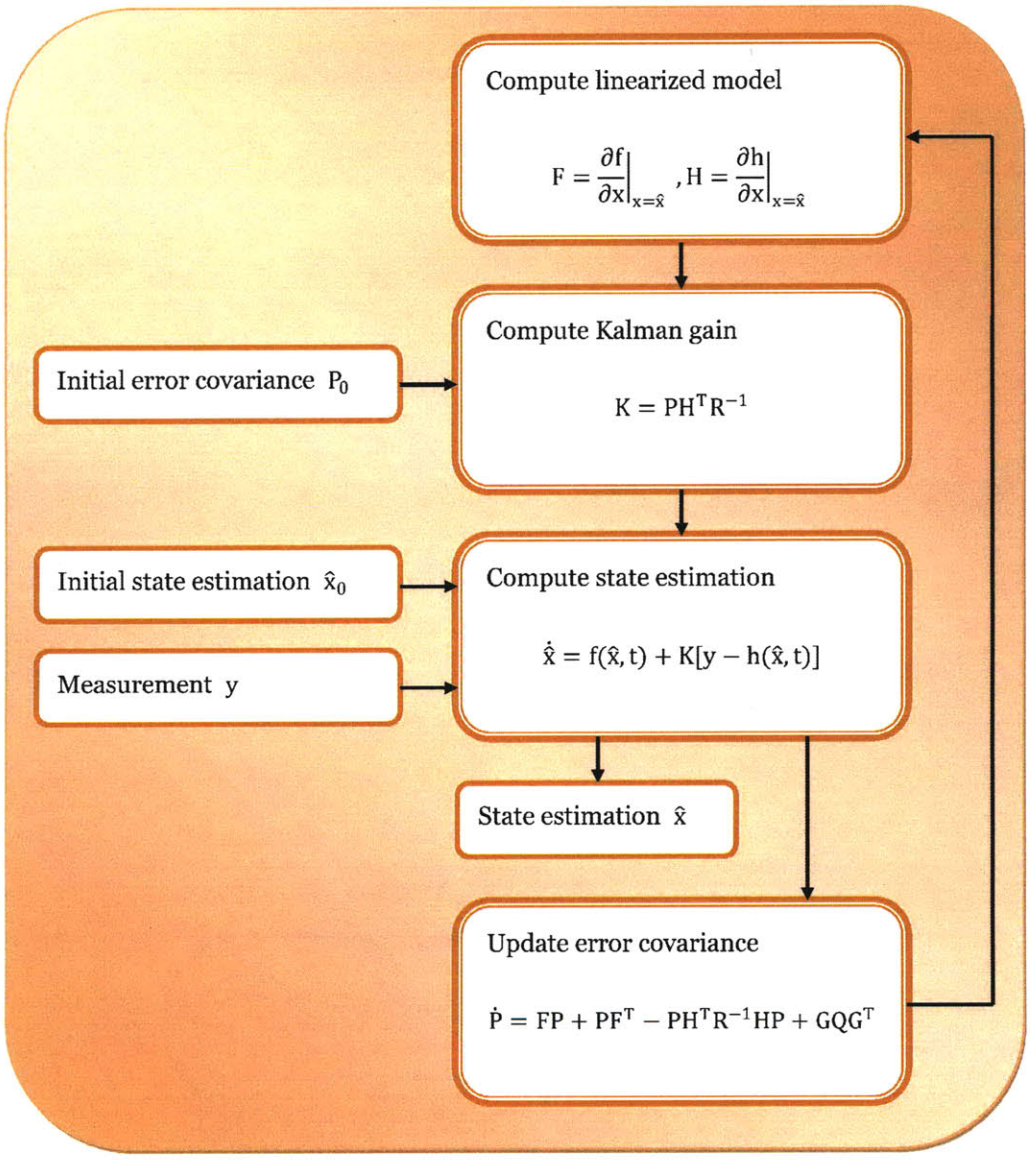

Figure 3-6: Flow chat of the extended Kalman filter.

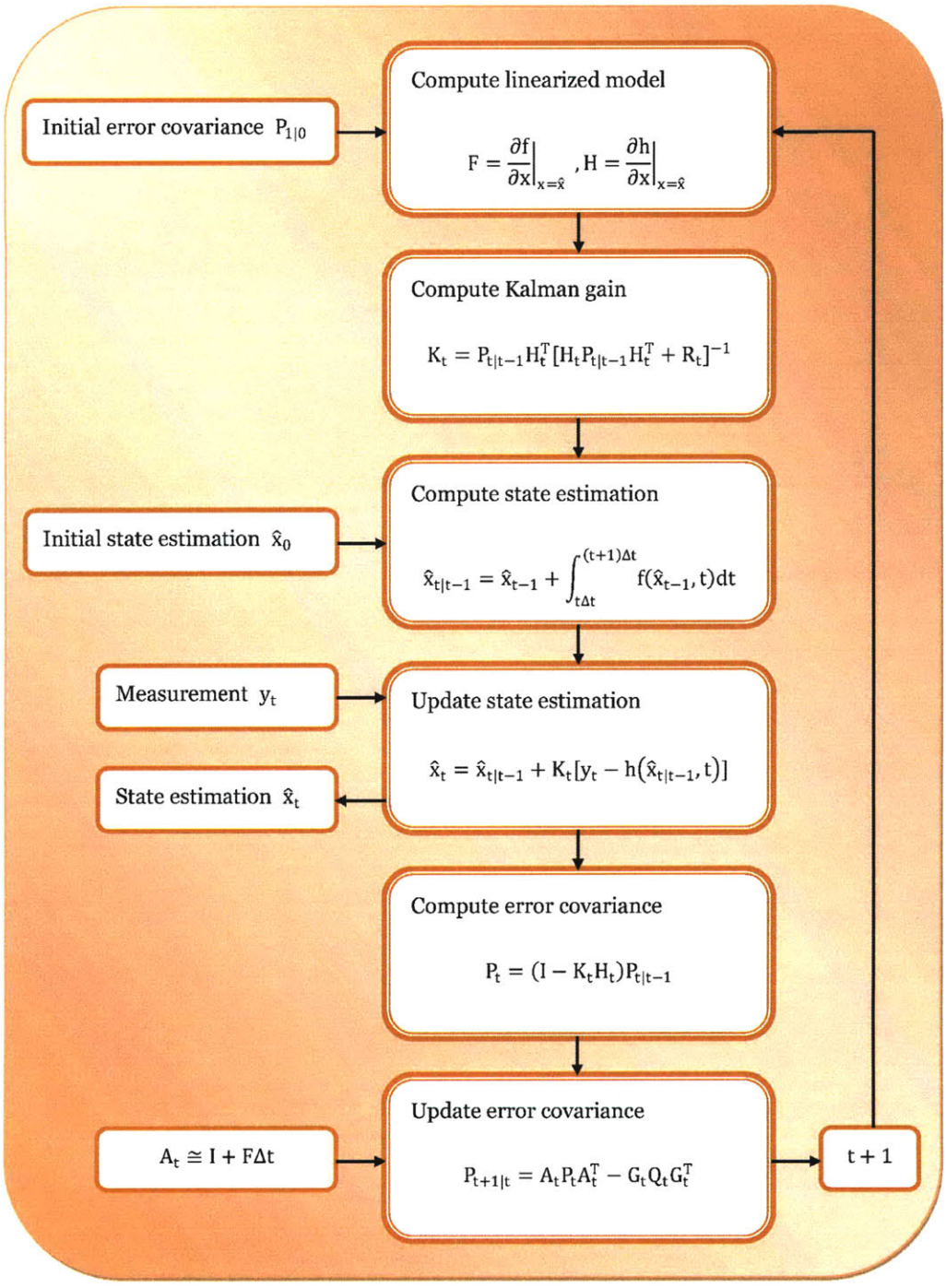

Figure 3-7: Flow chat of the continuous-discrete extended Kalman filter.

3.3 Adaptive Extended Kalman Filter

To identify time-varying structural parameters, applications of the forgetting factor are widely used throughout different estimation methods. The constant forgetting factor approach needs a trade-off between noise and accuracy, and sometimes it is inconvenient for implementation. Therefore, a variable forgetting factor approach was developed to perform a better estimation. This approach indicates the variance of parameters, but it fails to point out the exact varying parameter. To overcome this drawback, Yang et al. [49] proposed a new technique to track the time-varying parameters.

The idea is minimizing the estimation error by implementing an adaptive factor ϕ so that the filter can accurately track the parameters. The adaptive factor can be determined using the measurement outputs y. Suppose a residual error $\check{e}$ and a predicted output error e are given by

$$\check{e}_{t+1} = y_{t+1} - h(\hat{x}_{t+1}, t) \tag{3.75}$$

$$e_{t+1} = y_{t+1} - h(\hat{x}_{t+1|t}, t) \tag{3.76}$$

where the relation between $h(\hat{x}_{t+1}, t)$ and $h(\hat{x}_{t+1|t}, t)$ can be expressed as

$$h(\hat{x}_{t+1}, t) = h(\hat{x}_{t+1|t}, t) + H_t[\hat{x}_{t+1} - \hat{x}_{t+1|t}] \tag{3.77}$$

where H_{t+1} is $\frac{\partial h}{\partial x}\Big|_{x_{t+1}=\hat{x}_{t+1}}$. Substituting Equation 3.22, 3.76, and 3.77 into 3.75; and taking the expected values, we obtain

$$E[\check{e}_{t+1}\check{e}_{t+1}^T] = (I - H_{t+1}K_{t+1})E[e_{t+1}e_{t+1}^T](I - H_{t+1}K_{t+1})^T \tag{3.78}$$

Define S as the predicted error covariance which means $S_{t+1} = E[e_{t+1}e_{t+1}^T]$. Also, the residual error covariance can be described as R_{t+1} ($E[\breve{e}_{t+1}\breve{e}_{t+1}^T] = E[v_{t+1}v_{t+1}^T] = R_{t+1}$). Substituting the Kalman gain of Equation 3.33 into 3.78, the predicted error covariance can be written as

$$S_{t+1} = (H_{t+1}P_{t+1|t}H_{t+1}^T + R_{t+1})R_{t+1}^{-1}(H_{t+1}P_{t+1|t}H_{t+1}^T + R_{t+1})^T \tag{3.79}$$

Since the error covariance P is composed of the estimation error, Yang et al. proposed an adaptive error covariance to perform better tracking ability. The adaptive error covariance can be described in terms of the adaptive factor as

$$P_{t+1|t} = \Phi_{t+1}[A_tP_{t|t}A_t^T]\Phi_{t+1}^T + G_tQ_tG_t^T \tag{3.80}$$

where Φ is the adaptive factor matrix. The error covariance involves Φ; therefore, the predicted error covariance also involves Φ. The ideal adaptive factor matrix is the one that can provide accurate estimations; therefore, it can be determined by minimizing an objective function $J[\hat{\theta}_t(\Phi_t)]$ which is a function of estimated error:

$$J[\hat{\theta}_t(\Phi_{t+1})] = \sum_{i=1}^{n}\left|\frac{\hat{\theta}_i(t) - \hat{\theta}_i(t-1)}{\hat{\theta}_i(t-1)}\right| \tag{3.81}$$

where $\hat{\theta}_i$ is the parameters to be estimated. Minimizing the objective function is the key in this adaptive filter, but the relation between the predicted error covariance and the adaptive factor matrix as described in Equation 3.79 has to be satisfied. In other words, Equation 3.79 provides a condition to determine the adaptive factor matrix. The condition sometimes is too restrictive to determine the adaptive factor matrix; hence, a less restrictive condition is applied:

$$\left\| S_{t+1} - (H_{t+1}P_{t+1|t}H_{t+1}^T + R_{t+1})R_{t+1}^{-}1(H_{t+1}P_{t+1|t}H_{t+1}^T + R_{t+1})^T \right\| \leq \delta \qquad (3.82)$$

where $\|\bullet\|$ is a Frobenius norm and δ is the allowed error magnitude. To access this constrained optimization problem, an initial estimate of Φ_{t+1} is needed. Yang et al. suggested that Φ_{t+1} can be a diagonal matrix with unity for known state variables. For the other diagonal elements (unknown state variables), the initial estimation can be obtained from

$$\Phi_{t+1} = \bar{\phi}_{t+1}^{\frac{1}{2}} I \qquad (3.83)$$

where $\bar{\phi}_{t+1}^{\frac{1}{2}}$ is a variable forgetting factor and it can be computed from

$$\bar{\phi}_{t+1} = \frac{-T_b + \sqrt{T_b^2 - 4T_aT_c}}{2T_a}, \ \bar{\phi}_{t+1} \geq 1 \qquad (3.84)$$

where $T_a = tr[T_1R_{t+1}^{-1}T_1^T]$, $T_b = tr[T_1R_{t+1}^{-1}T_2^T + T_2R_{t+1}^{-1}T_1^T]$, and $T_c = tr[T_2R_{t+1}^{-1}T_2^T] - tr[S_{t+1}]$, with $T_1 = H_{t+1}A_tP_{t|t}A_t^TH_{t+1}$ and $T_2 = H_{t+1}Q_{t+1}H_{t+1}^T + R_{t+1}$

For estimating the initial adaptive factor matrix and implementing the constrained condition, the predicted output error covariance S_{t+1} should be evaluated. Similarly, Yang et al. provided a recursive evaluation for S_{t+1} as

$$S_{t+1} = E_{t+1}/F_{t+1} \qquad (3.85)$$

where $E_{t+1} = e_{t+1}e_{t+1}^T + \frac{zE_t}{\bar{\phi}_t}$ and $F_{t+1} = 1 + \frac{zF_t}{\bar{\phi}_t}$. $\bar{\phi}_t$ can be computed from Equation 3.84. The suggested initial values for E_0 and F_0 are both zero, and the constant z is suggested to be within the range of $0 < z \leq 1$.

3.4 Chapter Summary

In this chapter, we put to work the theory of the Kalman filter. The flow charts presented in each section provide a step by step implementation of different types of the Kalman filter, which can be adopted for different applications. When dealing with linear model, the ordinary Kalman filter is robust enough to perform accurate estimation. But for nonlinear system, the extended Kalman filter is not highly reliable. For example, the uncertainty of measurement transition matrix H_t gives rise to inaccurate residual error so that the residual error fails to correct the state estimation. To date, much research has focused on reducing the uncertainty of the extended Kalman filter.

In the end of this chapter, an adaptive extended Kalman filter was introduced, and it is basically a combination of an optimization algorithm and the extended Kalman filter. The adaptive extended Kalman filter will be widely employed throughout the simulation part in Chapter 4.

Chapter 4

Numerical Simulation and Results

In this chapter, linear and nonlinear structures with single-degree-of-freedom (SDOF) and multi-degree-of-freedom (MODF) will be simulated. The input control force is El Centro earthquake throughout all the simulation cases. The El Centro earthquake accelerogram is shown in Figure 4-1. The adaptive extended Kalman filter was implemented for estimating constant parameters in nonlinear systems and time-varying parameters in both linear and nonlinear systems. The E_0, F_0, and z in Equation 3.85 were selected to be 0, 0, and 0.5, respectively, for all the simulation cases which utilize the adaptive extended Kalman filter. The tolerance error δ in Equation 3.82 was set to be 10^{-4} and the sampling frequency is $200Hz$. Measurements having different levels of white noise were considered to evaluate the effects of noise on parametric estimations. Simulation results with different levels of noise covariance were also presented to determine which noise covariance is the best selection for our models. Models without adding additional noise, with Signal to Noise Ratio (SNR)=50 noise, and with SNR=20 noise were performed for all cases. For evaluating the effects of measurement noise covariance, the process noise covariance was fixed to be $10^{-7}\mathbf{I}$ throughout the whole cases. For evaluating the effects of process noise covariance, the measurement noise covariance was fixed to be $1\mathbf{I}$.

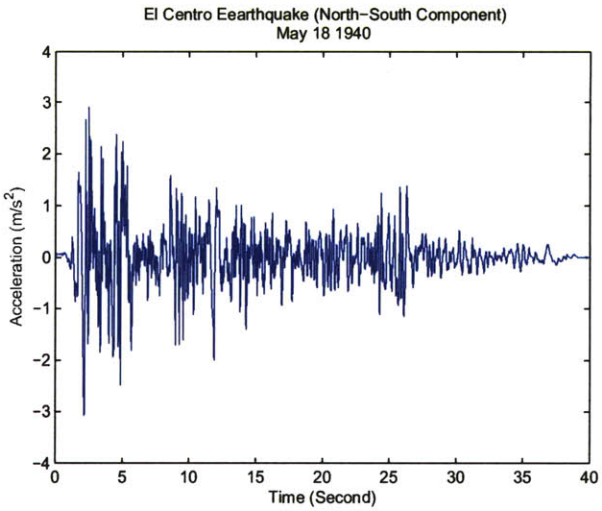

Figure 4-1: El Centro earthquake accelerogram.

4.1 Single-Degree-of-Freedom Model

Both linear and nonlinear elastic structures were considered in this section, and Matlab codes were programmed to perform these simulations. The properties of the structural models and simulation results were presented as follows.

4.1.1 Linear Elastic Structure

In order to compute the displacements, velocities, and accelerations of a structure due to a ground excitation (earthquake), the dynamic motion equation of a structure was implemented in SIMULINK. Consider the motion of equation of a linear SDOF structure subjected to an earthquake acceleration a_g is given by

$$m\ddot{x} + c\dot{x} + kx = -ma_g \tag{4.1}$$

where m is mass; c is damping coefficient; k is stiffness; and $\ddot{x}$, $\dot{x}$,and x are accelerations, velocities, and displacements, respectively. Equation 4.1 can be described in

state space representation as mentioned in Chapter 3:

$$X = \begin{bmatrix} \dot{x} \\ \ddot{x} \end{bmatrix} = \begin{bmatrix} 0 & \mathbf{I} \\ -m^{-1}k & -m^{-1}c \end{bmatrix} \begin{bmatrix} x \\ \dot{x} \end{bmatrix} + \begin{bmatrix} 0 \\ -m \end{bmatrix} a_g \tag{4.2}$$

In our linear SDOF structural model, the state vector and measured quantity can be described as

$$X = \begin{bmatrix} x \\ \dot{x} \\ k \\ c \end{bmatrix} = \begin{bmatrix} x_1 \\ x_2 \\ x_3 \\ x_4 \end{bmatrix} \tag{4.3}$$

$$\dot{X} = \begin{bmatrix} \dot{x} \\ \ddot{x} \\ \dot{k} \\ \dot{m} \end{bmatrix} + w(t) = \begin{bmatrix} x_2 \\ -a_g - (x_4 x_2 + x_3 x_1)/m \\ 0 \\ 0 \end{bmatrix} + w(t) \tag{4.4}$$

$$y = \ddot{x} + a_g + v(t) = -(x_4 x_2 + x_3 x_1)/m + v(t) \tag{4.5}$$

Note that k and m are the unknown parameters desired to be identified. The structural properties of the model are shown in Table 4.1.

Table 4.1: Structural properties of the linear SDOF model.

Structural Properties	Magnitudes	Units
m	500	kg
k	50000	N/m
c	300	Ns/m

Estimated parameters can be obtained by plugging Equation 4.4 and 4.5 into the

ordinary Kalman filter algorithm and incorporating initial estimations of state space variables. The initial estimations of state space variables do not need to be close to the true values because the Kalman filter can recursively correct the predicted values and eventually produce the accurate values. Table 4.2 shows the initial estimations of this model.

Table 4.2: Initial estimations for state parameters of the linear SDOF model.

State parameters	Magnitudes	Units
x	0	m
$\dot{x}$	0	m/s
k	30000	N/m
c	200	Ns/m

Two tuned noise covariances (measurement noise covariance and process noise covariance) were selected as shown in Table 4.3. A discussion on influences of different levels of noise covariances will be followed.

Table 4.3: Noise covariances of the linear SDOF model.

Noise covariances	Magnitudes
Measurement	1
Process	$10^{-7}\mathbf{I}_4$

The initial selection of the error covariance $P_{0|0}$ only effects the convergent speed [5], and we selected $P_{0|0} = diag[1, 1, 10^7, 10^7]$ for this case. In order to know the effects of noise on estimated results, noise of SNR equals to 20 (5% noise) and 50 (2% noise) were added to the measured acceleration. Due to the high quality of sensors manufacturing, the nosie produced by sensors is very small; therefore, SNR equals to 20 and 50 are actually overestimated. Figure 4-2 and 4-3 show the estimated values of stiffness and damping coefficient with different levels of noise.

The results show that the Kalman filter accurately estimates stiffness, but consistently overestimates damping. The reason why the damping coefficient was not estimated accurately is because the damping in a structure is usually small (3 to 5%) and this makes it difficult to estimate correctly. Obviously, the Kalman filter can filter out noise and produce accurate results.

Estimated stiffness and damping coefficient from different levels of noise with measurement noise covariance R equals to 0.1, 1, 10, 100 and process noise covariance Q equals to $10^{-5}\mathbf{I}_4$, $10^{-6}\mathbf{I}_4$, $10^{-7}\mathbf{I}_4$, $10^{-8}\mathbf{I}_4$ are presented. Figure 4-4 and 4-5 show the effects of R on estimating stiffness and damping coefficient for the case of SNR=20; Figure 4-6 and 4-7 show the results for the case of SNR=50.

Figure 4-8 and 4-9 show the effects of Q on estimated stiffness and damping coefficient for SNR=20 case. Figure 4-10 and 4-11 show the results for SNR=50 case. It was found that smaller R and Q can produce better estimations and quicker convergence on both estimated stiffness and damping coefficient.

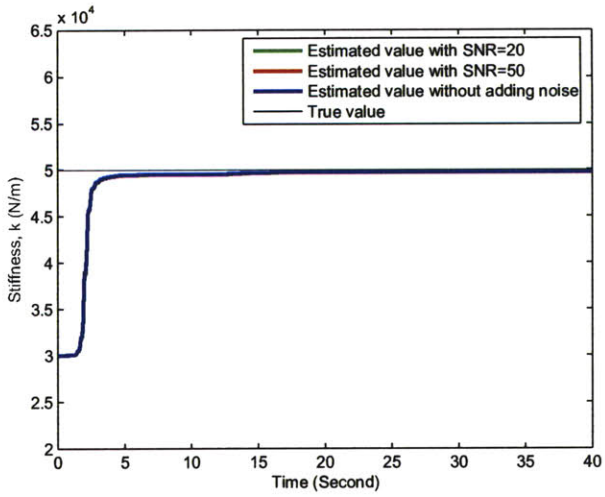

Figure 4-2: Comparison of estimated stiffness of the linear SDOF model with different levels of noise.

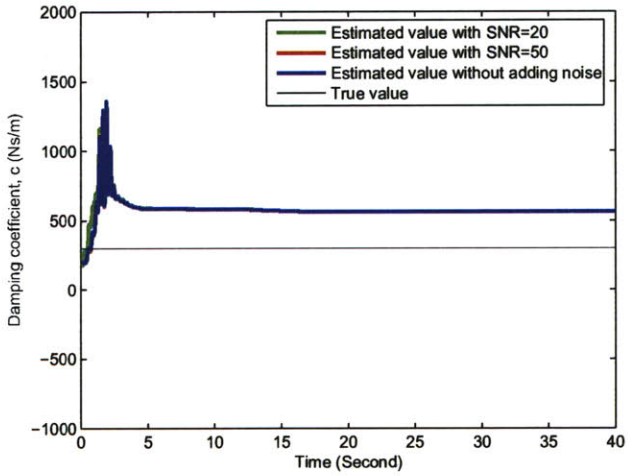

Figure 4-3: Comparison of estimated damping coefficient of the linear SDOF model with different levels of noise.

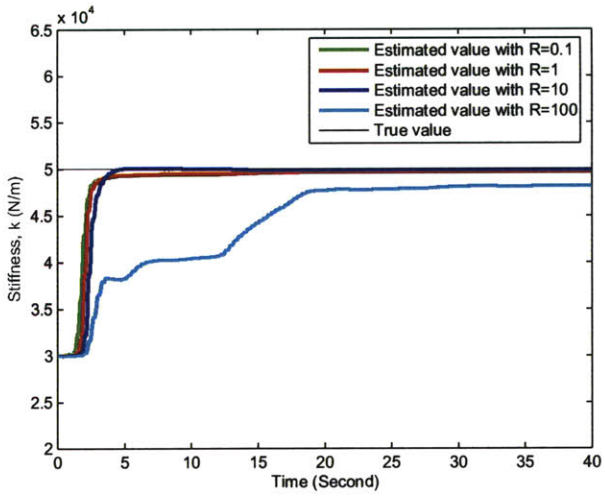

Figure 4-4: Comparison of estimated stiffness with different levels of measurement noise covariance (R) of the linear SDOF model (SNR=20).

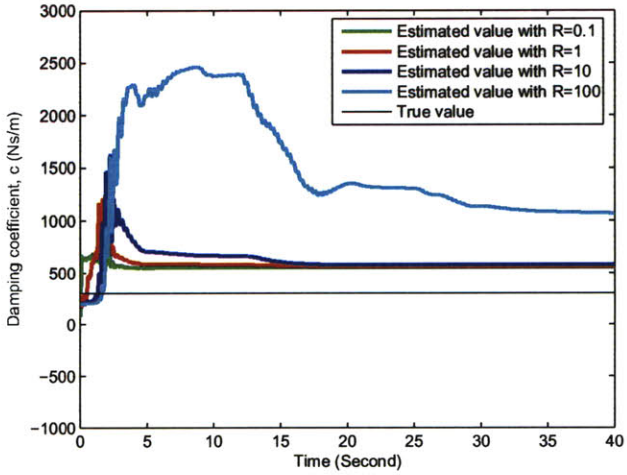

Figure 4-5: Comparison of estimated damping coefficient with different levels of measurement noise covariance (R) of the linear SDOF model (SNR=20).

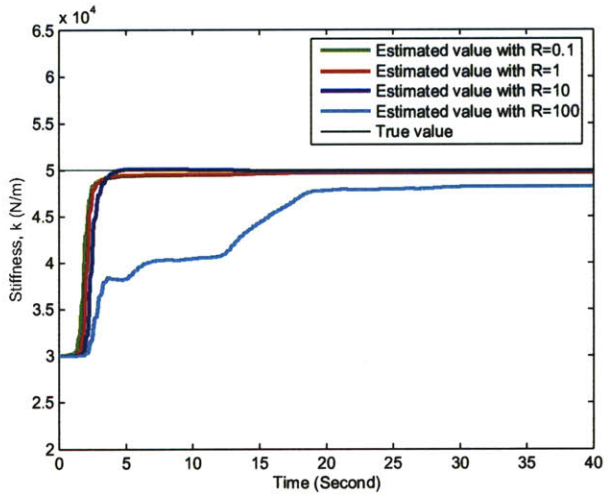

Figure 4-6: Comparison of estimated stiffness with different levels of measurement noise covariance (R) of the linear SDOF model (SNR=50).

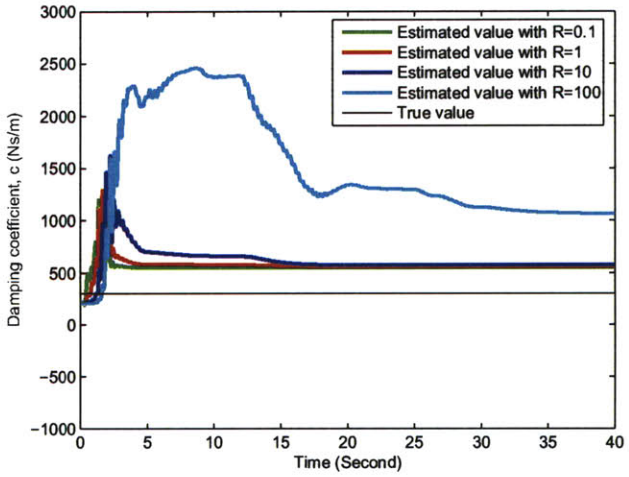

Figure 4-7: Comparison of estimated damping coefficient with different levels of measurement noise covariance (R) of the linear SDOF model (SNR=50).

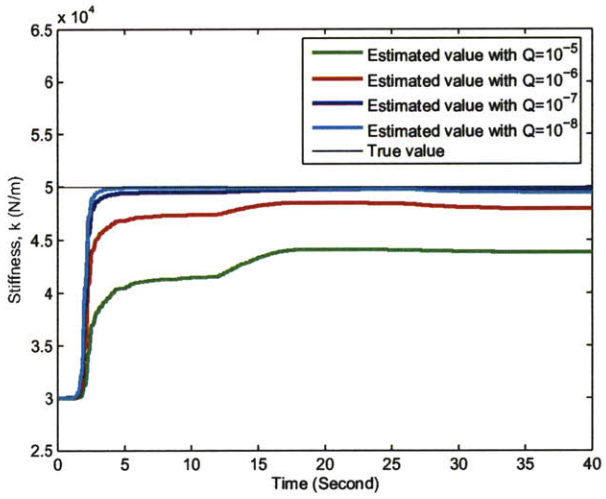

Figure 4-8: Comparison of estimated stiffness with different levels of process noise covariance (Q) of the linear SDOF model (SNR=20).

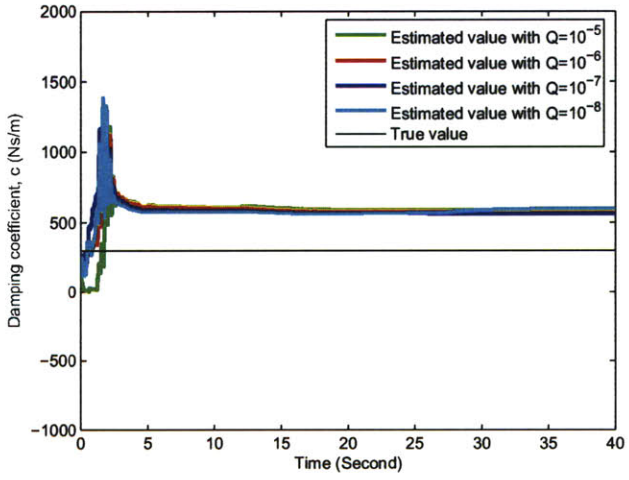

Figure 4-9: Comparison of estimated damping coefficient with different levels of process noise covariance (Q) of the linear SDOF model (SNR=20).

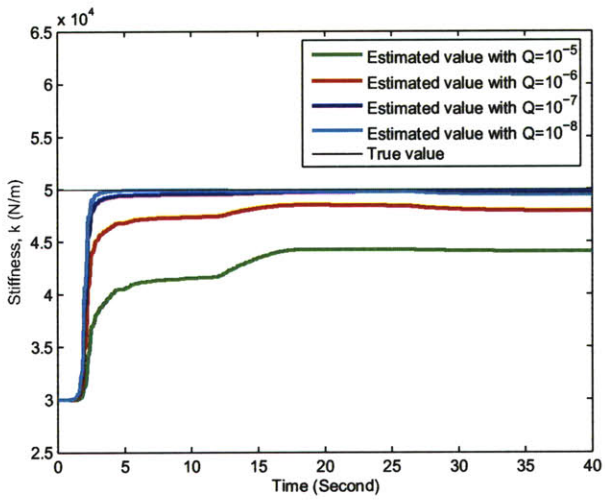

Figure 4-10: Comparison of estimated stiffness with different levels of process noise covariance (Q) of the linear SDOF model (SNR=50).

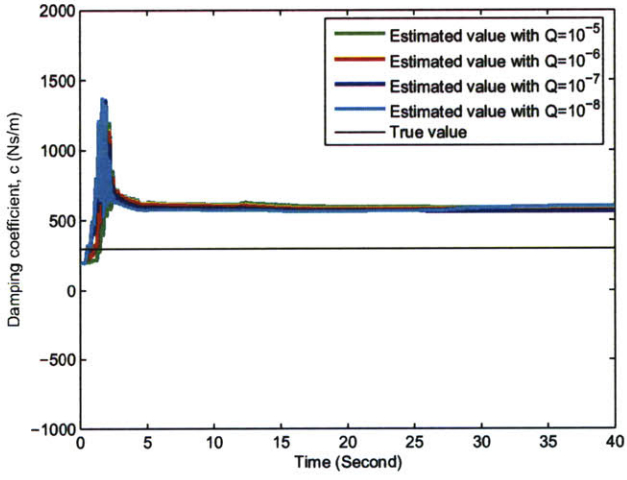

Figure 4-11: Comparison of estimated damping coefficient with different levels of process noise covariance (Q) of the linear SDOF model (SNR=50).

For simulating damage in a structure, a sigmoid function was adopted to illustrate a sudden change in stiffness. A sigmoid function is a mathematical function which can be described as

$$S(t) = \frac{1}{1 + e^{-a(x-c)}} \tag{4.6}$$

where a controls the slope and c controls the position. Figure 4-12 shows a sigmoid function with $a = -5$ and $c = 1$. Sigmoid functions are differentiable throughout the function and have either a non-positive or non-negative slope only.

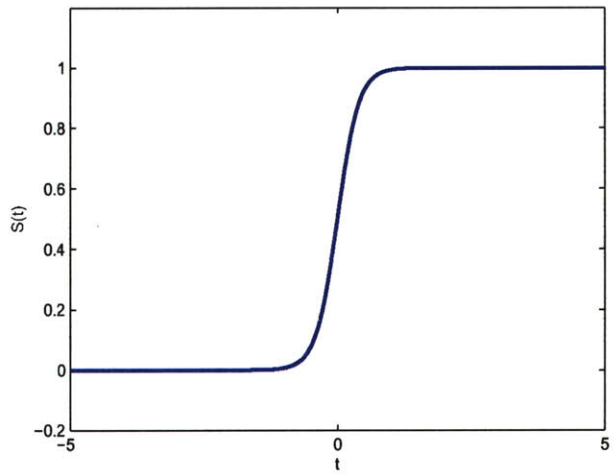

Figure 4-12: Sigmoid function.

A sudden change of stiffness from $50kN/m$ to $40kN/m$ was applied to the model. All the initial settings and selections are same as the model with constant stiffness. For estimating a sudden change in stiffness, the adaptive extended Kalman filter has to be implemented.

Figure 4-13 and 4-14 show the results for different levels of noise with the noise covariance shown in Table 4.3. It was found that the adaptive extended Kalman filter can track the changing stiffness well, but for the case of SNR=20, there exists slight instability after the stiffness drops.

Figure 4-15 and 4-16 show the results of different levels of measurement noise covariance for the case of SNR=20 with $Q = 10^{-7}\mathbf{I}_4$. Figure 4-17 and 4-18 show the results of different levels of measurement noise covariance for the case of SNR=50 with $Q = 10^{-7}\mathbf{I}_4$. From the figures, we found that for the case of SNR=20, larger R can produce better estimations, but for the case of SNR=50, noise is too small to affect the estimated values, as a result, it is not critical to select a particular R value.

Figure 4-19 and 4-20 show the results of different levels of process noise covariance for the case of SNR=20 with $R = 1$. Figure 4-21 and 4-22 show the results of different levels of process noise covariance for the case of SNR=50 with $R = 1$. The results reveal that a larger process noise covariance leads to less accurate estimations for the case of SNR=20. In particular, results from model with $Q = 10^{-5}\mathbf{I}_4$ are almost diverged. It was also found that different values of Q make no difference for SNR=50.

In summary, the ordinary Kalman filter produces the best performances on estimating stiffness and damping coefficient with process noise covariance being 10^{-8} and measurement noise covariance being 0.1; the adaptive extended Kalman filter used for simulating stiffness dropping generates the best performances with process noise covariance being 10^{-8} and measurement noise covariance being 100. As expected, a system with less noise is less affected by noise covariances.

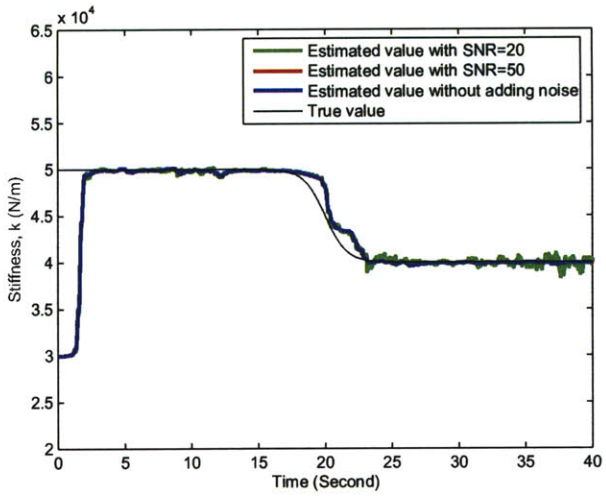

Figure 4-13: Comparison of estimated stiffness with different levels of noise for the cases of stiffness dropping of the linear SDOF model.

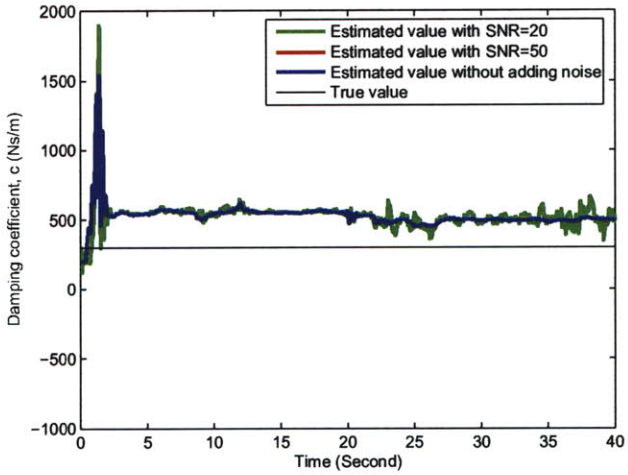

Figure 4-14: Comparison of estimated damping coefficient with different levels of noise for the case of stiffness dropping of the linear SDOF model.

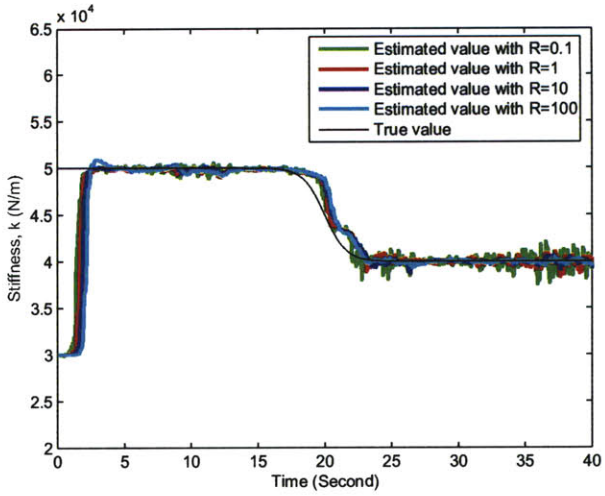

Figure 4-15: Comparison of estimated stiffness with different levels of measurement noise covariance (R) for the case of stiffness dropping of the linear SDOF model (SNR=20).

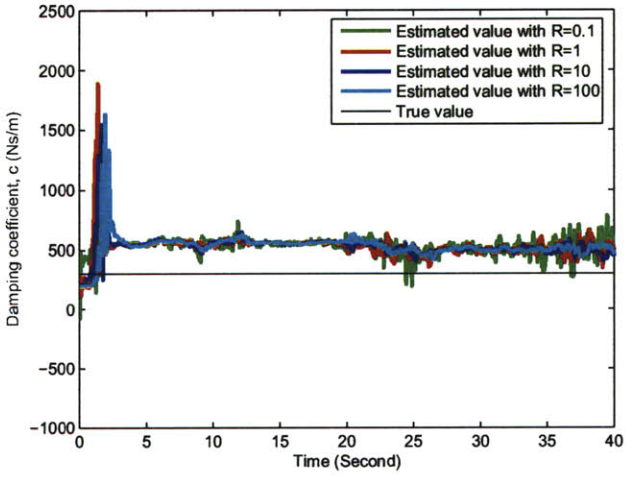

Figure 4-16: Comparison of estimated damping coefficient with different levels of measurement noise covariance (R) for the case of stiffness dropping of the linear SDOF model (SNR=20).

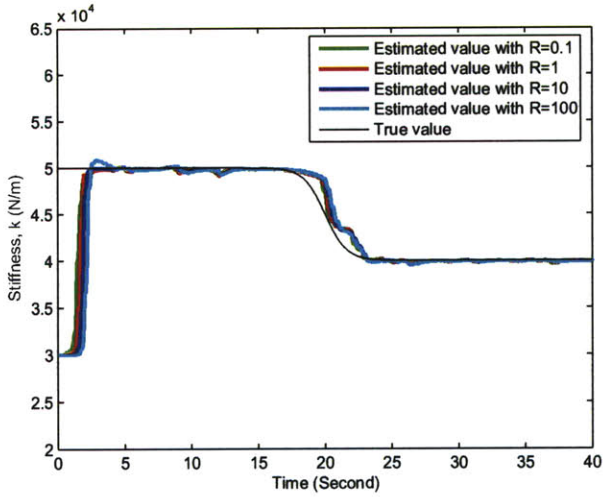

Figure 4-17: Comparison of estimated stiffness with different levels of measurement noise covariance (R) for the case of stiffness dropping of the linear SDOF model (SNR=50).

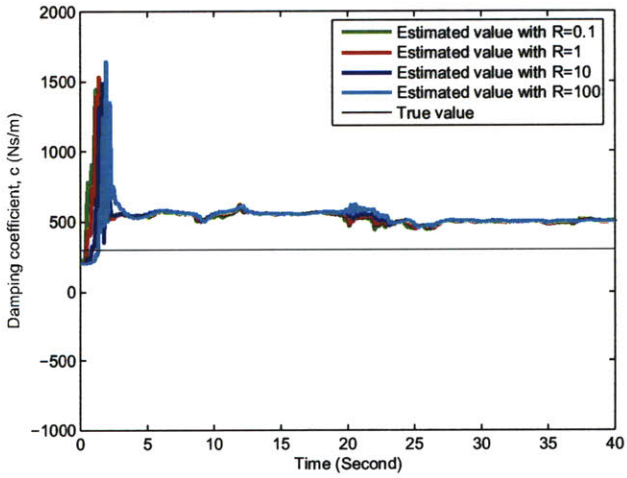

Figure 4-18: Comparison of estimated damping coefficient with different levels of measurement noise covariance (R) for the case of stiffness dropping of the linear SDOF model (SNR=50).

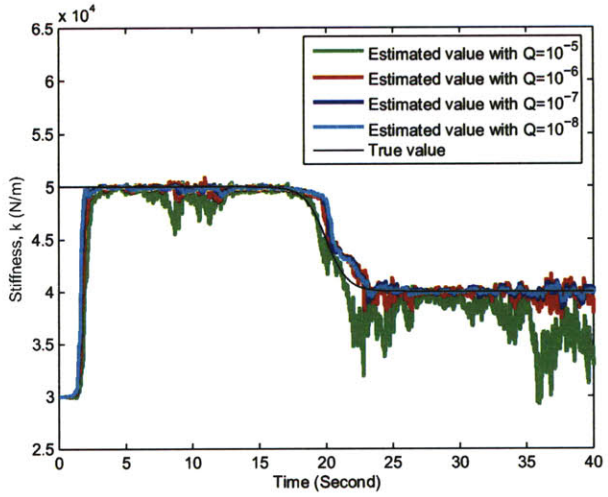

Figure 4-19: Comparison of estimated stiffness with different levels of process noise covariance (Q) for the case of stiffness dropping of the linear SDOF model (SNR=20).

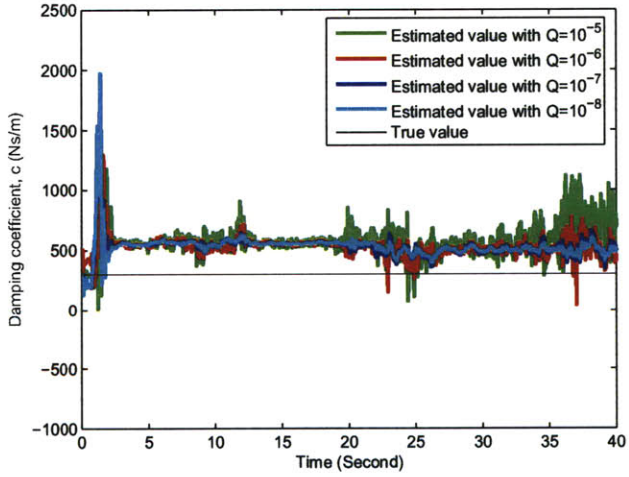

Figure 4-20: Comparison of estimated damping coefficient with different levels of process noise covariance (Q) for the case of stiffness dropping of the linear SDOF model (SNR=20).

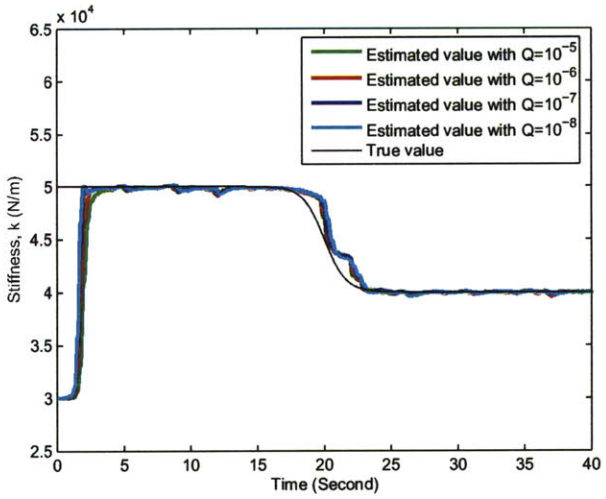

Figure 4-21: Comparison of estimated stiffness with different levels of process noise covariance (Q) for the case of stiffness dropping of the linear SDOF model (SNR=50).

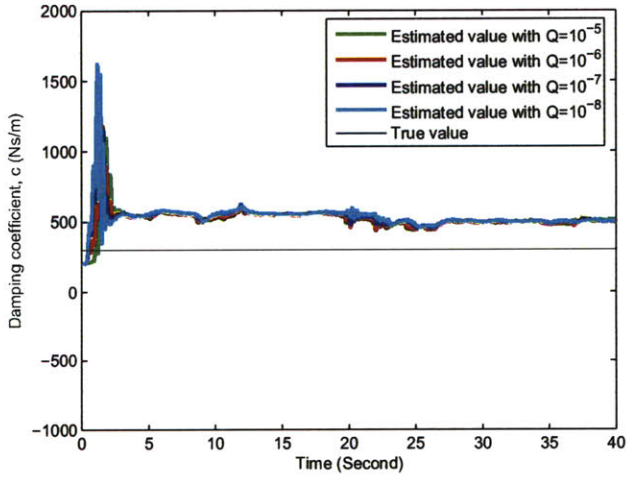

Figure 4-22: Comparison of estimated damping coefficient with different levels of process noise covariance (Q) for the case of stiffness dropping of the linear SDOF model (SNR=50).

4.1.2 Nonlinear Elastic Structure

The adaptive extended Kalman filter was implemented to perform parametric estimations for nonlinear elastic model, and the model was designed as

$$m\ddot{x} + c\dot{x} + k_1 x + k_2 x^2 = -ma_g \tag{4.7}$$

where m is mass; c is damping coefficient; k_1 is the stiffness related to linear terms; and k_2 is the stiffness related to nonlinear parts. Equation 4.7 can be written in state space representation:

$$\begin{aligned}\begin{bmatrix} \dot{x} \\ \ddot{x} \end{bmatrix} &= \begin{bmatrix} 0 & \mathbf{I} \\ -m^{-1}k_1 & -m^{-1}c \end{bmatrix} \begin{bmatrix} x \\ \dot{x} \end{bmatrix} \\ &+ \begin{bmatrix} 0 & 0 \\ -m^{-1}k_2 & 0 \end{bmatrix} \begin{bmatrix} x^2 \\ \dot{x}^2 \end{bmatrix} + \begin{bmatrix} 0 \\ -m \end{bmatrix} a_g \end{aligned} \tag{4.8}$$

The state vector and measured output are described as

$$X = \begin{bmatrix} x \\ \dot{x} \\ k_1 \\ k_2 \\ c \end{bmatrix} = \begin{bmatrix} x_1 \\ x_2 \\ x_3 \\ x_4 \\ x_5 \end{bmatrix} \tag{4.9}$$

$$\dot{X} = \begin{bmatrix} \dot{x} \\ \ddot{x} \\ \dot{k}_1 \\ \dot{k}_2 \\ \dot{c} \end{bmatrix} + w(t) = \begin{bmatrix} x_2 \\ -a_g - (x_5 x_2 + x_3 x_1 + x_4 x_1^2)/m \\ 0 \\ 0 \end{bmatrix} + w(t) \tag{4.10}$$

$$y = \ddot{x} + a_g + v(t) = -(x_4 x_2 + x_3 x_1 + x_4 x_1^2)/m + v(t) \tag{4.11}$$

The structural properties, initial estimations, and noise covariances are shown in Table 4.4, 4.5, and 4.6, respectively. The initial selection for the error covariance is $P_{0|0} = diag[1, 1, 10^7, 10^7, 10^7]$.

Table 4.4: Structural properties of the nonlinear SDOF model.

Structural Properties	Magnitudes	Units
m	500	kg
k_1	50000	N/m
k_2	50000	N/m
c	300	Ns/m

Table 4.5: Initial estimations for state parameters of the nonlinear SDOF model.

State parameters	Magnitudes	Units
x	0	m
$\dot{x}$	0	m/s
k_1	30000	N/m
k_2	30000	N/m
c	200	Ns/m

Table 4.6: Noise covariances of the nonlinear SDOF model.

Noise covariances	Magnitudes
Measurement	1
Process	$10^{-7}\mathbf{I}_5$

Figure 4-23, 4-24, and 4-25 show the estimated stiffness and damping coefficient of the nonlinear model with noise of SNR=20, noise of SNR=50, and noise free. It was found that for k_1 and c, the estimated values are acceptable for all levels of noise. However, noise with SNR=20 has a significant effect on the estimated k_2 leading to instability. The possible reason for that is because an earthquake consists of different levels of frequency, and the huge range of frequencies may give rise to inaccurate parametric estimations.

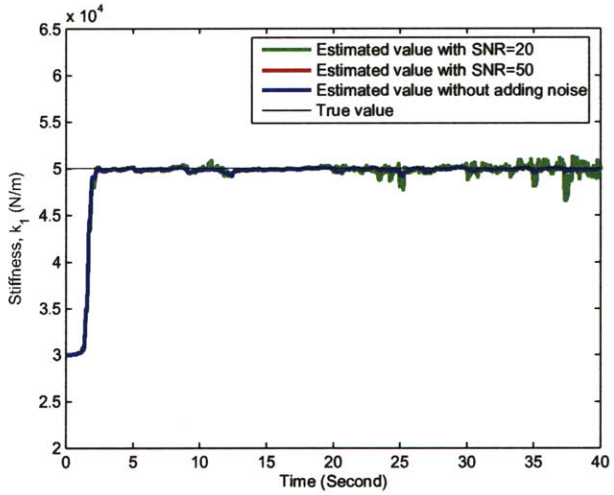

Figure 4-23: Comparison of estimated stiffness (k_1) of the nonlinear SDOF model with different levels of noise.

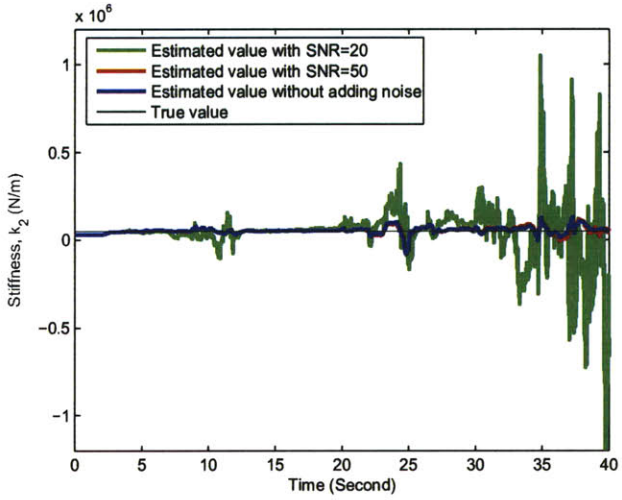

Figure 4-24: Comparison of estimated stiffness (k_2) of the nonlinear SDOF model with different levels of noise.

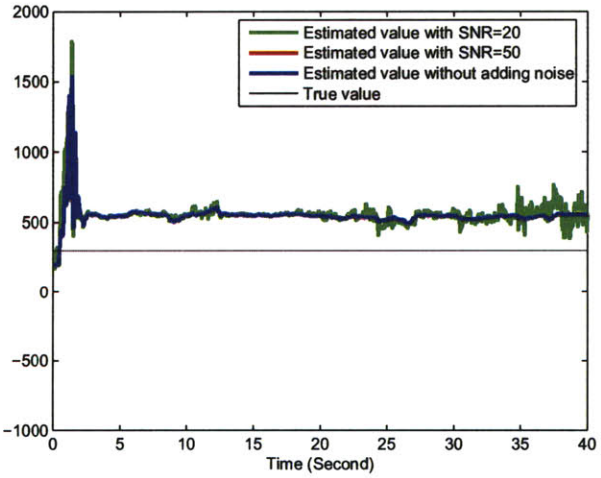

Figure 4-25: Comparison of estimated damping coefficient of the nonlinear SDOF model with different levels of noise.

Figure 4-26, 4-27, and 4-28 show the estimated results of different levels of measurement noise covariance for the case of noise with SNR=20 where the process noise covariance remains 10^{-7}. Figure 4-29, 4-30, and 4-31 show the estimated results for the case of noise with SNR=50. It was found that for the cases of SNR=20 the filter generates good estimations on k_1 and damping, but k_2 is unacceptable. For the cases of SNR=50, an arbitrary measurement noise covariance may be applied.

Figure 4-32 through 4-37 illustrates the impacts of different levels of process noise covariance on the simulated results for the cases of SNR=20 and 50. Similarly, the Q values are from $10^{-5}\mathbf{I}_5$ to $10^{-8}\mathbf{I}_5$ with an interval of $10^{-1}\mathbf{I}_5$, and the measurement noise covariance is set to be 1. As shown in the images for the case of SNR=20, a smaller process noise covariance generates better estimations on k_1 and damping, but k_2 diverges. For the case of SNR=50, there is no preference selection of process noise covariance.

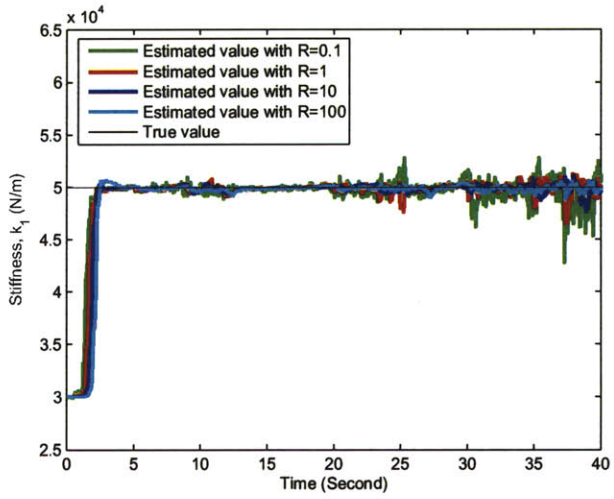

Figure 4-26: Comparison of estimated stiffness (k_1) with different levels of measurement noise covariance (R) of the nonlinear SDOF model (SNR=20).

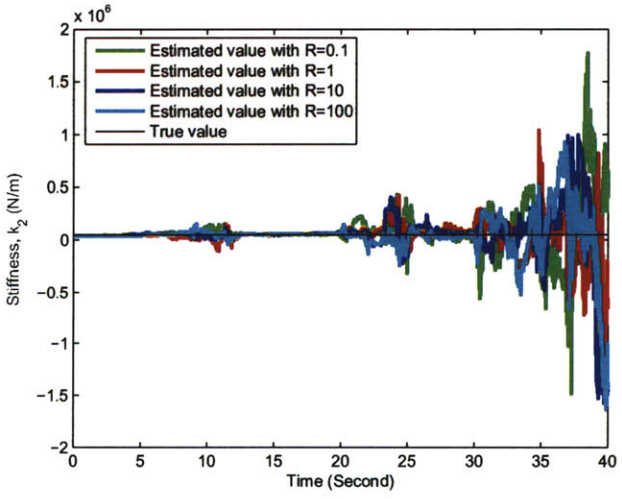

Figure 4-27: Comparison of estimated stiffness (k_2) with different levels of measurement noise covariance (R) of the nonlinear SDOF model (SNR=20).

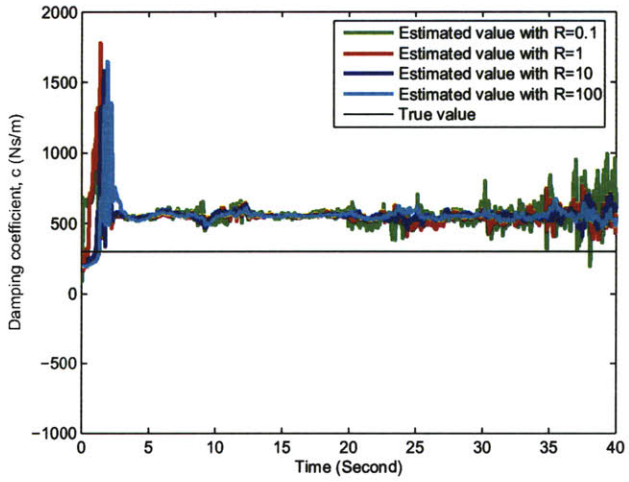

Figure 4-28: Comparison of estimated damping coefficient with different levels of measurement noise covariance (R) of the nonlinear SDOF model (SNR=20).

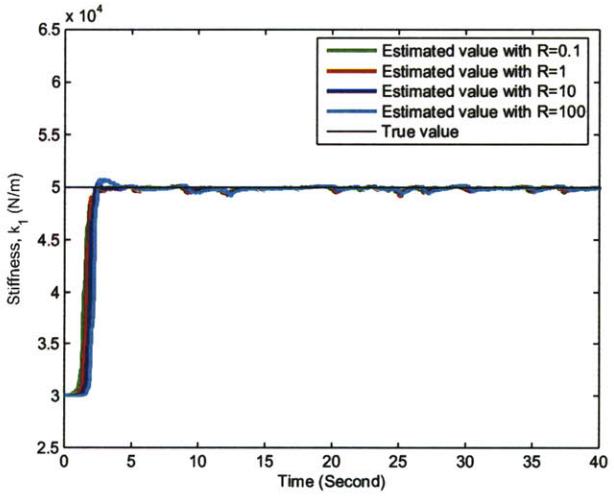

Figure 4-29: Comparison of estimated stiffness (k_1) with different levels of measurement noise covariance (R) of the nonlinear SDOF model (SNR=50).

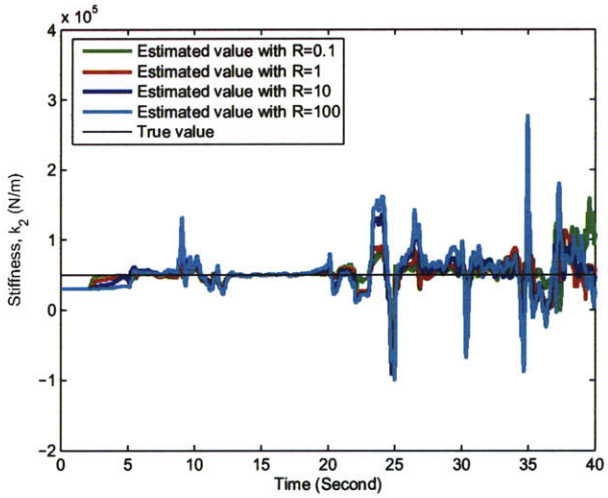

Figure 4-30: Comparison of estimated stiffness (k_2) with different levels of measurement noise covariance (R) of the nonlinear SDOF model (SNR=50).

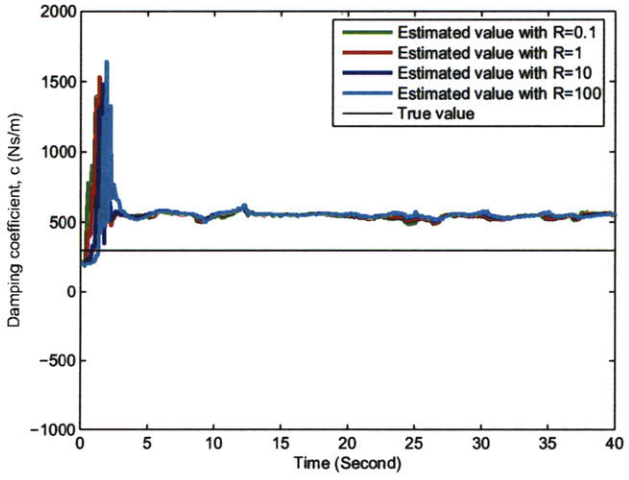

Figure 4-31: Comparison of estimated damping coefficient with different levels of measurement noise covariance (R) of the nonlinear SDOF model (SNR=50).

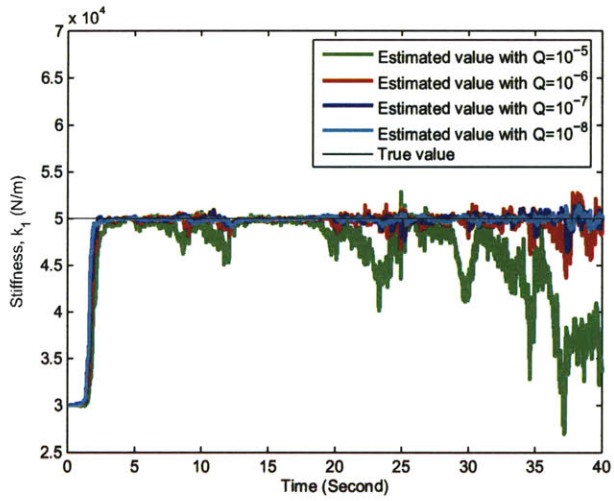

Figure 4-32: Comparison of estimated stiffness (k_1) with different levels of process noise covariance (Q) of the nonlinear SDOF model (SNR=20).

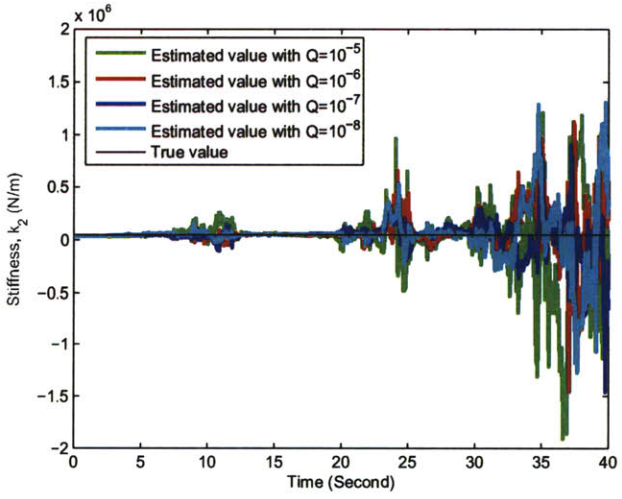

Figure 4-33: Comparison of estimated stiffness (k_2) with different levels of process noise covariance (Q) of the nonlinear SDOF model (SNR=20).

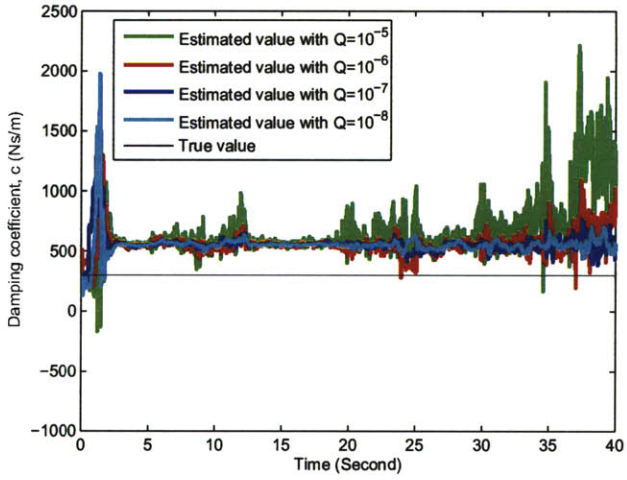

Figure 4-34: Comparison of estimated damping coefficient with different levels of process noise covariance (Q) of the nonlinear SDOF model (SNR=20).

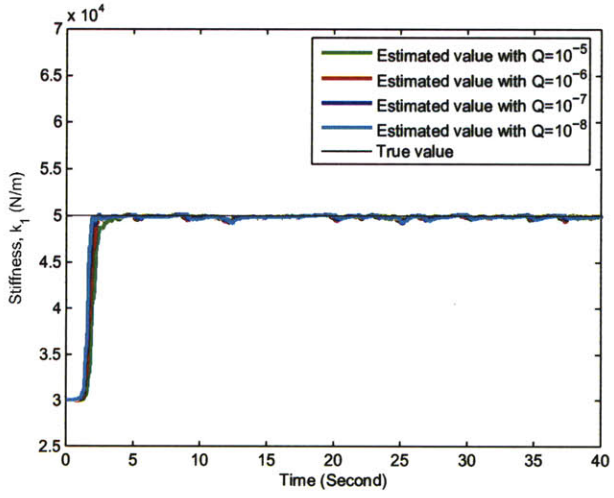

Figure 4-35: Comparison of estimated stiffness (k_1) with different levels of process noise covariance (Q) of the nonlinear SDOF model (SNR=50).

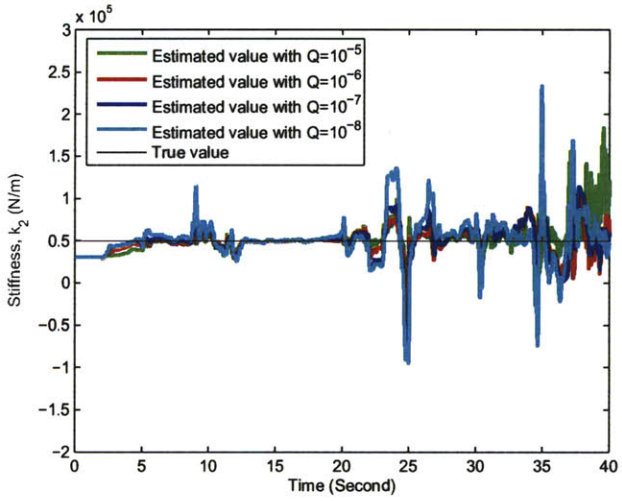

Figure 4-36: Comparison of estimated stiffness (k_2) with different levels of process noise covariance (Q) of the nonlinear SDOF model (SNR=50).

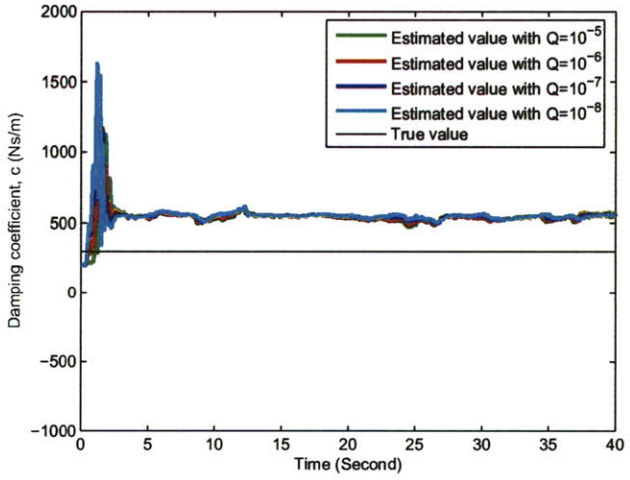

Figure 4-37: Comparison of estimated damping coefficient with different levels of process noise covariance (Q) of the nonlinear SDOF model (SNR=50).

Likewise, a simulated damage in a structure is performed. Stiffness k_1 in the nonlinear model is dropped from $50kN/m$ to $40kN/m$, and other structural characteristics remain unchanged. Figure 4-38 through 4-40 shows the results of different levels of external noise. Obviously, estimated stiffness k_1 is accurate, estimated damping is acceptable, but the filter does not work well on estimating stiffness k_2.

Figure 4-41 through 4-46 illustrates the estimated stiffness and damping coefficient for the noise-added model with different levels of measurement noise covariance where process noise covariance is fixed to be $10^{-7}\mathbf{I}_5$. The results show that for the case of SNR=20, a larger R makes the model more stable; however, estimated stiffness k_2 is diverged for all the selections of R. As for the case of SNR=50, a smaller Q generates better estimations on stiffness k_2. Hence, a smaller Q is preferred for low noise case.

Figure 4-47 through 4-52 presents the effects of different levels of process noise covariance with fixed $R = 1$. The results reveal that a smaller process noise covariance produces better estimations for the case of SNR=20. But for the case of SNR=50, a larger process noise covariance is preferred because it generates better estimations on stiffness k_2.

To summarize, for both constant and time-varying stiffness cases, process noise covariance being 10^{-8} and measurement noise covariance being 100 are the ones performing the best estimations. However, for stiffness related to nonlinear terms, the proposed filter does not work well.

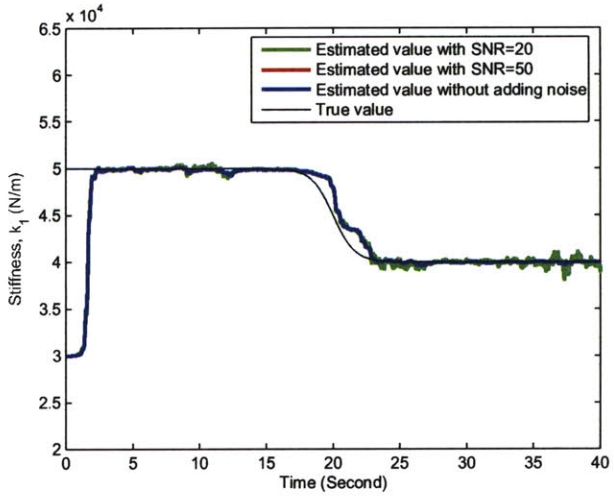

Figure 4-38: Comparison of estimated stiffness (k_1) with different levels of noise for the case of stiffness dropping of the nonlinear SDOF model.

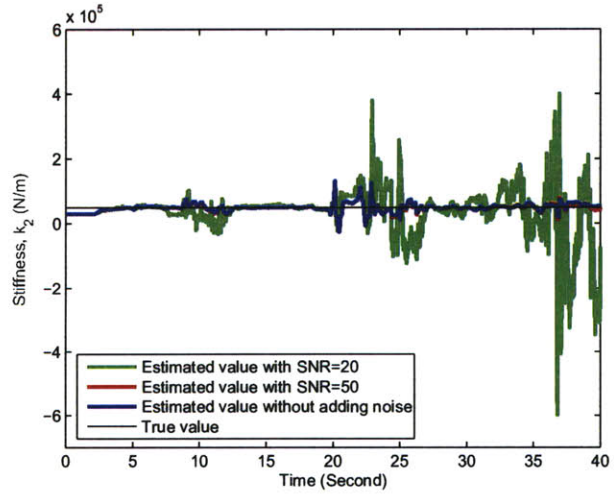

Figure 4-39: Comparison of estimated stiffness (k_2) with different levels of noise for the case of stiffness dropping of the nonlinear SDOF model.

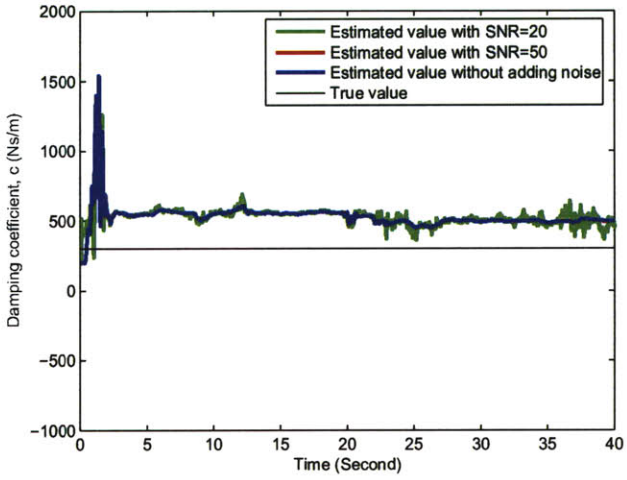

Figure 4-40: Comparison of estimated damping coefficient with different levels of noise for the case of stiffness dropping of the nonlinear SDOF model.

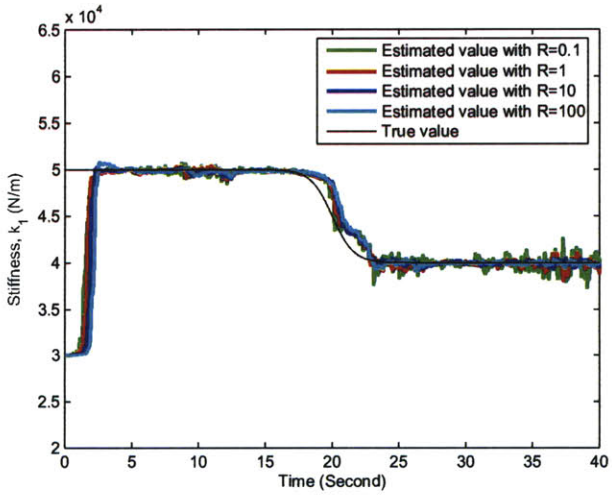

Figure 4-41: Comparison of estimated stiffness (k_1) with different levels of measurement noise covariance (R) for the case of stiffness dropping of the nonlinear SDOF model (SNR=20).

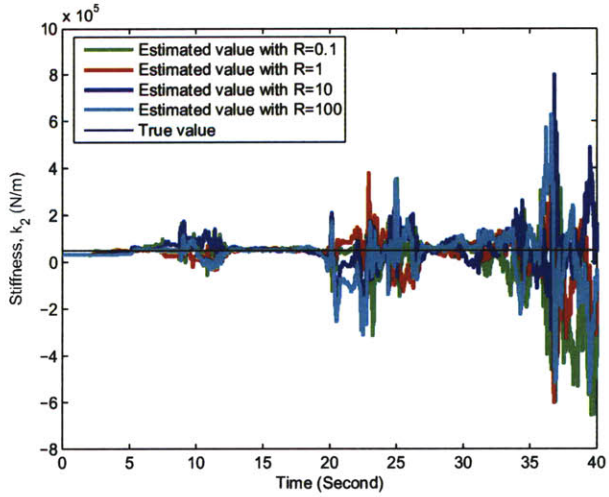

Figure 4-42: Comparison of estimated stiffness (k_2) with different levels of measurement noise covariance (R) for the case of stiffness dropping of the nonlinear SDOF model (SNR=20).

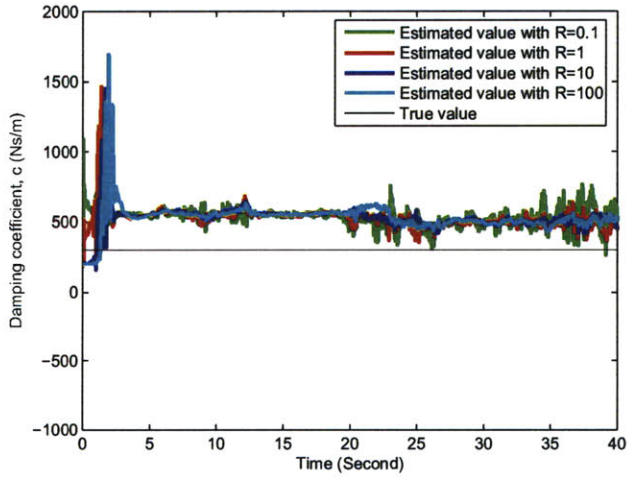

Figure 4-43: Comparison of estimated damping coefficient with different levels of measurement noise covariance (R) for the case of stiffness dropping of the nonlinear SDOF model (SNR=20).

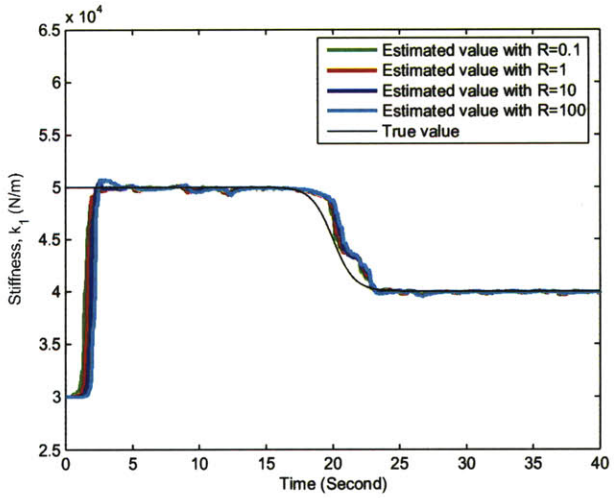

Figure 4-44: Comparison of estimated stiffness (k_1) with different levels of measurement noise covariance (R) for the case of stiffness dropping of the nonlinear SDOF model (SNR=50).

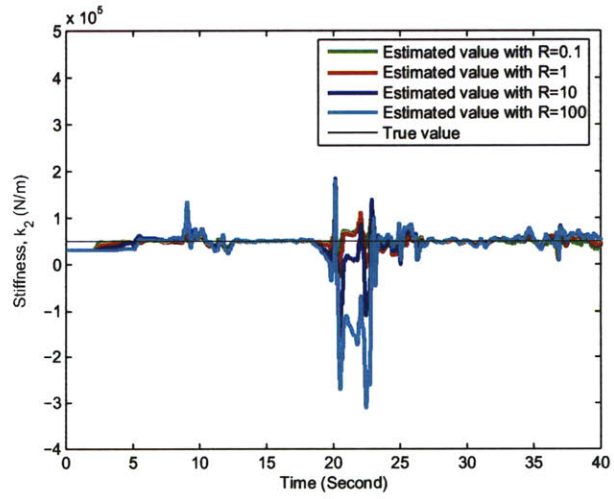

Figure 4-45: Comparison of estimated stiffness (k_2) with different levels of measurement noise covariance (R) for the case of stiffness dropping of the nonlinear SDOF model (SNR=50).

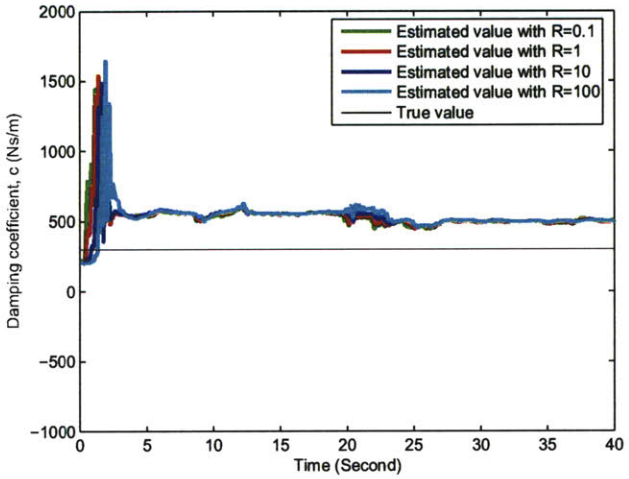

Figure 4-46: Comparison of estimated damping coefficient with different levels of measurement noise covariance (R) for the case of stiffness dropping of the nonlinear SDOF model (SNR=50).

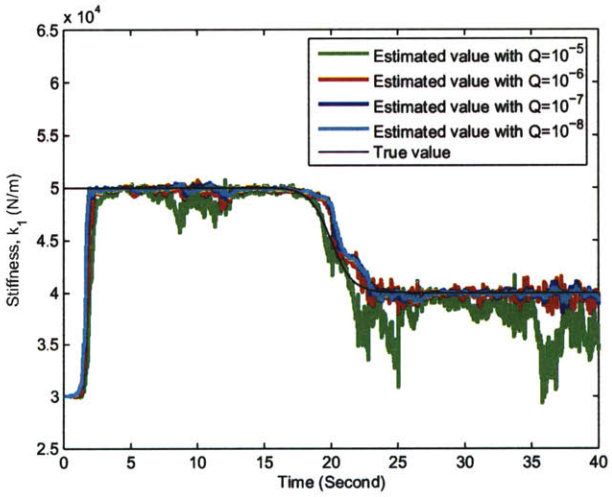

Figure 4-47: Comparison of estimated stiffness (k_1) with different levels of process noise covariance (Q) for the case of stiffness dropping of the nonlinear SDOF model (SNR=20).

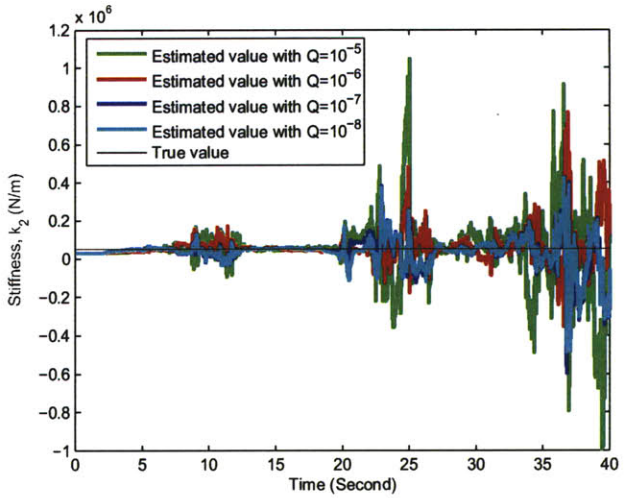

Figure 4-48: Comparison of estimated stiffness (k_2) with different levels of process noise covariance (Q) for the case of stiffness dropping of the nonlinear SDOF model (SNR=20).

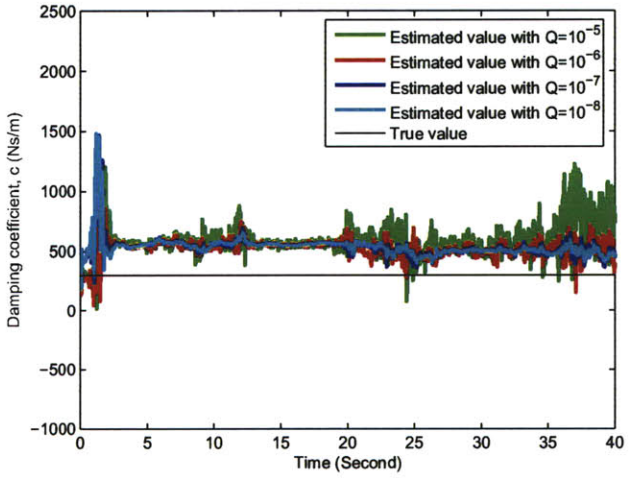

Figure 4-49: Comparison of estimated damping coefficient with different levels of process noise covariance (Q) for the case of stiffness dropping of the nonlinear SDOF model (SNR=20).

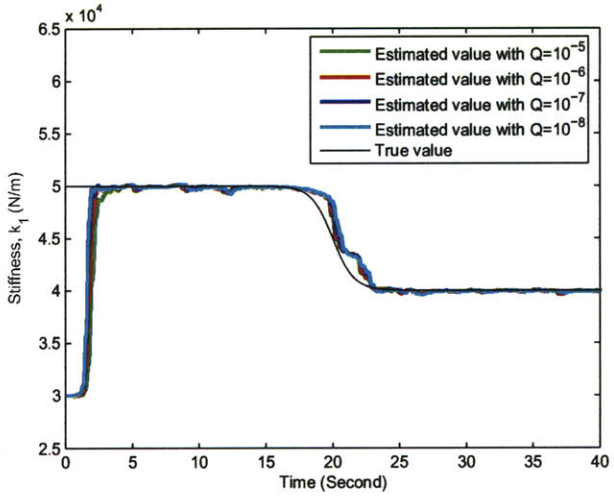

Figure 4-50: Comparison of estimated stiffness (k_1) with different levels of process noise covariance (Q) for the case of stiffness dropping of the nonlinear SDOF model (SNR=50).

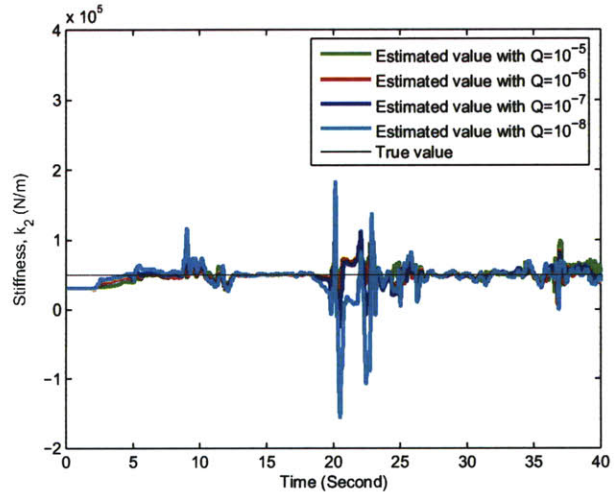

Figure 4-51: Comparison of estimated stiffness (k_2) with different levels of process noise covariance (Q) for the case of stiffness dropping of the nonlinear SDOF model (SNR=50).

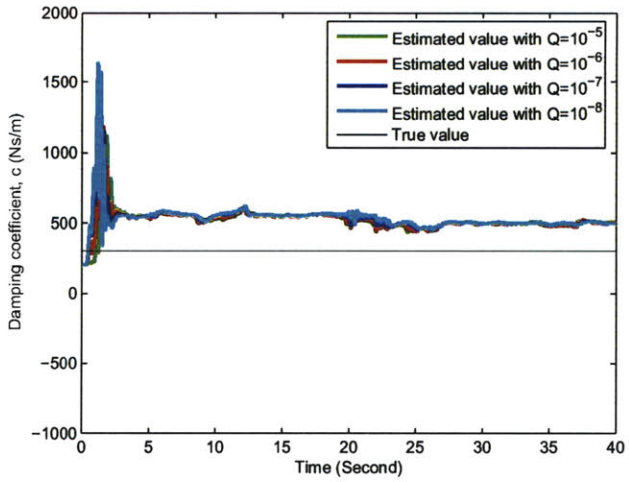

Figure 4-52: Comparison of estimated damping coefficient with different levels of process noise covariance (Q) for the case of stiffness dropping of the nonlinear SDOF model (SNR=50).

4.2 Multi-Degree-of-Freedom Model

In this section, a three-degree-of-freedom (3DOF) linear model and a two-degree-of-freedom (2DOF) nonlinear model are considered. The simulation results were carried out by implementing the adaptive extended Kalman filter to all cases.

4.2.1 Linear Elastic Structure

The motion of equations of a 3DOF linear elastic model, which is an imitation of a three-story building, subjected to an external excitation can be written in a state space representation as

$$\begin{bmatrix} m & 0 & 0 \\ 0 & m & 0 \\ 0 & 0 & m \end{bmatrix} \begin{bmatrix} \ddot{x}_1 \\ \ddot{x}_2 \\ \ddot{x}_3 \end{bmatrix} + \begin{bmatrix} c_1 + c_2 & -c_2 & 0 \\ -c_2 & c_2 + c_3 & -c_3 \\ 0 & -c_3 & c_3 \end{bmatrix} \begin{bmatrix} \dot{x}_1 \\ \dot{x}_2 \\ \dot{x}_3 \end{bmatrix} + \begin{bmatrix} k_1 + k_2 & -k_2 & 0 \\ -k_2 & k_2 + k_3 & -k_3 \\ 0 & -k_3 & k_3 \end{bmatrix} \begin{bmatrix} x_1 \\ x_2 \\ x_3 \end{bmatrix} = -a_g \begin{bmatrix} m \\ m \\ m \end{bmatrix} \tag{4.12}$$

where k_1, k_2, and k_3 are the stiffness in the first, second, and third floor, respectively; likewise, c_1, c_2, and c_3 are the damping coefficient in the first, second , and third floor. The state space representation has the following state vector and measured output:

$$X = \begin{bmatrix} x_1 \\ x_2 \\ x_3 \\ \dot{x}_1 \\ \dot{x}_2 \\ \dot{x}_3 \\ k_1 \\ k_2 \\ k_3 \\ c_1 \\ c_2 \\ c_3 \end{bmatrix} = \begin{bmatrix} x_1 \\ x_2 \\ x_3 \\ x_4 \\ x_5 \\ x_6 \\ x_7 \\ x_8 \\ x_9 \\ x_{10} \\ x_{11} \\ x_{12} \end{bmatrix} \tag{4.13}$$

$$\dot{X} = \begin{bmatrix} \dot{x}_1 \\ \dot{x}_2 \\ \dot{x}_3 \\ \ddot{x}_1 \\ \ddot{x}_2 \\ \ddot{x}_3 \\ \dot{k}_1 \\ \dot{k}_2 \\ \dot{k}_3 \\ \dot{c}_1 \\ \dot{c}_2 \\ \dot{c}_3 \end{bmatrix} + w(t) = \begin{bmatrix} x_4 \\ x_5 \\ x_6 \\ -a_g - (x_{10}x_4 + x_7x_1)/m \\ -a_g - (x_{11}x_5 + x_8x_2)/m \\ -a_g - (x_{12}x_6 + x_9x_3)/m \\ 0 \\ 0 \\ 0 \\ 0 \\ 0 \\ 0 \end{bmatrix} + w(t) \tag{4.14}$$

$$Y = \begin{bmatrix} \ddot{x}_1 + a_g \\ \ddot{x}_2 + a_g \\ \ddot{x}_3 + a_g \end{bmatrix} + v(t) = \begin{bmatrix} -(x_{10}x_4 + x_7x_1)/m \\ -(x_{11}x_5 + x_8x_2)/m \\ -(x_{12}x_6 + x_9x_3)/m \end{bmatrix} + v(t) \tag{4.15}$$

where k and c are the parameters desired to be estimated. The structural properties, the initial estimations of the state parameters, and the noise covariances are stated in Table 4.7, 4.8,and 4.9, respectively. As for the initial error covariance, it was selected to be $P_{0|0} = diag[1, 1, 1, 1, 1, 1, 10^7, 10^7, 10^7, 10^7, 10^7, 10^7]$.

Table 4.7: Structural properties of the linear 3DOF model.

Structural Properties	Magnitudes	Units
m	500	kg
$k_1 = k_2 = k_3$	50000	N/m
$c_1 = c_2 = c_3$	300	Ns/m

Table 4.8: Initial estimations for state parameters of the linear 3DOF model.

State parameters	Magnitudes	Units
$x_1 = x_2 = x_3$	0	m
$\dot{x}_1 = \dot{x}_2 = \dot{x}_3$	0	m/s
$k_1 = k_2 = k_3$	30000	N/m
$c_1 = c_2 = c_3$	200	Ns/m

Table 4.9: Noise covariances of the linear 3DOF model.

Noise covariances	Magnitudes
Measurement	$1\mathbf{I}_3$
Process	$10^{-7}\mathbf{I}_{12}$

As shown in Figure 4-53 through 4-58, the adaptive extended Kalman filter generates an accurate estimation on stiffness, although there is an over estimation on damping coefficient. It was also found that the model with noise of SNR=20 is less stable than the others, but it basically gives acceptable estimations.

Figure 4-59 through 4-64 shows the influences of different levels of measurement noise covariance with fixed process noise covariance $Q = 10^{-7}\mathbf{I}_{12}$ for the system with noise of SNR=20. As for the case of SNR=50, the results are shown in Figure 4-65 through 4-70. It was found that for the case of SNR=20, a larger measurement noise covariance produces better estimations, particularly for estimated k_3 and c_3. For the case of SNR=50, it seems there is no significant difference using different values of R.

Figure 4-71 through 4-76 illustrates the influences of different levels of process noise covariance with fixed measurement noise covariance $R = 1\mathbf{I}_3$ for the system with noise of SNR=20; Figure 4-77 through 4-82 shows the results for the case of SNR=50. Obviously, a larger process noise covariance results in better estimations, especially for estimating k_3, c_2, and c_3. For the case of SNR=50, influences due to different levels of process noise covariance is inconspicuous.

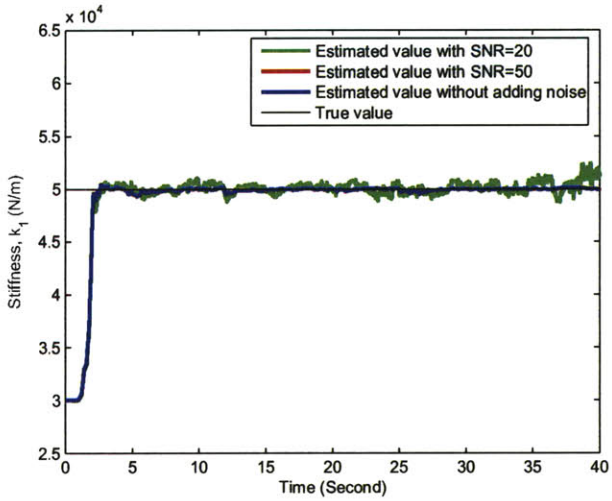

Figure 4-53: Comparison of estimated stiffness (k_1) of the linear 3DOF model with different levels of noise.

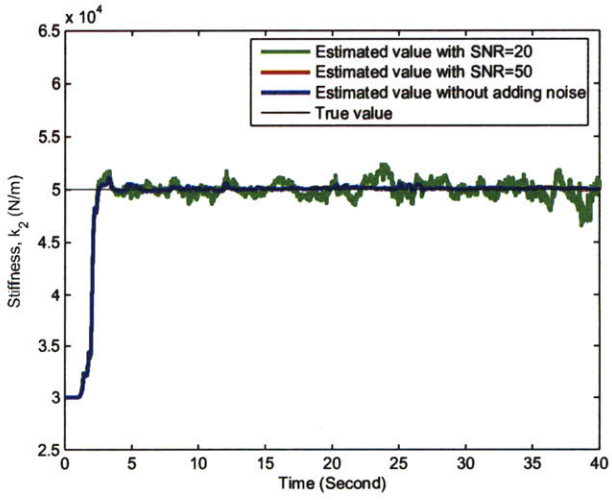

Figure 4-54: Comparison of estimated stiffness (k_2) of the linear 3DOF model with different levels of noise.

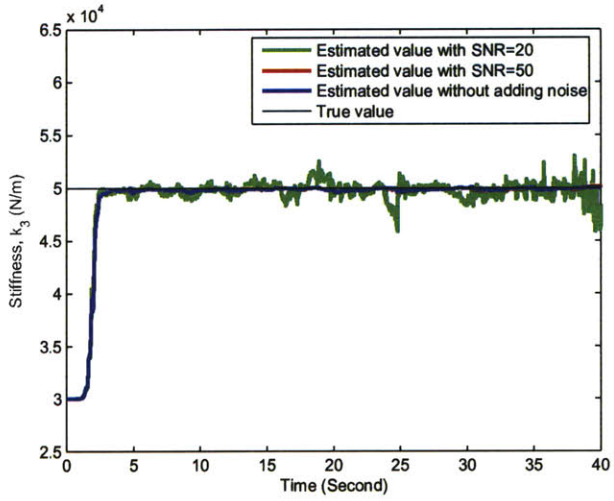

Figure 4-55: Comparison of estimated stiffness (k_3) of the linear 3DOF model with different levels of noise.

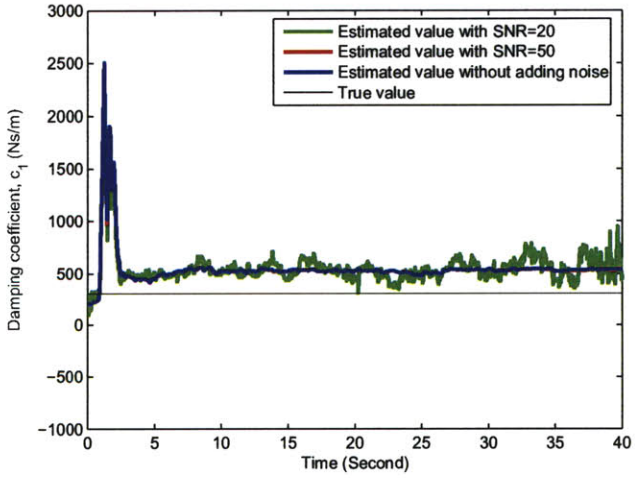

Figure 4-56: Comparison of estimated damping coefficient (c_1) of the linear 3DOF model with different levels of noise.

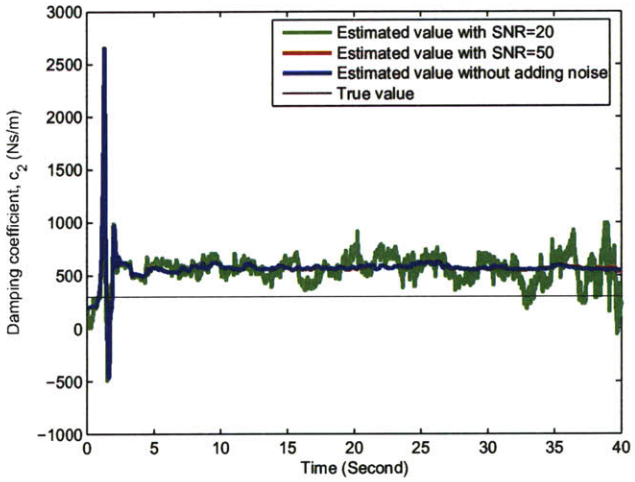

Figure 4-57: Comparison of estimated damping coefficient (c_2) of the linear 3DOF model with different levels of noise.

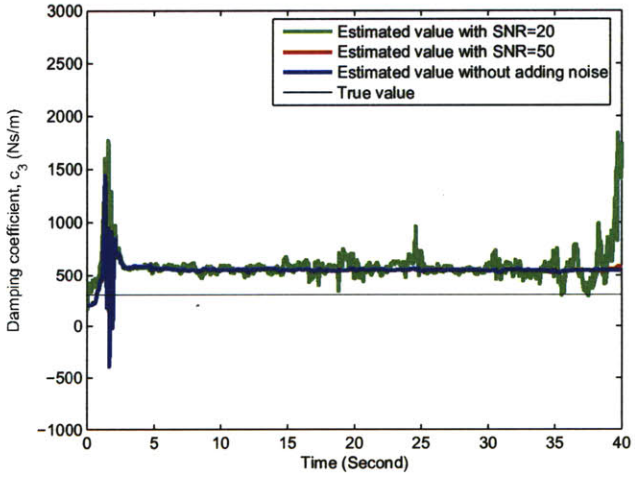

Figure 4-58: Comparison of estimated damping coefficient (c_3) of the linear 3DOF model with different levels of noise.

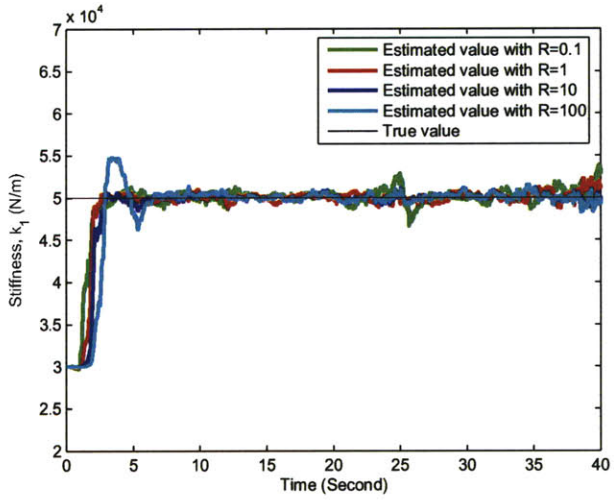

Figure 4-59: Comparison of estimated stiffness (k_1) with different levels of measurement noise covariance (R) of the linear 3DOF model (SNR=20).

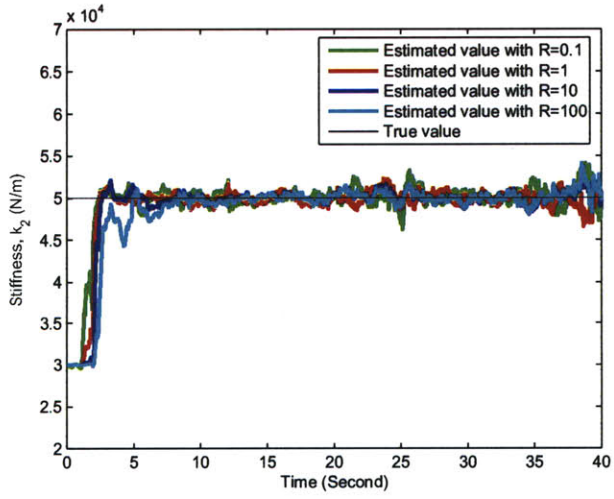

Figure 4-60: Comparison of estimated stiffness (k_2) with different levels of measurement noise covariance (R) of the linear 3DOF model (SNR=20).

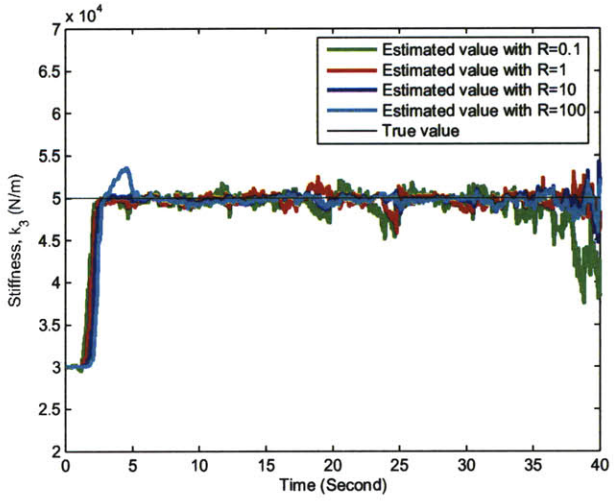

Figure 4-61: Comparison of estimated stiffness (k_3) with different levels of measurement noise covariance (R) of the linear 3DOF model (SNR=20).

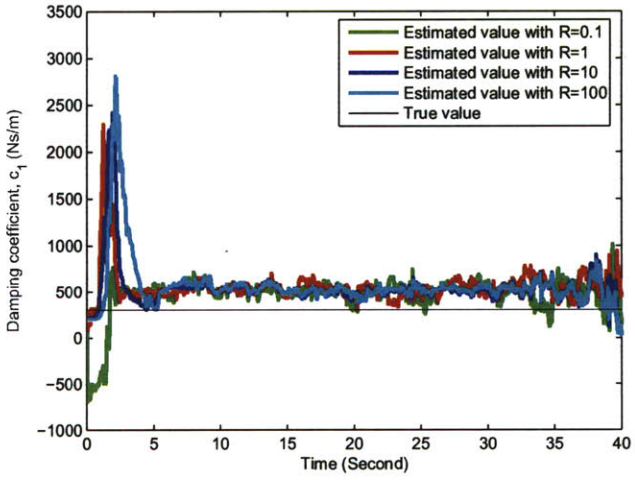

Figure 4-62: Comparison of estimated damping coefficient (c_1) with different levels of measurement noise covariance (R) of the linear 3DOF model (SNR=20).

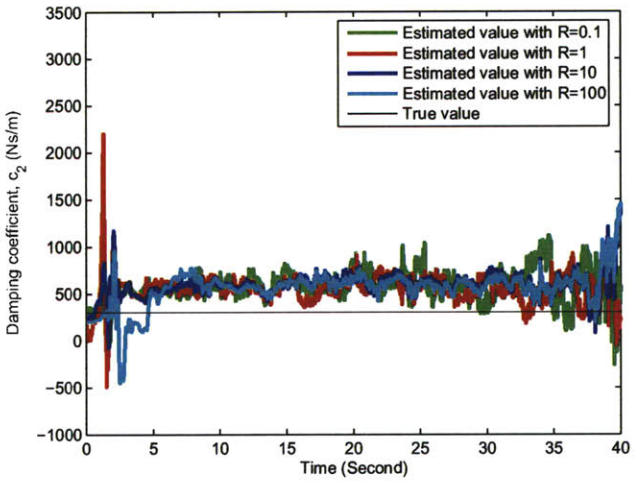

Figure 4-63: Comparison of estimated damping coefficient (c_2) with different levels of measurement noise covariance (R) of the linear 3DOF model (SNR=20).

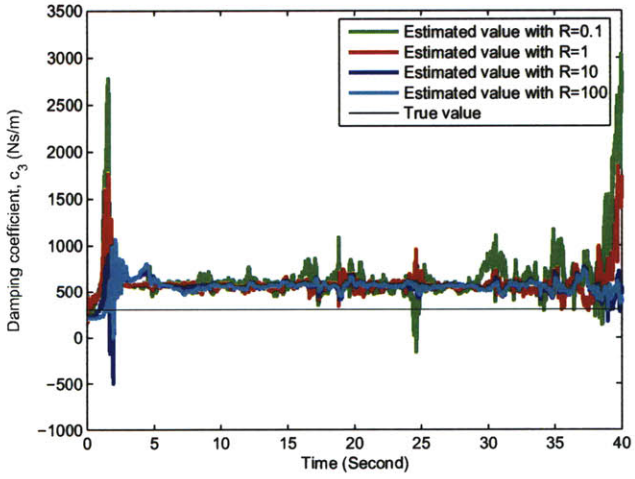

Figure 4-64: Comparison of estimated damping coefficient (c_3) with different levels of measurement noise covariance (R) of the linear 3DOF model (SNR=20).

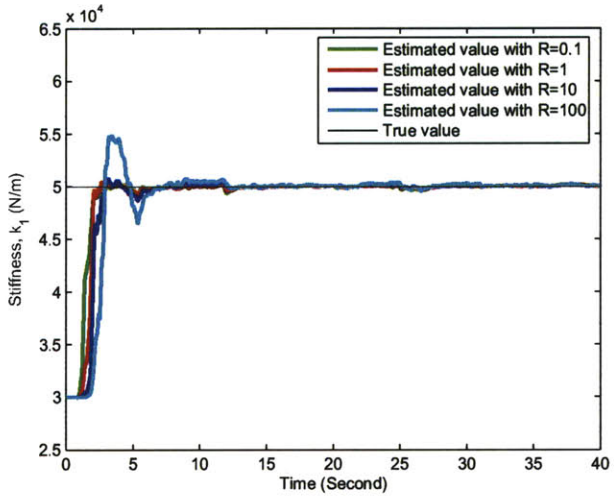

Figure 4-65: Comparison of estimated stiffness (k_1) with different levels of measurement noise covariance (R) of the linear 3DOF model (SNR=50).

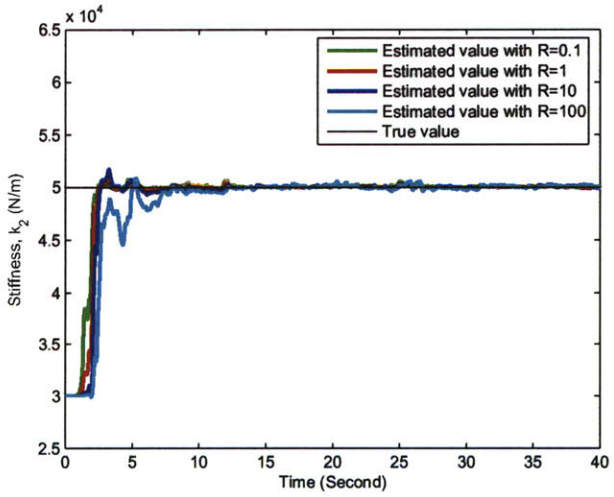

Figure 4-66: Comparison of estimated stiffness (k_2) with different levels of measurement noise covariance (R) of the linear 3DOF model (SNR=50).

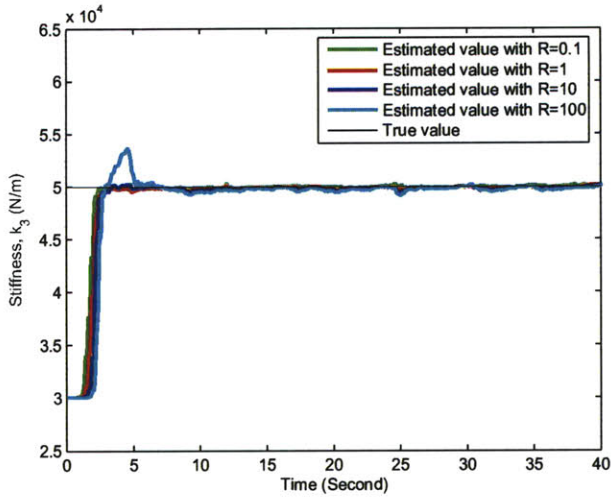

Figure 4-67: Comparison of estimated stiffness (k_3) with different levels of measurement noise covariance (R) of the linear 3DOF model (SNR=50).

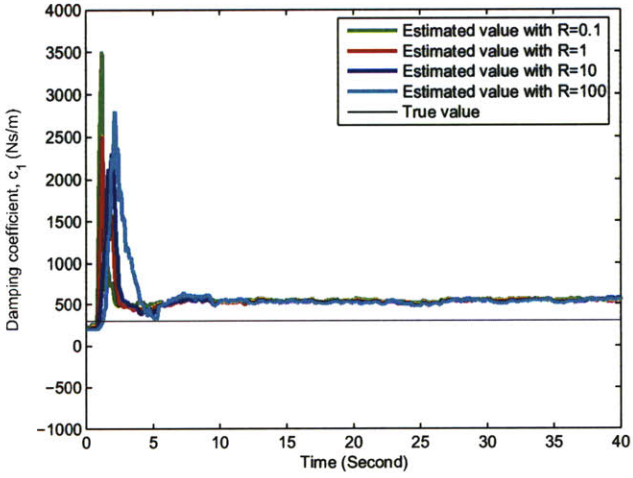

Figure 4-68: Comparison of estimated damping coefficient (c_1) with different levels of measurement noise covariance (R) of the linear 3DOF model (SNR=50).

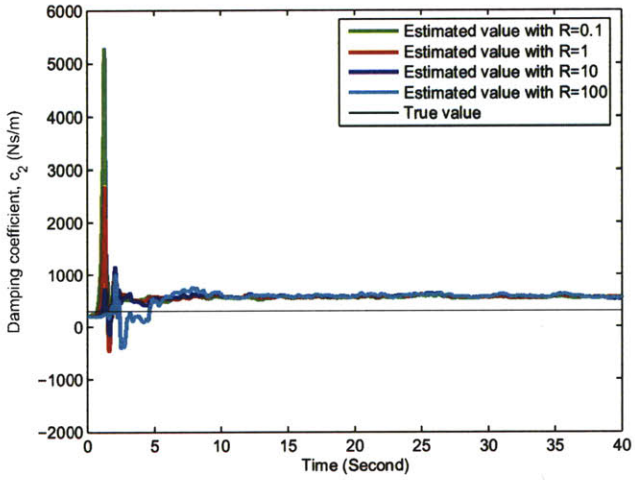

Figure 4-69: Comparison of estimated damping coefficient (c_2) with different levels of measurement noise covariance (R) of the linear 3DOF model (SNR=50).

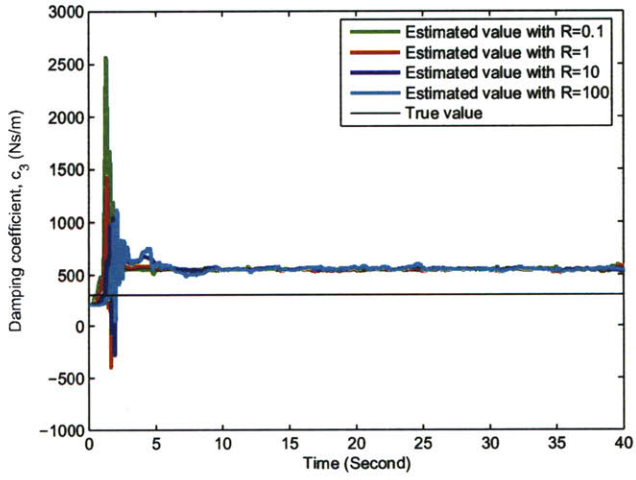

Figure 4-70: Comparison of estimated damping coefficient (c_3) with different levels of measurement noise covariance (R) of the linear 3DOF model (SNR=50).

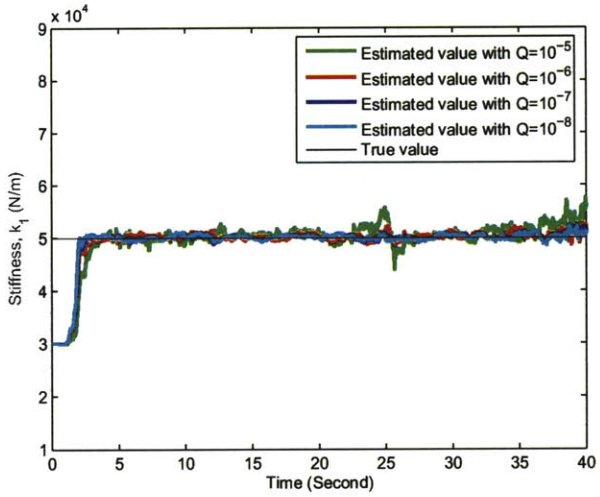

Figure 4-71: Comparison of estimated stiffness (k_1) with different levels of process noise covariance (Q) of the linear 3DOF model (SNR=20).

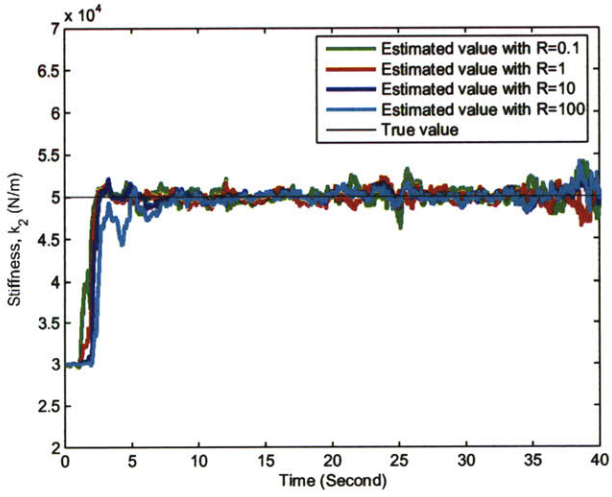

Figure 4-72: Comparison of estimated stiffness (k_2) with different levels of process noise covariance (Q) of the linear 3DOF model (SNR=20).

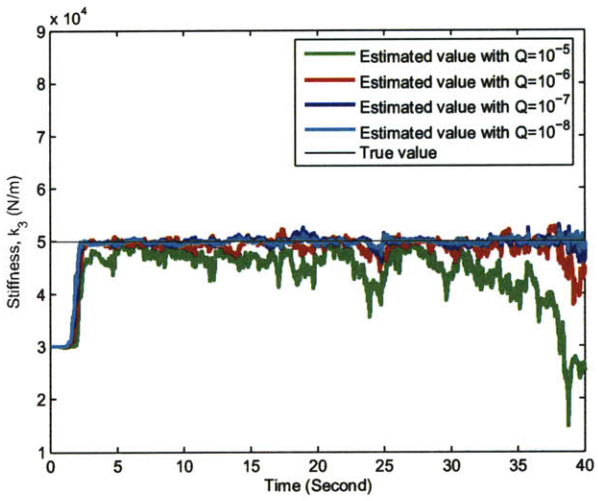

Figure 4-73: Comparison of estimated stiffness (k_3) with different levels of process noise covariance (Q) of the linear 3DOF model (SNR=20).

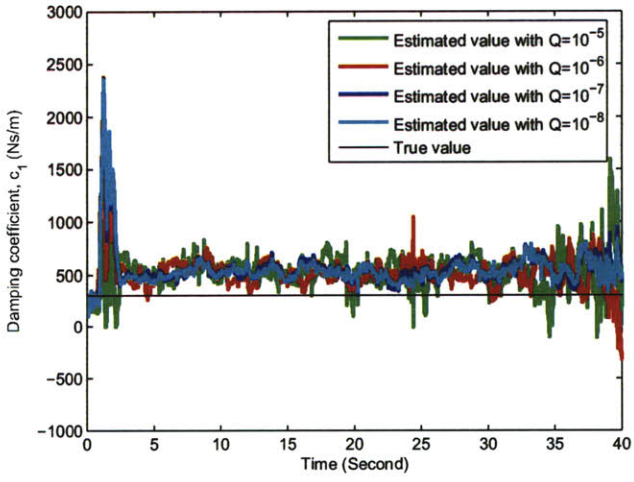

Figure 4-74: Comparison of estimated damping coefficient (c_1) with different levels of process noise covariance (Q) of the linear 3DOF model (SNR=20).

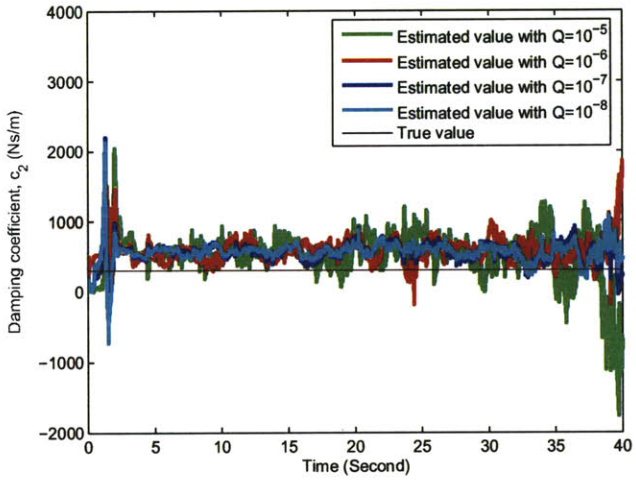

Figure 4-75: Comparison of estimated damping coefficient (c_2) with different levels of process noise covariance (Q) of the linear 3DOF model (SNR=20).

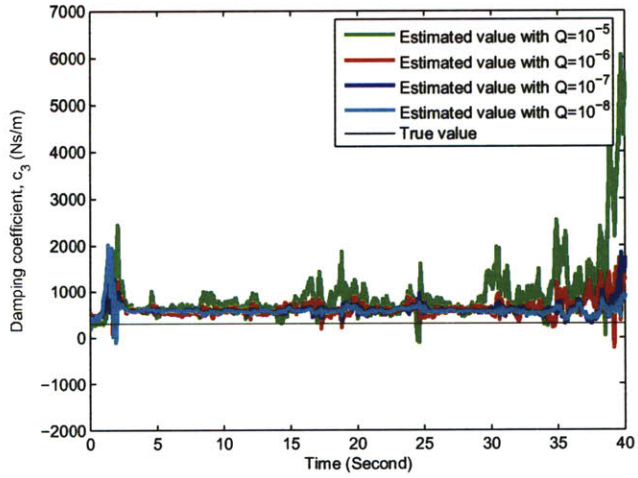

Figure 4-76: Comparison of estimated damping coefficient (c_3) with different levels of process noise covariance (Q) of the linear 3DOF model (SNR=20).

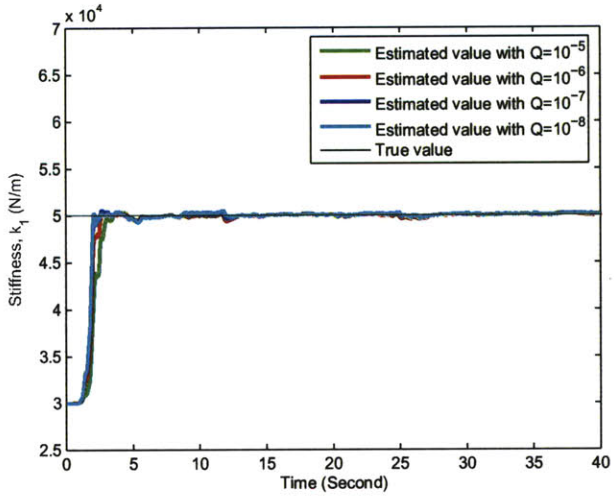

Figure 4-77: Comparison of estimated stiffness (k_1) with different levels of process noise covariance (Q) of the linear 3DOF model (SNR=50).

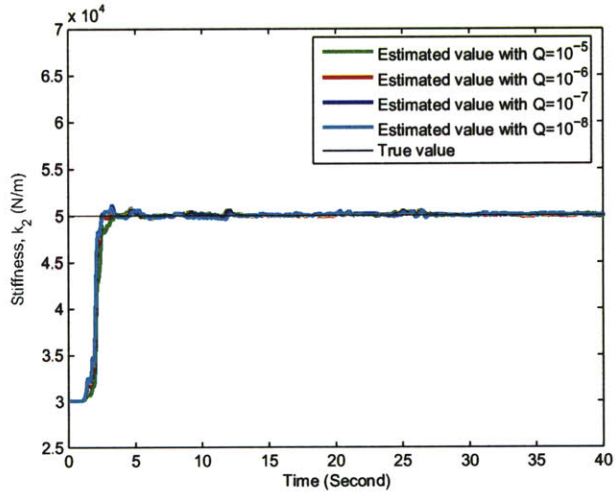

Figure 4-78: Comparison of estimated stiffness (k_2) with different levels of process noise covariance (Q) of the linear 3DOF model (SNR=50).

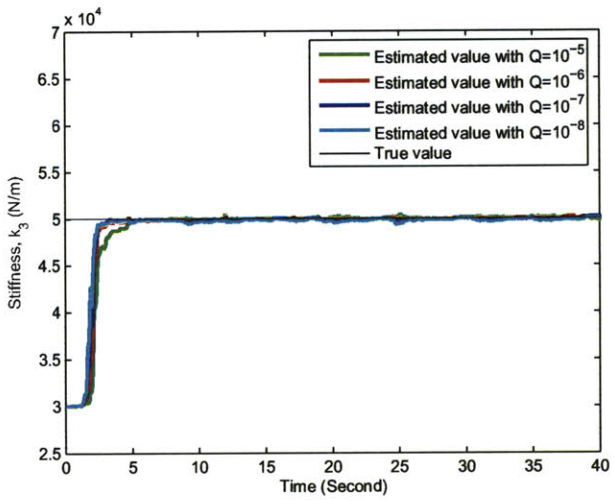

Figure 4-79: Comparison of estimated stiffness (k_3) with different levels of process noise covariance (Q) of the linear 3DOF model (SNR=50).

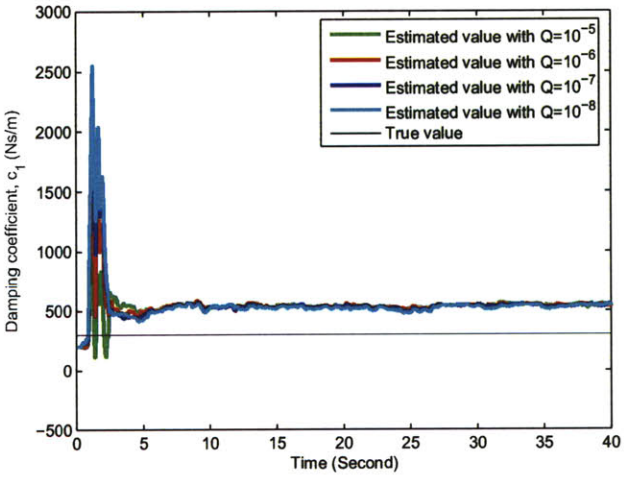

Figure 4-80: Comparison of estimated damping coefficient (c_1) with different levels of process noise covariance (Q) of the linear 3DOF model (SNR=50).

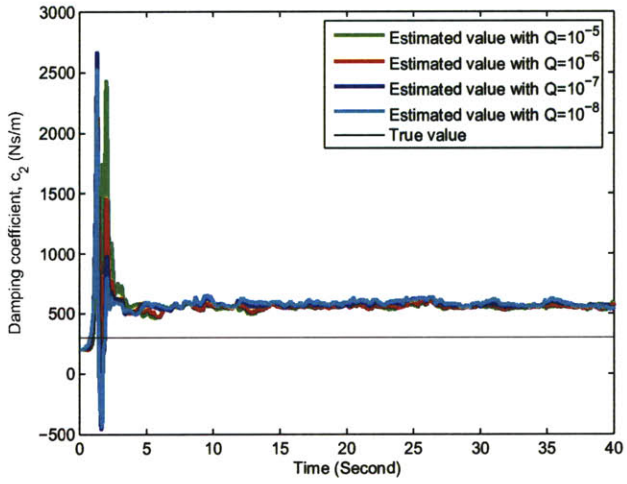

Figure 4-81: Comparison of estimated damping coefficient (c_2) with different levels of process noise covariance (Q) of the linear 3DOF model (SNR=50).

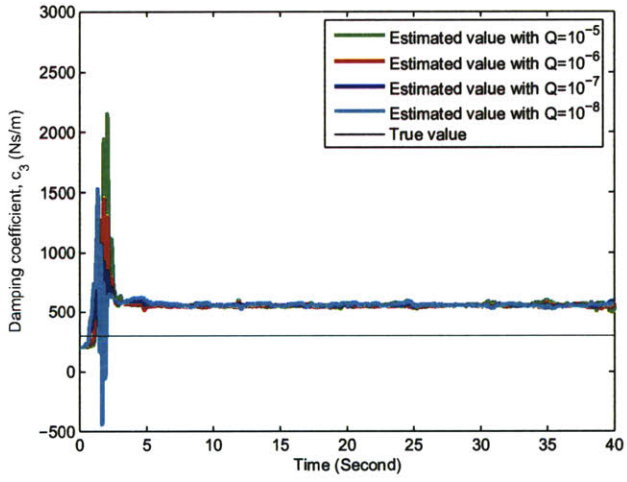

Figure 4-82: Comparison of estimated damping coefficient (c_3) with different levels of process noise covariance (Q) of the linear 3DOF model (SNR=50).

For simulating damage occurrence in a real structure, the stiffness in the first floor (k_1) and in the third floor (k_3) are designed to be dropped from 50 kN/m to 40 kN/m in our model. Other initial selections and settings are same as those in the non-dropped case.

Figure 4-83 through 4-88 illustrates the estimated results of different external noise levels. It was found that models with lower noise generate accurate estimations. One thing deserved to be mentioned is that there exists a little jump at around 20 second for estimated k_2, c_1, c_2, c_3, which means the unchanged parameters reveal that other parameters are altered in the system.

Figure 4-89 through 4-94 exhibits the effects of different levels of measurement noise covariance on the simulation results with fixed process noise covariance $Q = 10^{-7}\mathbf{I}_{12}$ for the model with noise of SNR=20. Figure 4-95 through 4-100 shows the effects for the case of SNR=50. As expected, a larger R produces better estimations for the case of SNR=20, and there is no conspicuous difference for the case of SNR=50.

Likewise, the influences of process noise covariance were evaluated with fixed measurement noise covariance $R = 1\mathbf{I}_3$, and the results are shown in Figure 4-101 to 4-112. Figure 4-101 to 4-106 is for the case of model with noise of SNR=20, and Figure 4-107 to 4-112 is for the case of model with SNR=50. The results show that a smaller Q provides a more stable parametric estimation for the case of SNR=20. As for the case of SNR=50, the estimated parameters are rarely distinct.

To sum up, process noise covariance being 10^{-8} and measurement noise covariance being 100 are the preferred choice for both constant and time-varying stiffness cases. Although R=100 converges slower than other values, overall, it results in better estimations.

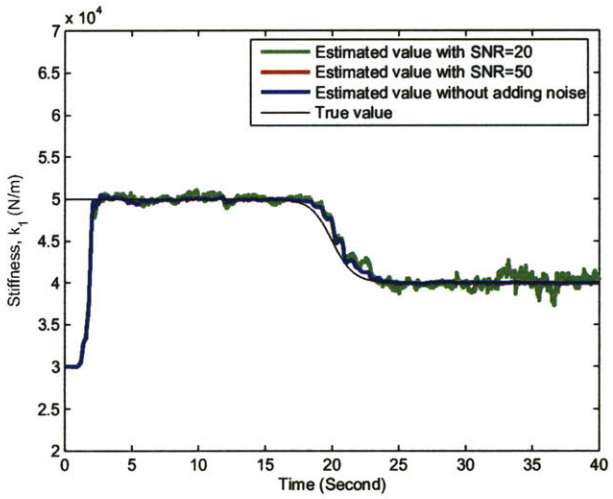

Figure 4-83: Comparison of estimated stiffness (k_1) with different levels of noise for the case of stiffness dropping of the linear 3DOF model.

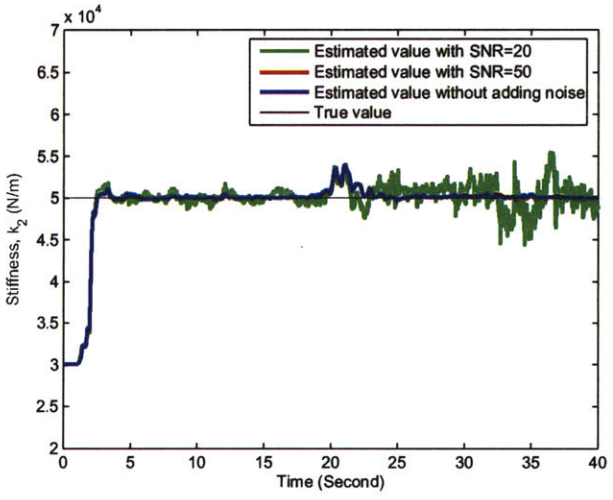

Figure 4-84: Comparison of estimated stiffness (k_2) with different levels of noise for the case of stiffness dropping of the linear 3DOF model.

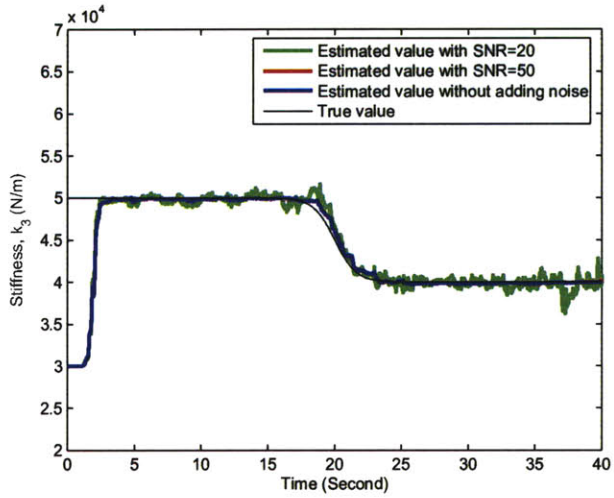

Figure 4-85: Comparison of estimated stiffness (k_3) with different levels of noise for the case of stiffness dropping of the linear 3DOF model.

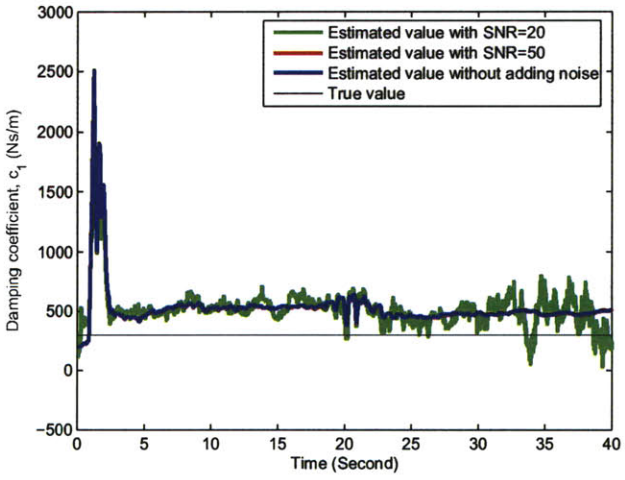

Figure 4-86: Comparison of estimated damping coefficient (c_1) with different levels of noise for the case of stiffness dropping of the linear 3DOF model.

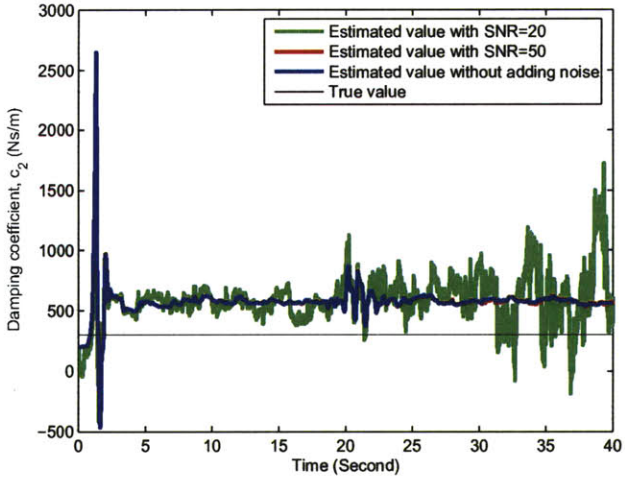

Figure 4-87: Comparison of estimated damping coefficient (c_2) with different levels of noise for the case of stiffness dropping of the linear 3DOF model.

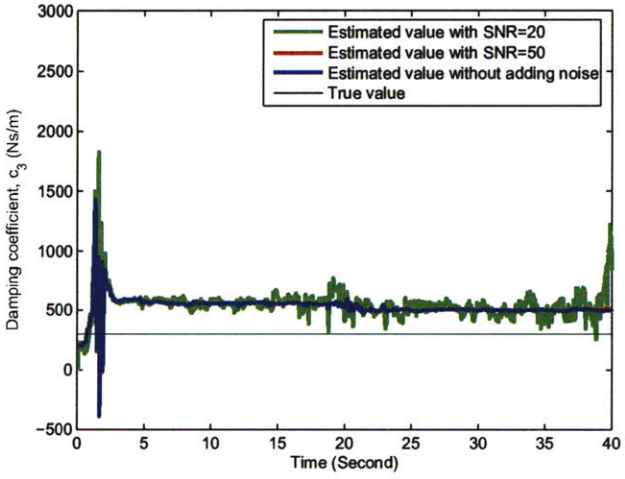

Figure 4-88: Comparison of estimated damping coefficient (c_3) with different levels of noise for the case of stiffness dropping of the linear 3DOF model.

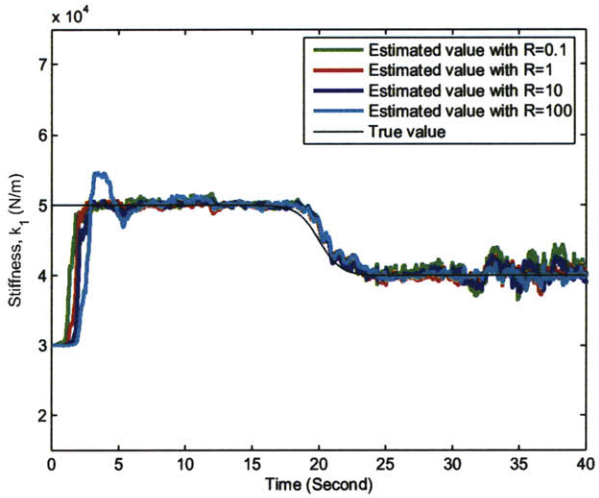

Figure 4-89: Comparison of estimated stiffness (k_1) with different levels of measurement noise covariance (R) for the case of stiffness dropping of the linear 3DOF model (SNR=20).

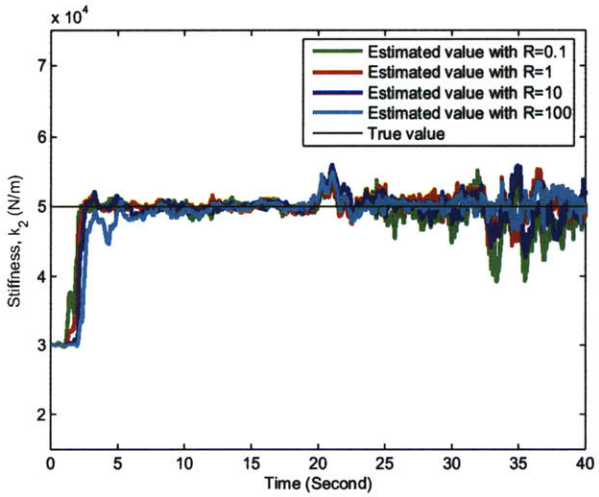

Figure 4-90: Comparison of estimated stiffness (k_2) with different levels of measurement noise covariance (R) for the case of stiffness dropping of the linear 3DOF model (SNR=20).

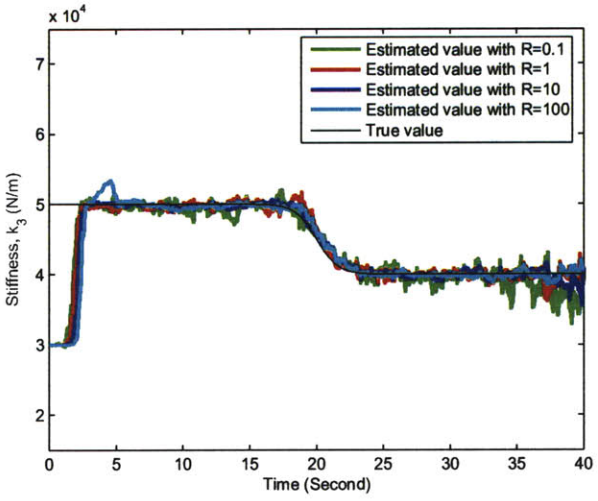

Figure 4-91: Comparison of estimated stiffness (k_3) with different levels of measurement noise covariance (R) for the case of stiffness dropping of the linear 3DOF model (SNR=20).

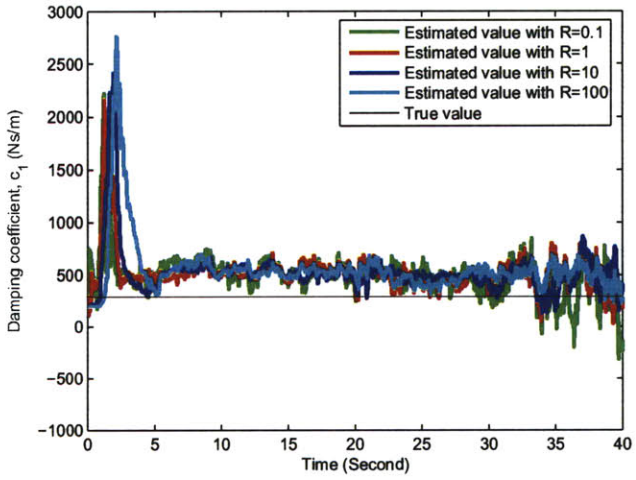

Figure 4-92: Comparison of estimated damping coefficient (c_1) with different levels of measurement noise covariance (R) for the case of stiffness dropping of the linear 3DOF model (SNR=20).

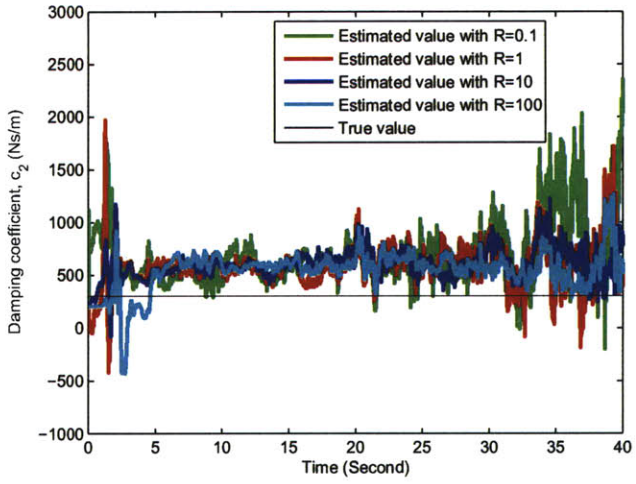

Figure 4-93: Comparison of estimated damping coefficient (c_2) with different levels of measurement noise covariance (R) for the case of stiffness dropping of the linear 3DOF model (SNR=20).

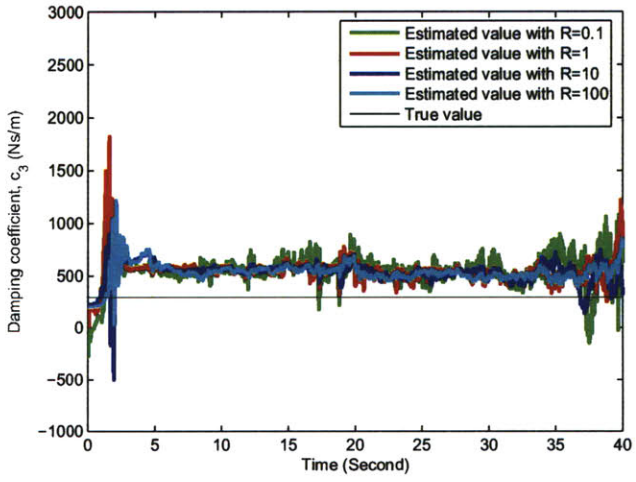

Figure 4-94: Comparison of estimated damping coefficient (c_3) with different levels of measurement noise covariance (R) for the case of stiffness dropping of the linear 3DOF model (SNR=20).

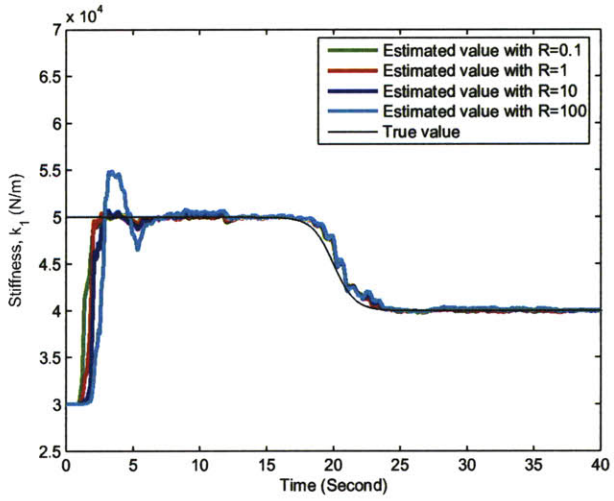

Figure 4-95: Comparison of estimated stiffness (k_1) with different levels of measurement noise covariance (R) for the case of stiffness dropping of the linear 3DOF model (SNR=50).

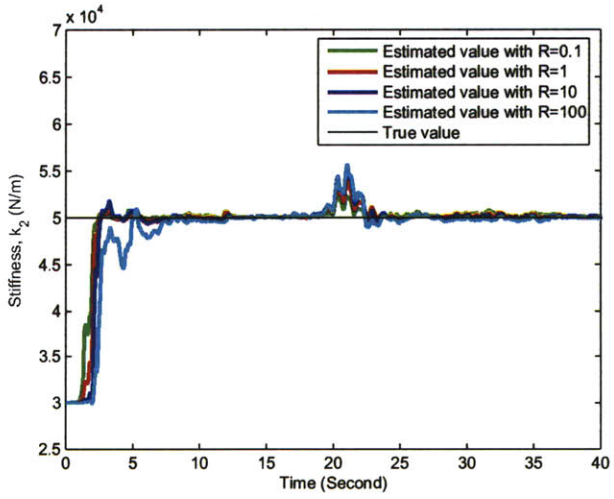

Figure 4-96: Comparison of estimated stiffness (k_2) with different levels of measurement noise covariance (R) for the case of stiffness dropping of the linear 3DOF model (SNR=50).

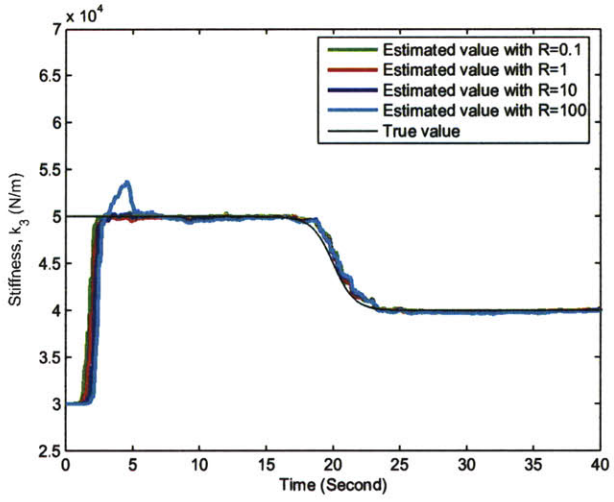

Figure 4-97: Comparison of estimated stiffness (k_3) with different levels of measurement noise covariance (R) for the case of stiffness dropping of the linear 3DOF model (SNR=50).

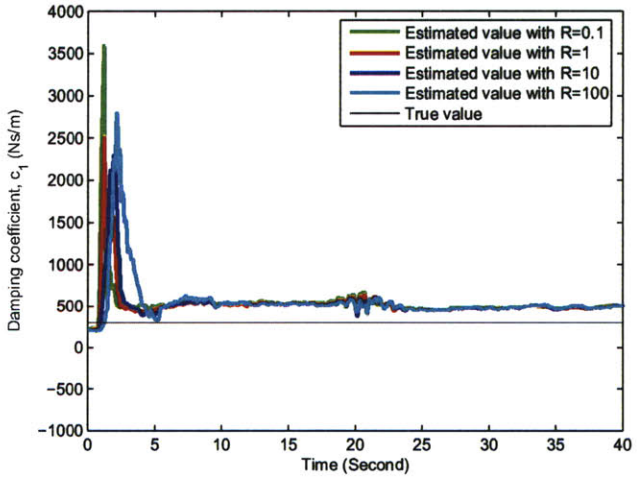

Figure 4-98: Comparison of estimated damping coefficient (c_1) with different levels of measurement noise covariance (R) for the case of stiffness dropping of the linear 3DOF model (SNR=50).

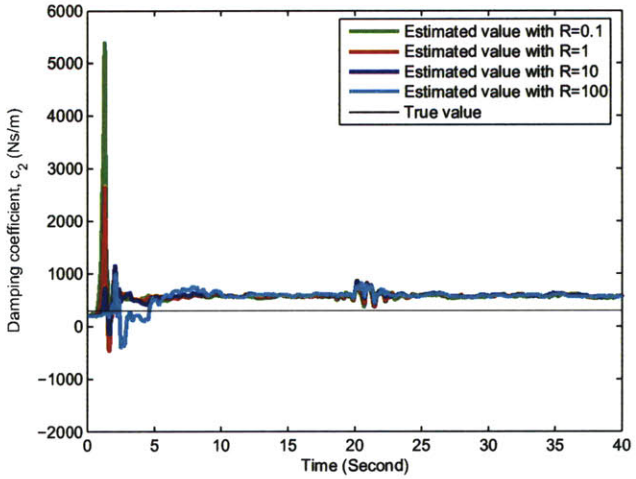

Figure 4-99: Comparison of estimated damping coefficient (c_2) with different levels of measurement noise covariance (R) for the case of stiffness dropping of the linear 3DOF model (SNR=50).

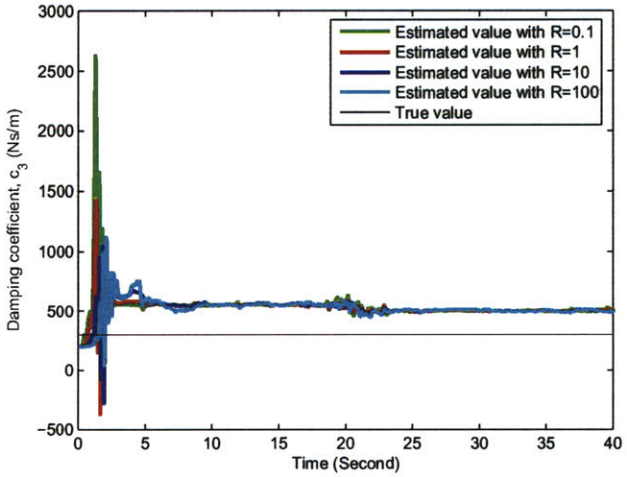

Figure 4-100: Comparison of estimated damping coefficient (c_3) with different levels of measurement noise covariance (R) for the case of stiffness dropping of the linear 3DOF model (SNR=50).

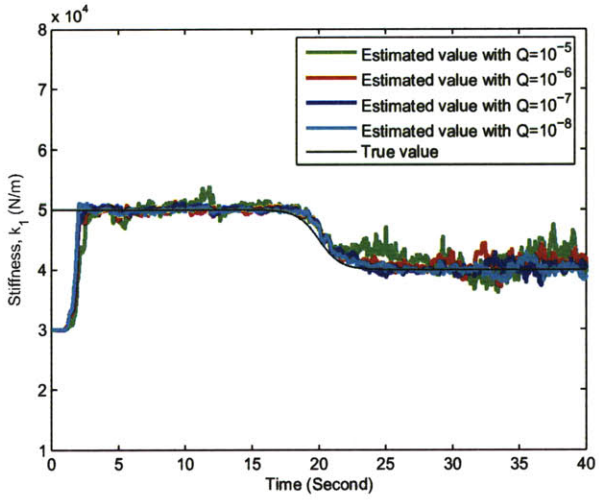

Figure 4-101: Comparison of estimated stiffness (k_1) with different levels of process noise covariance (Q) for the case of stiffness dropping of the linear 3DOF model (SNR=20).

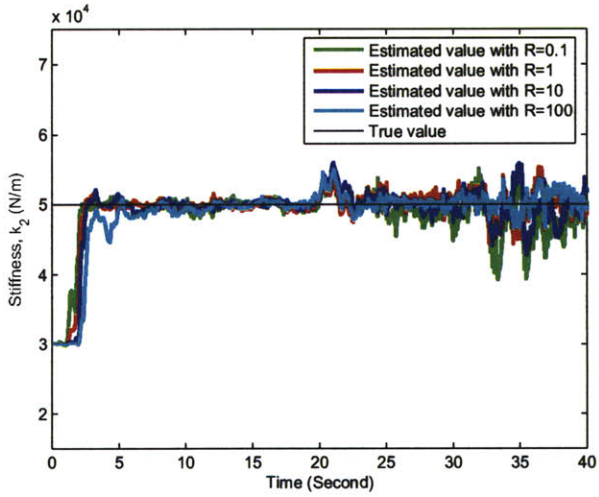

Figure 4-102: Comparison of estimated stiffness (k_2) with different levels of process noise covariance (Q) for the case of stiffness dropping of the linear 3DOF model (SNR=20).

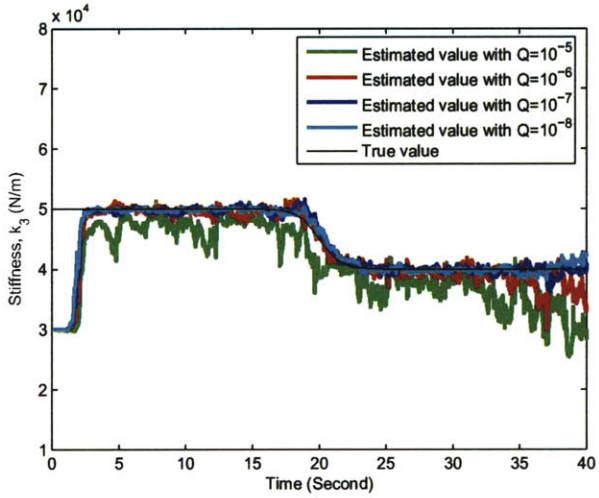

Figure 4-103: Comparison of estimated stiffness (k_3) with different levels of process noise covariance (Q) for the case of stiffness dropping of the linear 3DOF model (SNR=20).

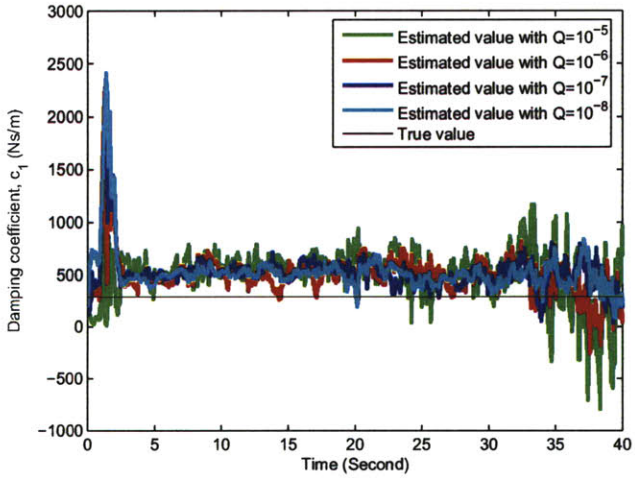

Figure 4-104: Comparison of estimated damping coefficient (c_1) with different levels of process noise covariance (Q) for the case of stiffness dropping of the linear 3DOF model (SNR=20).

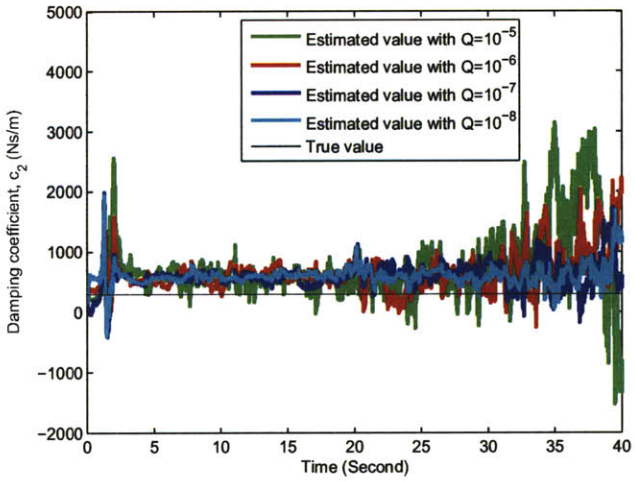

Figure 4-105: Comparison of estimated damping coefficient (c_2) with different levels of process noise covariance (Q) for the case of stiffness dropping of the linear 3DOF model (SNR=20).

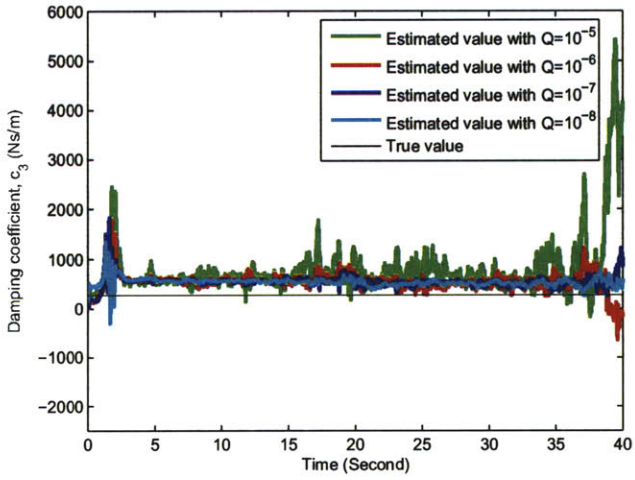

Figure 4-106: Comparison of estimated damping coefficient (c_3) with different levels of process noise covariance (Q) for the case of stiffness dropping of the linear 3DOF model (SNR=20).

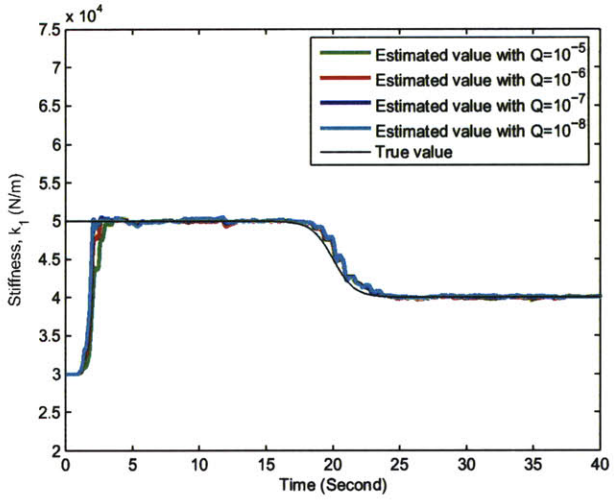

Figure 4-107: Comparison of estimated stiffness (k_1) with different levels of process noise covariance (Q) for the case of stiffness dropping of the linear 3DOF model (SNR=50).

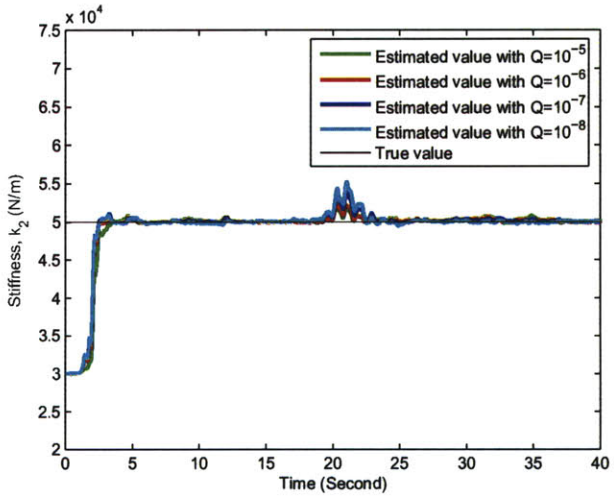

Figure 4-108: Comparison of estimated stiffness (k_2) with different levels of process noise covariance (Q) for the case of stiffness dropping of the linear 3DOF model (SNR=50).

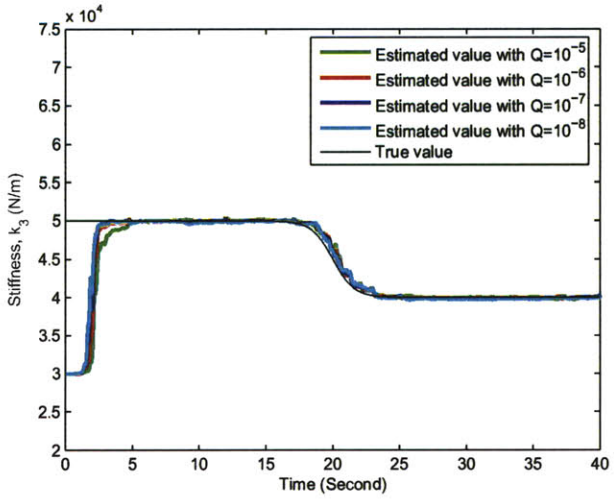

Figure 4-109: Comparison of estimated stiffness (k_3) with different levels of process noise covariance (Q) for the case of stiffness dropping of the linear 3DOF model (SNR=50).

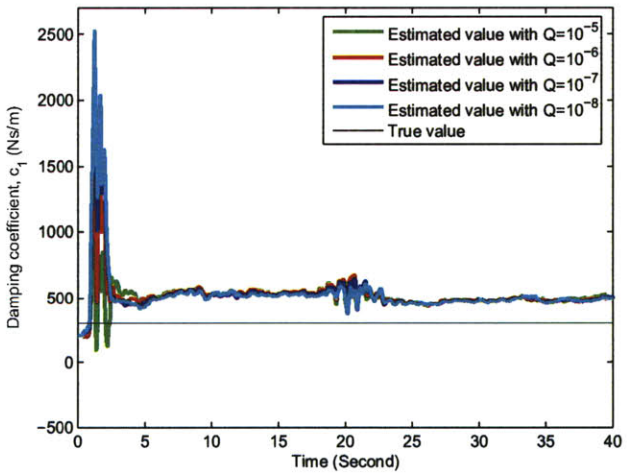

Figure 4-110: Comparison of estimated damping coefficient (c_1) with different levels of process noise covariance (Q) for the case of stiffness dropping of the linear 3DOF model (SNR=50).

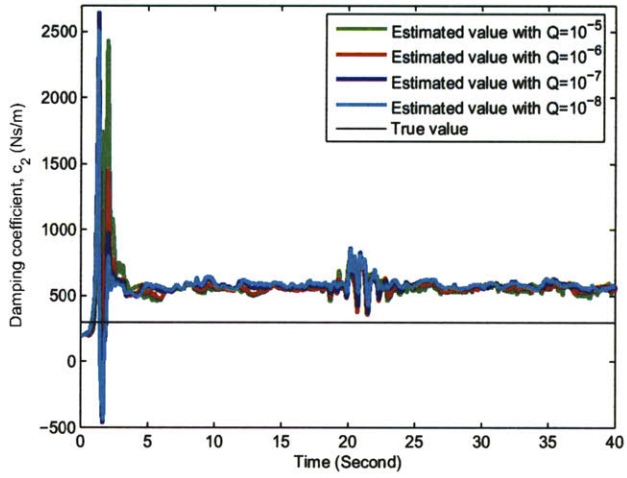

Figure 4-111: Comparison of estimated damping coefficient (c_2) with different levels of process noise covariance (Q) for the case of stiffness dropping of the linear 3DOF model (SNR=50).

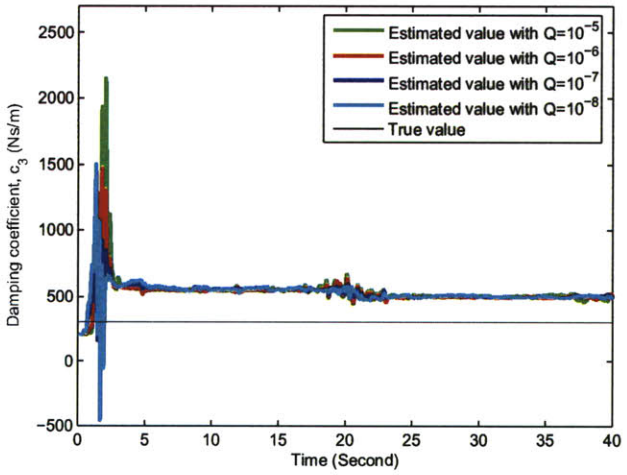

Figure 4-112: Comparison of estimated damping coefficient (c_3) with different levels of process noise covariance (Q) for the case of stiffness dropping of the linear 3DOF model (SNR=50).

4.2.2 Nonlinear Elastic Structure

In this section, a 2DOF nonlinear elastic structure is considered, and the adaptive Kalman filter was implemented to estimate stiffness and damping coefficient. The designed nonlinear model subjected to an earthquake excitation can be described in state space representation as

$$\begin{bmatrix} m & 0 \\ 0 & m \end{bmatrix} \begin{bmatrix} \ddot{x}_1 \\ \ddot{x}_2 \end{bmatrix} + \begin{bmatrix} c_1 + c_2 & -c_2 \\ -c_2 & c_2 \end{bmatrix} \begin{bmatrix} \dot{x}_1 \\ \dot{x}_2 \end{bmatrix} + \begin{bmatrix} k_{11} + k_{21} & -k_{21} \\ -k_{21} & k_{21} \end{bmatrix} \begin{bmatrix} x_1 \\ x_2 \end{bmatrix} + \begin{bmatrix} k_{12} & -k_{22} \\ 0 & k_{22} \end{bmatrix} \begin{bmatrix} x_1^2 \\ (x_2 - x_1)^2 \end{bmatrix} = - \begin{bmatrix} m \\ m \end{bmatrix} a_g \tag{4.16}$$

where k_{11} and k_{21} represent the stiffness for the first floor and the second floor; k_{12} and k_{22} are the stiffness in the first floor and the second floor related to nonlinear terms; c_1 and c_2 are the damping coefficient for the first floor and the second floor. The state vector and measured output are defined as

$$X = \begin{bmatrix} x_1 \\ x_2 \\ \dot{x}_1 \\ \dot{x}_2 \\ k_{11} \\ k_{12} \\ k_{21} \\ k_{22} \\ c_1 \\ c_2 \end{bmatrix} = \begin{bmatrix} x_1 \\ x_2 \\ x_3 \\ x_4 \\ x_5 \\ x_6 \\ x_7 \\ x_8 \\ x_9 \\ x_{10} \end{bmatrix} \tag{4.17}$$

$$\dot{X} - w(t) = \begin{bmatrix} \dot{x}_1 \\ \dot{x}_2 \\ \ddot{x}_1 \\ \\ \ddot{x}_2 \\ \\ \dot{k}_{11} \\ \dot{k}_{12} \\ \dot{k}_{21} \\ \dot{k}_{22} \\ \dot{c}_1 \\ \dot{c}_2 \end{bmatrix} = \begin{bmatrix} x_3 \\ x_4 \\ -a_g - [x_9 x_3 - x_{10}(x_4 - x_3) + x_5 x_1 + x_6 x_1^2 \\ -x_7(x_2 - x_1) - x_8(x_2 - x_1)^2]/m \\ -a_g - [x_{10}(x_4 - x_3) + x_7(x_2 - x_1) \\ +x_8(x_2 - x_1)^2]/m \\ 0 \\ 0 \\ 0 \\ 0 \\ 0 \\ 0 \end{bmatrix} \tag{4.18}$$

$$Y - v(t) = \begin{bmatrix} \ddot{x}_1 + a_g \\ \\ \ddot{x}_2 + a_g \\ \\ \end{bmatrix} = \begin{bmatrix} -[x_9 x_3 - x_{10}(x_4 - x_3) + x_5 x_1 + x_6 x_1^2 \\ -x_7(x_2 - x_1) - x_8(x_2 - x_1)^2]/m \\ -[x_{10}(x_4 - x_3) + x_7(x_2 - x_1) \\ +x_8(x_2 - x_1)^2]/m \end{bmatrix} \tag{4.19}$$

Note that k and c are the parameters desired to be estimated. The structural properties, the initial estimations of the state parameters, and the noise covariances are stated in Table 4.10,4.11, and 4.12, respectively. The initial selection of the error covariance in this model is $P_{0|0} = diag[1, 1, 1, 1, 10^{-7}, 10^{-7}, 10^{-7}, 10^{-7}, 10^{-7}, 10^{-7}]$.

Table 4.10: Structural properties of the nonlinear 2DOF model.

Structural Properties	Magnitudes	Units
m	1000	kg
$k_{11} = k_{12}$	100000	N/m
k_{21}	60000	N/m
k_{22}	50000	N/m
$c_1 = c_2 = c_3$	1000	Ns/m

Table 4.11: Initial estimations for state parameters of the nonlinear 2DOF model.

State parameters	Magnitudes	Units
$x_1 = x_2$	0	m
$\dot{x}_1 = \dot{x}_2$	0	m/s
$k_{11} = k_{12}$	50000	N/m
k_{21}	20000	kN/m
k_{22}	20000	kN/m
$c_1 = c_2$	500	Ns/m

Table 4.12: Noise covariances of the nonlinear 2DOF model.

Noise covariances	Magnitudes
Measurement	$1\mathbf{I}_2$
Process	$10^{-7}\mathbf{I}_{10}$

Figure 4-113 to 4-118 shows the estimated stiffness and damping coefficient under different levels of noise. It was observed that the adaptive extended Kalman filter generates much more stable estimations for the case with low noise than it with high noise, especially for estimating nonlinear terms k_{12} and k_{22}.

Figure 4-119 through 4-124 shows the influences of different levels of measurement noise covariance with fixed process noise covariance $Q = 10^{-7}\mathbf{I}_{10}$ for the system with noise of SNR=20. The estimated parameters reveal that a larger value of measurement noise covariance produces better estimations. Figure 4-125 through 4-130 illustrates the results for the case of SNR=50. The results show that the proposed filter works better for low noise-added case and R is less sensitive compared with the case of SNR=20.

Figure 4-131 through 4-136 shows the influences of different levels of process noise covariance on estimations with fixed measurement noise covariance $R = 1\mathbf{I}_2$ for the model with noise of SNR=20. Figure 4-137 through 4-142 illustrates the results for the case of model with SNR=50 noise. As shown in the figures, a smaller selection of process noise covariance results in better estimations for the case of model with SNR=20 noise. As for the model with SNR=50 noise, Q has no influence on the estimated parameters.

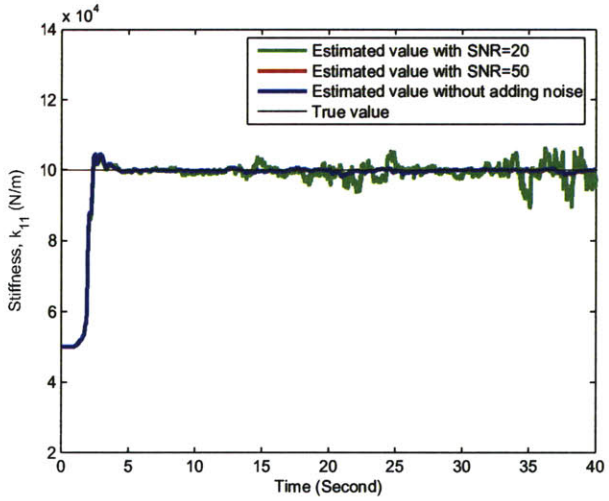

Figure 4-113: Comparison of estimated stiffness (k_{11}) of the nonlinear 2DOF model with different levels of noise.

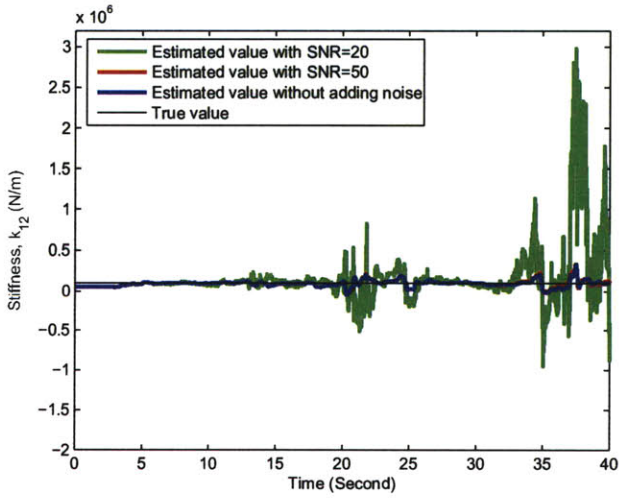

Figure 4-114: Comparison of estimated stiffness (k_{12}) of the nonlinear 2DOF model with different levels of noise.

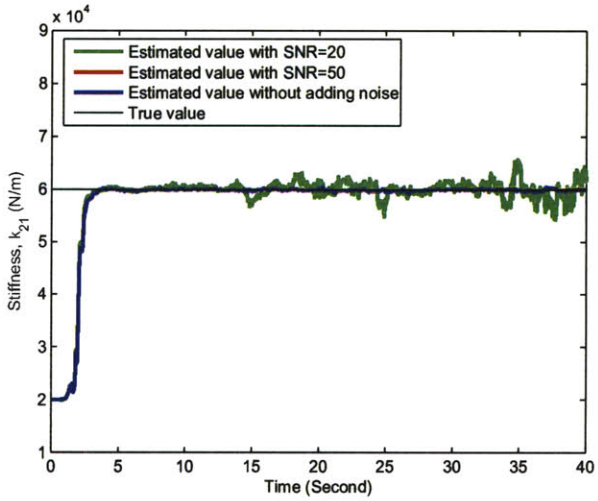

Figure 4-115: Comparison of estimated stiffness (k_{21}) of the nonlinear 2DOF model with different levels of noise.

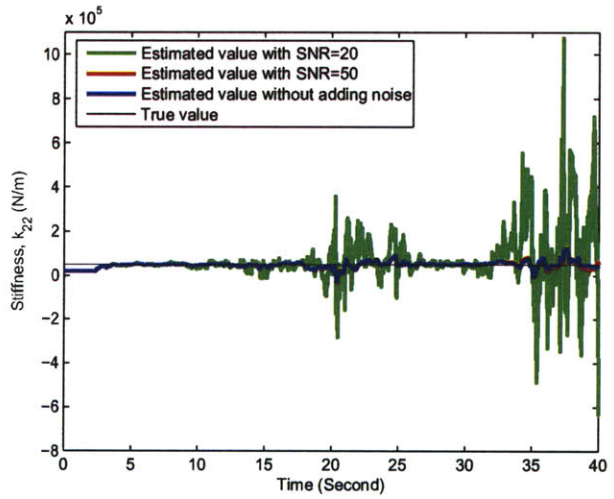

Figure 4-116: Comparison of estimated stiffness (k_{22}) of the nonlinear 2DOF model with different levels of noise.

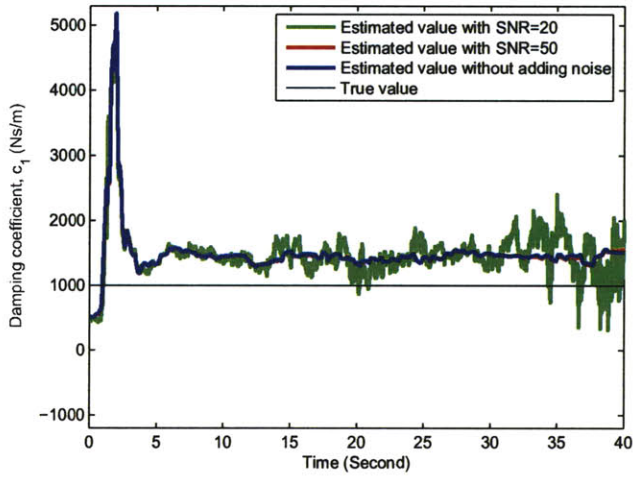

Figure 4-117: Comparison of estimated damping coefficient (c_1) of the nonlinear 2DOF model with different levels of noise.

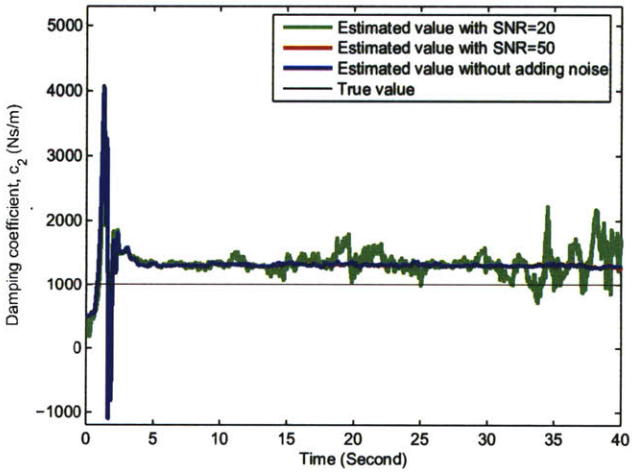

Figure 4-118: Comparison of estimated damping coefficient (c_2) of the nonlinear 2DOF model with different levels of noise.

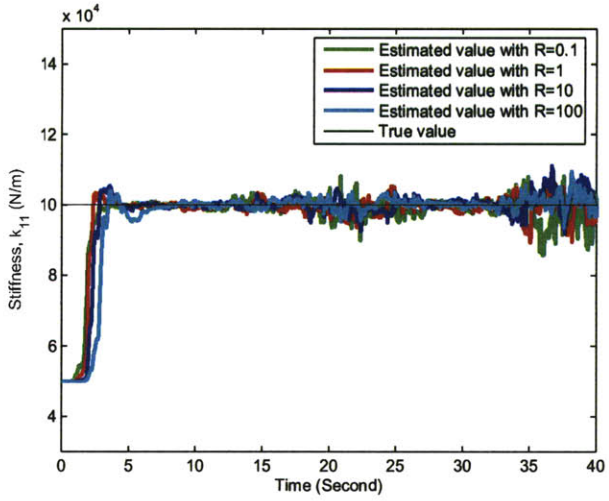

Figure 4-119: Comparison of estimated stiffness (k_{11}) with different levels of measurement noise covariance (R) of the nonlinear 2DOF model (SNR=20).

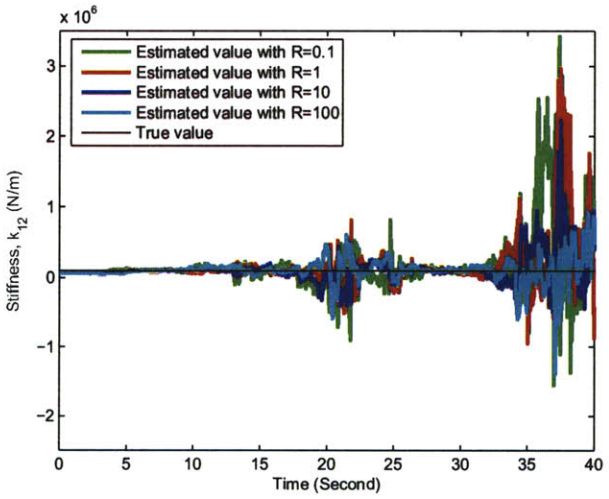

Figure 4-120: Comparison of estimated stiffness (k_{12}) with different levels of measurement noise covariance (R) of the nonlinear 2DOF model (SNR=20).

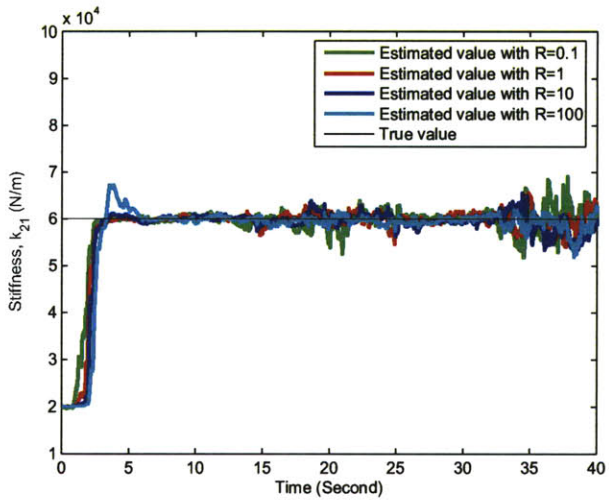

Figure 4-121: Comparison of estimated stiffness (k_{21}) with different levels of measurement noise covariance (R) of the nonlinear 2DOF model (SNR=20).

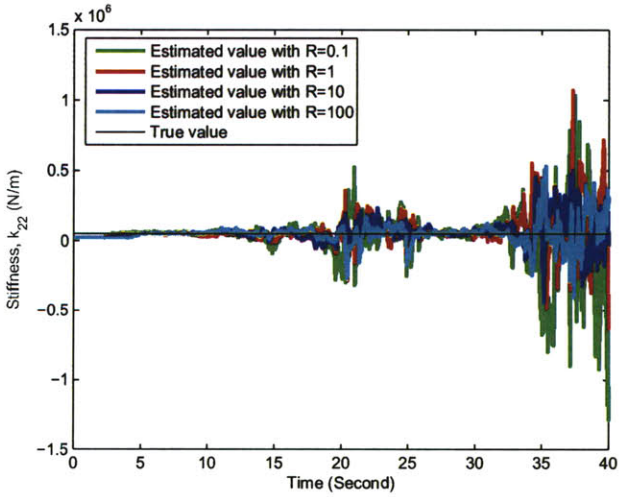

Figure 4-122: Comparison of estimated stiffness (k_{22}) with different levels of measurement noise covariance (R) of the nonlinear 2DOF model (SNR=20).

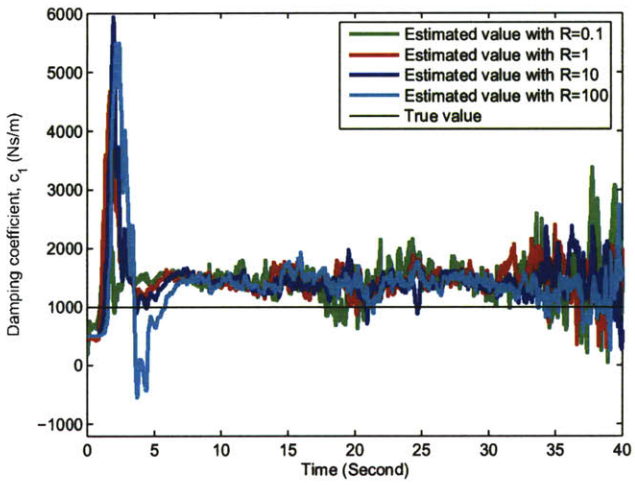

Figure 4-123: Comparison of estimated damping coefficient (c_1) with different levels of measurement noise covariance (R) of the nonlinear 2DOF model (SNR=20).

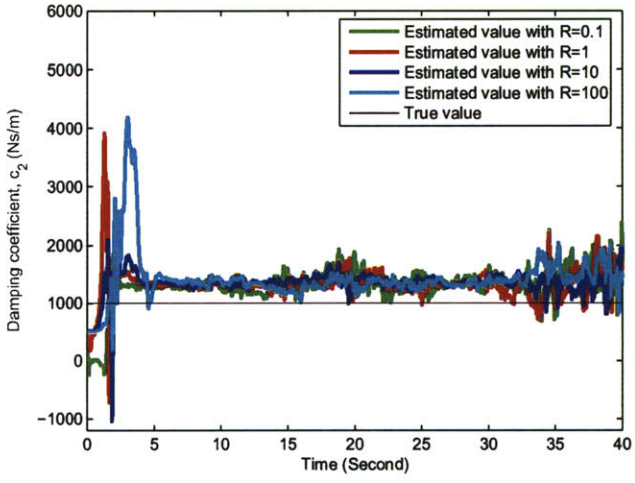

Figure 4-124: Comparison of estimated damping coefficient (c_2) with different levels of measurement noise covariance (R) of the nonlinear 2DOF model (SNR=20).

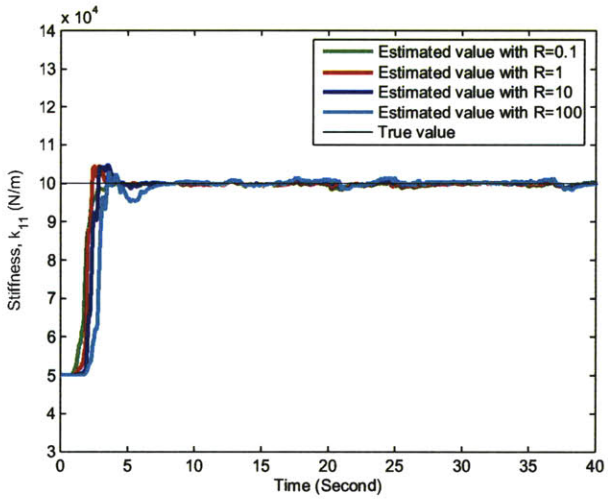

Figure 4-125: Comparison of estimated stiffness (k_{11}) with different levels of measurement noise covariance (R) of the nonlinear 2DOF model (SNR=50).

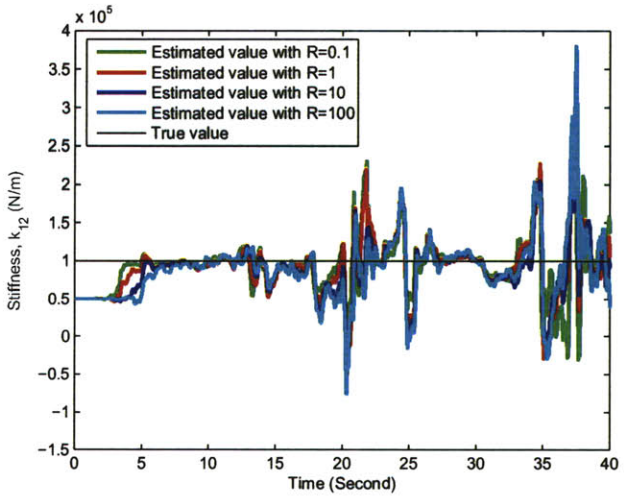

Figure 4-126: Comparison of estimated stiffness (k_{12}) with different levels of measurement noise covariance (R) of the nonlinear 2DOF model (SNR=50).

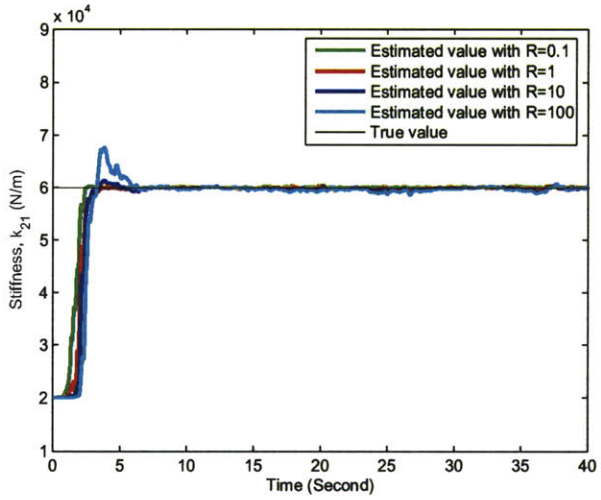

Figure 4-127: Comparison of estimated stiffness (k_{21}) with different levels of measurement noise covariance (R) of the nonlinear 2DOF model (SNR=50).

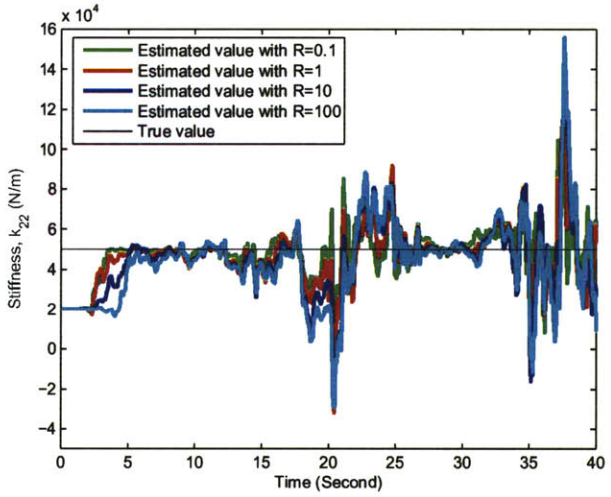

Figure 4-128: Comparison of estimated stiffness (k_{22}) with different levels of measurement noise covariance (R) of the nonlinear 2DOF model (SNR=50).

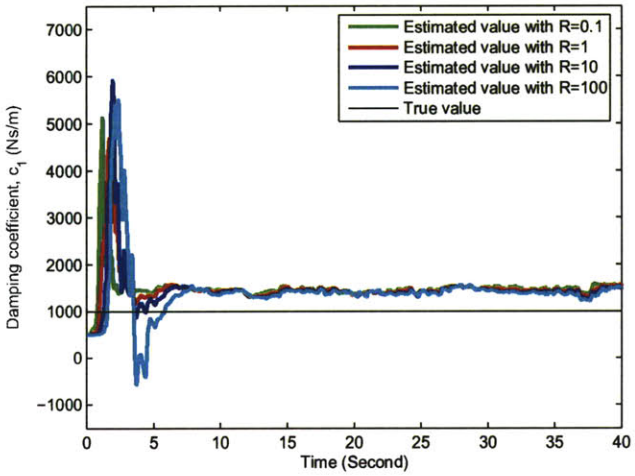

Figure 4-129: Comparison of estimated damping coefficient (c_1) with different levels of measurement noise covariance (R) of the nonlinear 2DOF model (SNR=50).

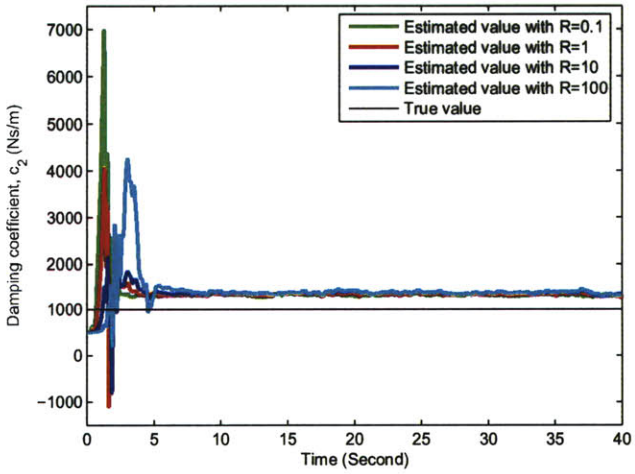

Figure 4-130: Comparison of estimated damping coefficient (c_2) with different levels of measurement noise covariance (R) of the nonlinear 2DOF model (SNR=50).

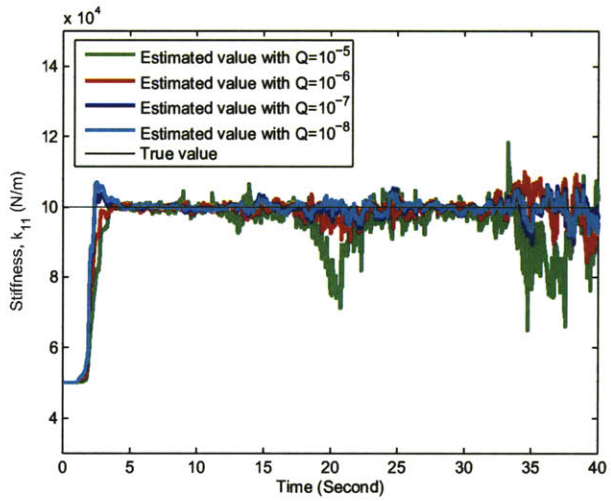

Figure 4-131: Comparison of estimated stiffness (k_{11}) with different levels of process noise covariance (Q) of the nonlinear 2DOF model (SNR=20).

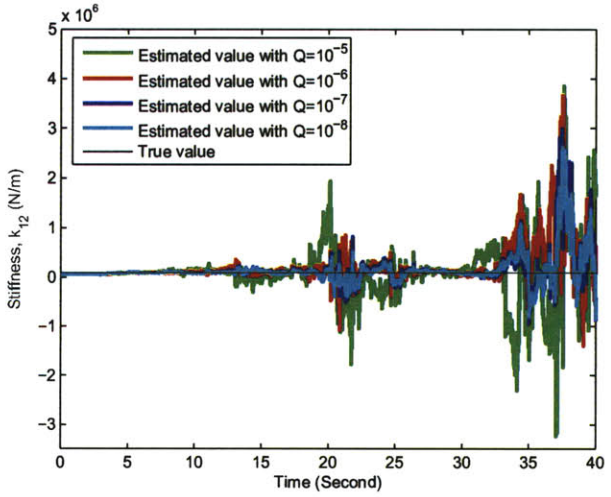

Figure 4-132: Comparison of estimated stiffness (k_{12}) with different levels of process noise covariance (Q) of the nonlinear 2DOF model (SNR=20).

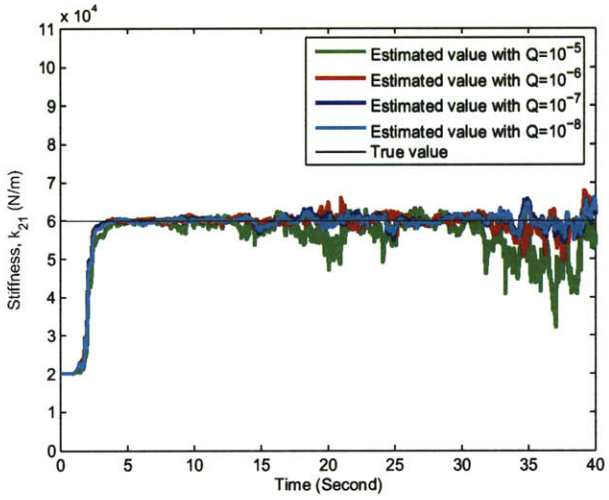

Figure 4-133: Comparison of estimated stiffness (k_{21}) with different levels of process noise covariance (Q) of the nonlinear 2DOF model (SNR=20).

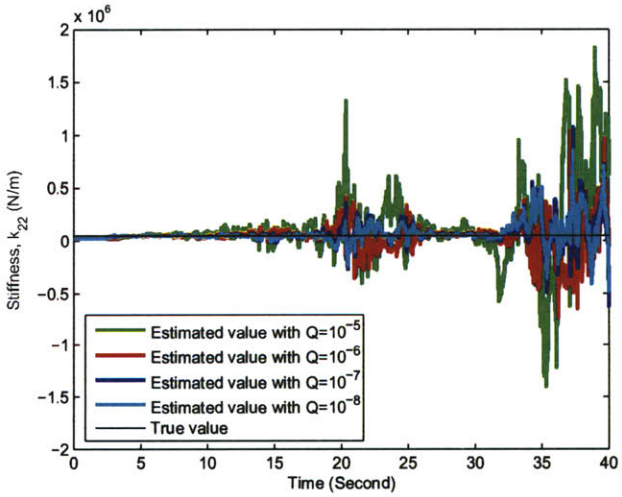

Figure 4-134: Comparison of estimated stiffness (k_{22}) with different levels of process noise covariance (Q) of the nonlinear 2DOF model (SNR=20).

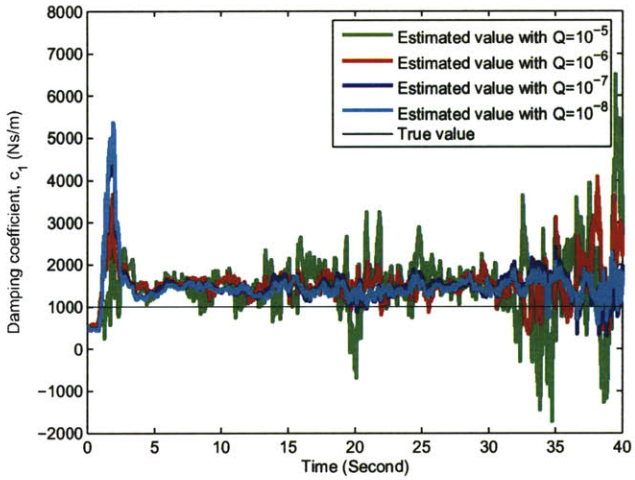

Figure 4-135: Comparison of estimated damping coefficient (c_1) with different levels of process noise covariance (Q) of the nonlinear 2DOF model (SNR=20).

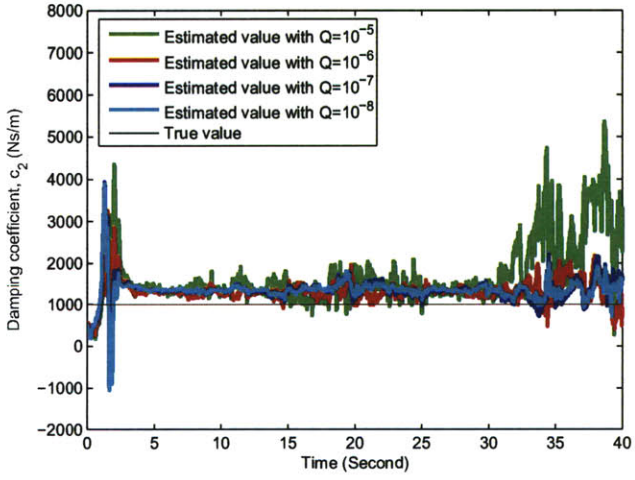

Figure 4-136: Comparison of estimated damping coefficient (c_2) with different levels of process noise covariance (Q) of the nonlinear 2DOF model (SNR=20).

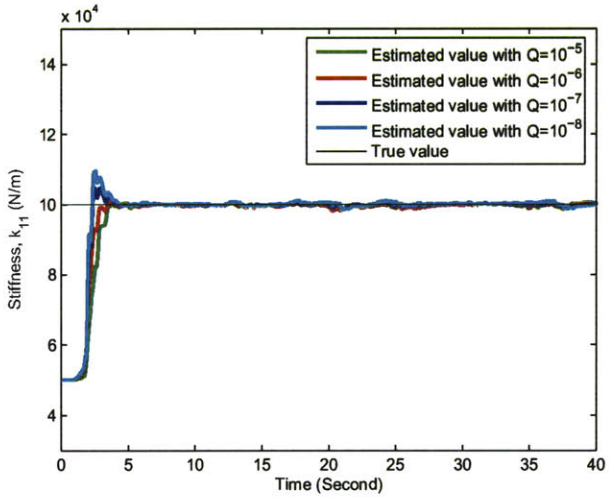

Figure 4-137: Comparison of estimated stiffness (k_{11}) with different levels of process noise covariance (Q) of the nonlinear 2DOF model (SNR=50).

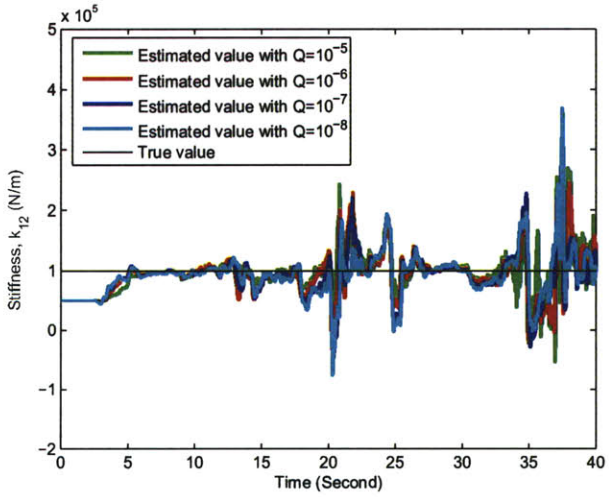

Figure 4-138: Comparison of estimated stiffness (k_{12}) with different levels of process noise covariance (Q) of the nonlinear 2DOF model (SNR=50).

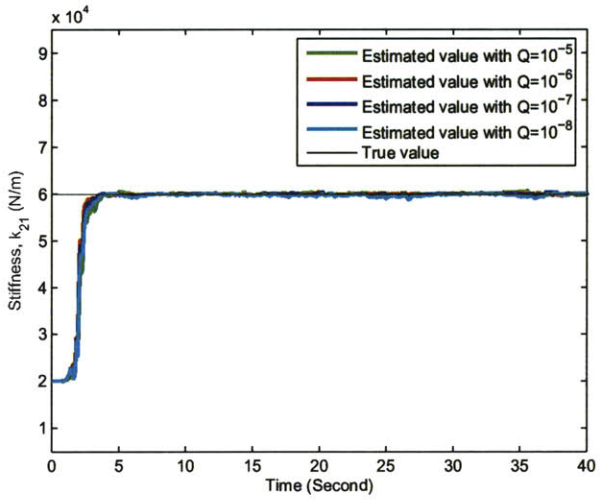

Figure 4-139: Comparison of estimated stiffness (k_{21}) with different levels of process noise covariance (Q) of the nonlinear 2DOF model (SNR=50).

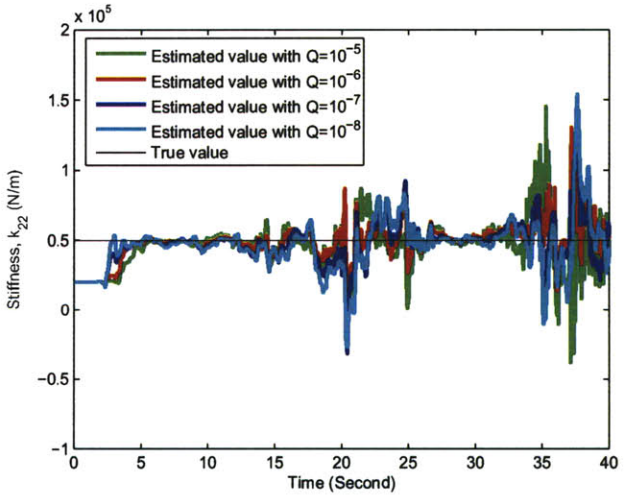

Figure 4-140: Comparison of estimated stiffness (k_{22}) with different levels of process noise covariance (Q) of the nonlinear 2DOF model (SNR=50).

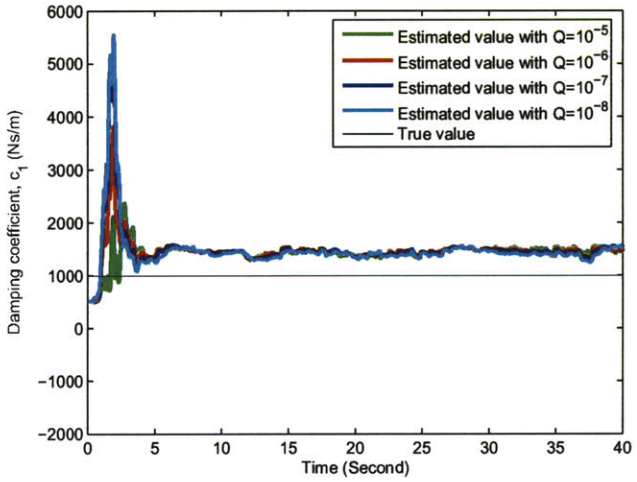

Figure 4-141: Comparison of estimated damping coefficient (c_1) with different levels of process noise covariance (Q) of the nonlinear 2DOF model (SNR=50).

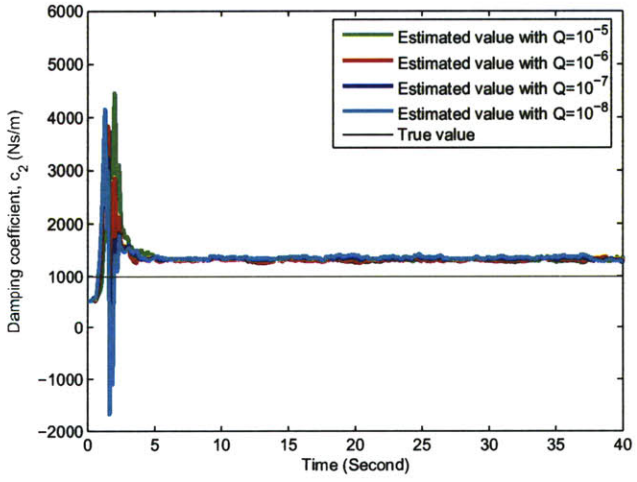

Figure 4-142: Comparison of estimated damping coefficient (c_2) with different levels of process noise covariance (Q) of the nonlinear 2DOF model (SNR=50).

Likewise, estimations of structural parameters of a system with sudden stiffness change were carried out. The stiffness in first floor was designed to drop from 100 kN/m to $80kN/m$. The structural parameters, initial values, and noise covariance are same as those in the non-dropped model. Figure 4-143 to 4-148 shows the estimated stiffness and damping coefficient under different external noise levels. It can be found that the proposed filter has the ability to pick up the stiffness and damping coefficient; however, the system with SNR=20 noise does not work well for estimating k_{12} and k_{22}.

Figure 4-149 through 4-154 shows the comparison of estimated results under different levels of measurement noise covariance with fixed process noise covariance $Q = 10^{-7}\mathbf{I}_{10}$ for the model having SNR=20 noise. Figure 4-155 through 4-160 illustrates the results for the case of model with SNR=50 noise. As shown in the figures, a larger measurement noise covariance generates better estimations for the case of the system with SNR=20 noise, but for the system with SNR=50 noise, no significant influence caused by process noise covariance was found.

Figure 4-161 through 4-166 shows the comparison of estimated results under different levels of process noise covariance with fixed measurement noise covariance $R = 1\mathbf{I}_2$ for the model having SNR=20 noise. Figure 4-167 through 4-172 illustrates the results for the model with SNR=50 noise. The figures reveal that the model with SNR=20 noise is sensitive to the selection of process noise covariance and the suggested selection is a small value to Q. The Low noise-added system performs better estimations showing that it is less sensitive to Q so that an arbitrary value of Q can be applied.

In summary, process noise covariance and measurement noise covariance being 10^{-8} and 100, respectively, result in the best estimations, for both constant and time-varying stiffness cases. However, the proposed filter fails to accurately estimate stiffness related to nonlinear terms.

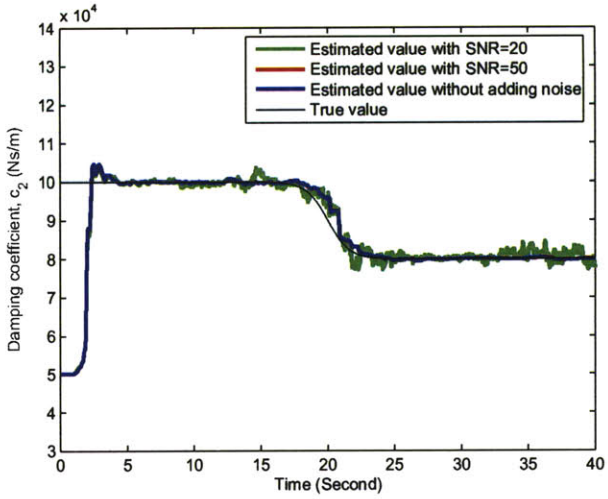

Figure 4-143: Comparison of estimated stiffness (k_{11}) with different levels of noise for the case of stiffness dropping of the nonlinear 2DOF model.

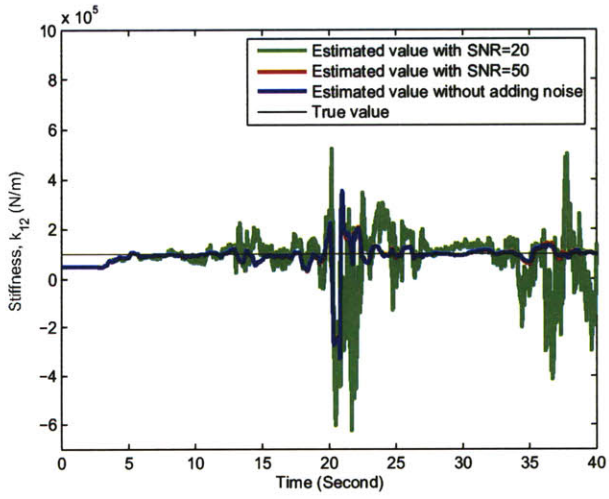

Figure 4-144: Comparison of estimated stiffness (k_{12}) with different levels of noise for the case of stiffness dropping of the nonlinear 2DOF model.

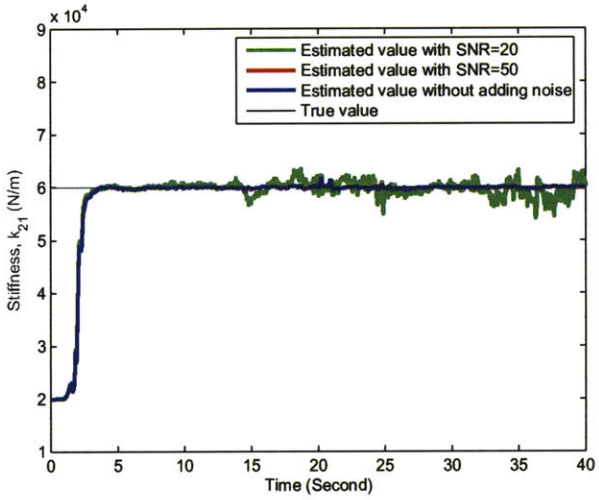

Figure 4-145: Comparison of estimated stiffness (k_{21}) with different levels of noise for the case of stiffness dropping of the nonlinear 2DOF model.

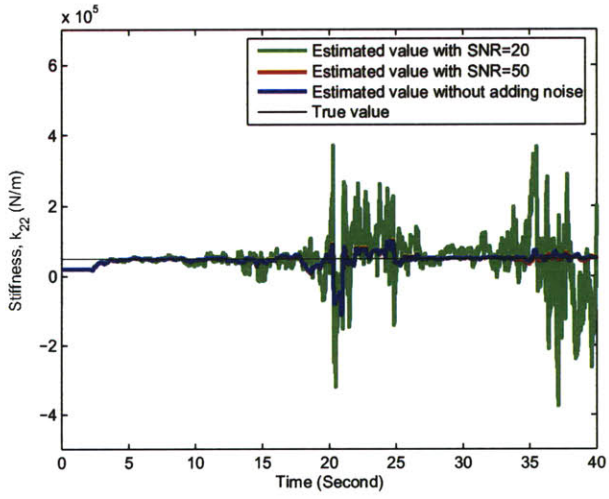

Figure 4-146: Comparison of estimated stiffness (k_{22}) with different levels of noise for the case of stiffness dropping of the nonlinear 2DOF model.

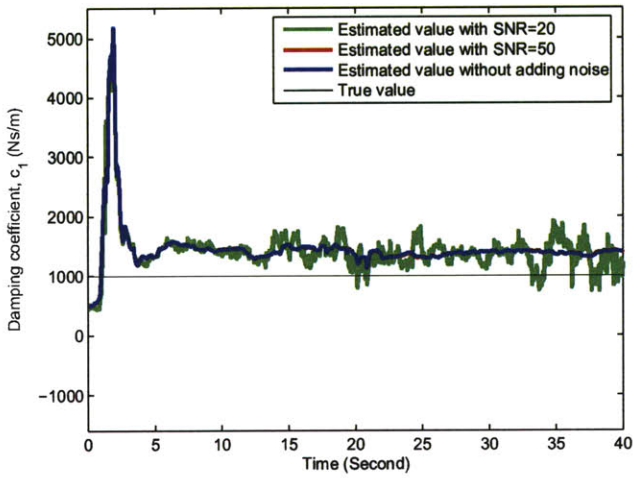

Figure 4-147: Comparison of estimated damping coefficient (c_1) with different levels of noise for the case of stiffness dropping of the nonlinear 2DOF model.

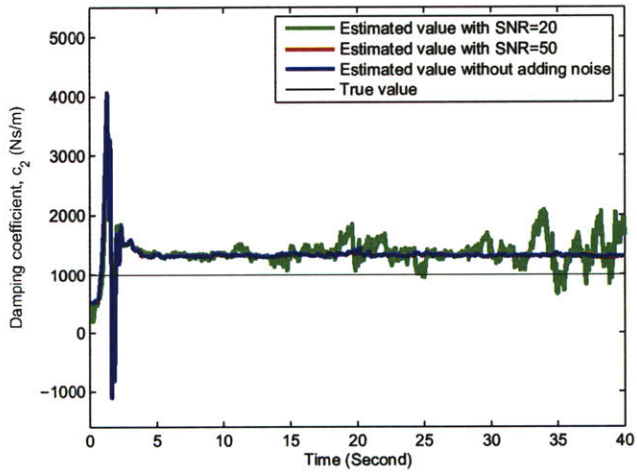

Figure 4-148: Comparison of estimated damping coefficient (c_2) with different levels of noise for the case of stiffness dropping of the nonlinear 2DOF model.

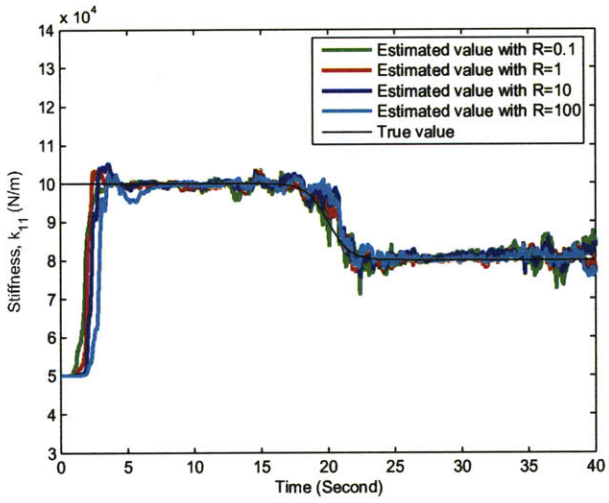

Figure 4-149: Comparison of estimated stiffness (k_{11}) with different levels of measurement noise covariance (R) for the case of stiffness dropping of the nonlinear 2DOF model (SNR=20).

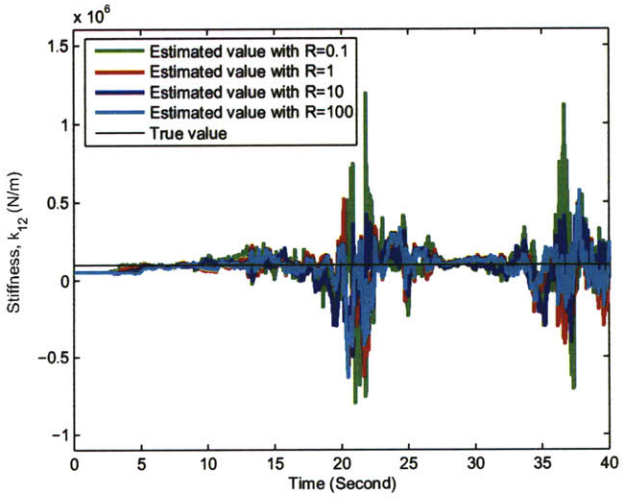

Figure 4-150: Comparison of estimated stiffness (k_{12}) with different levels of measurement noise covariance (R) for the case of stiffness dropping of the nonlinear 2DOF model (SNR=20).

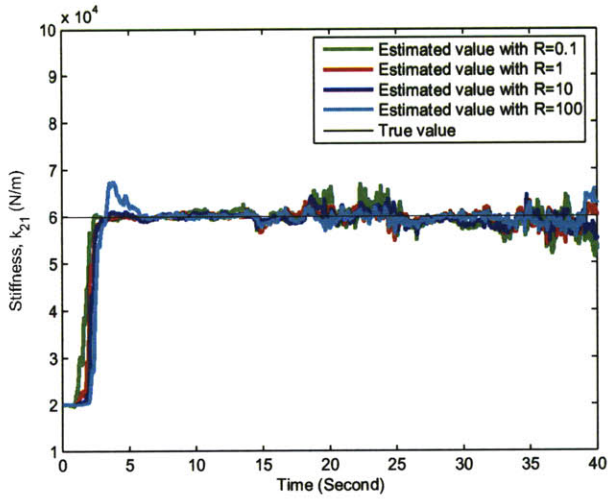

Figure 4-151: Comparison of estimated stiffness (k_{21}) with different levels of measurement noise covariance (R) for the case of stiffness dropping of the nonlinear 2DOF model (SNR=20).

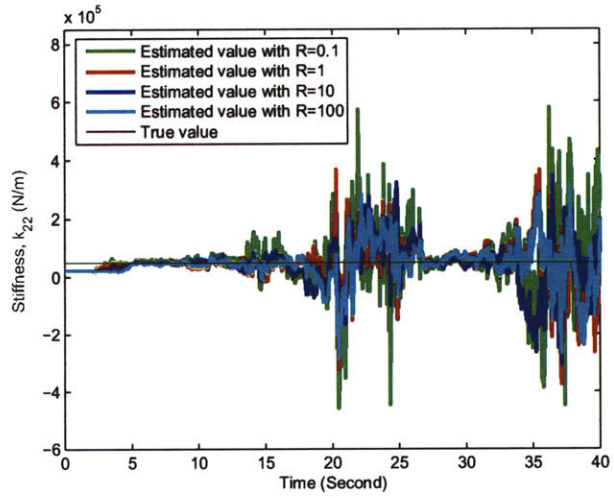

Figure 4-152: Comparison of estimated stiffness (k_{22}) with different levels of measurement noise covariance (R) for the case of stiffness dropping of the nonlinear 2DOF model (SNR=20).

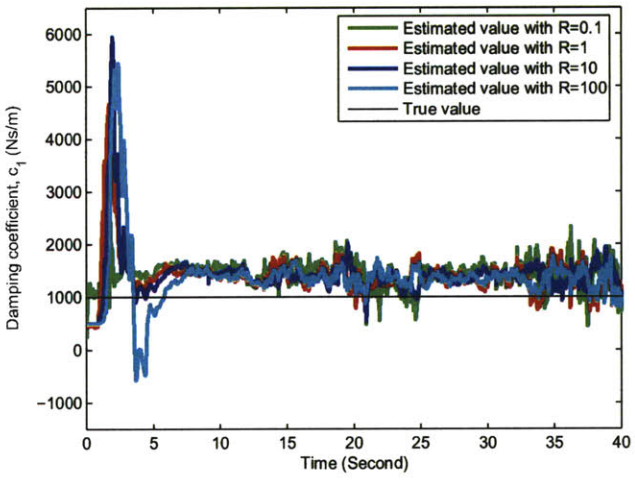

Figure 4-153: Comparison of estimated damping coefficient (c_1) with different levels of measurement noise covariance (R) for the case of stiffness dropping of the nonlinear 2DOF model (SNR=20).

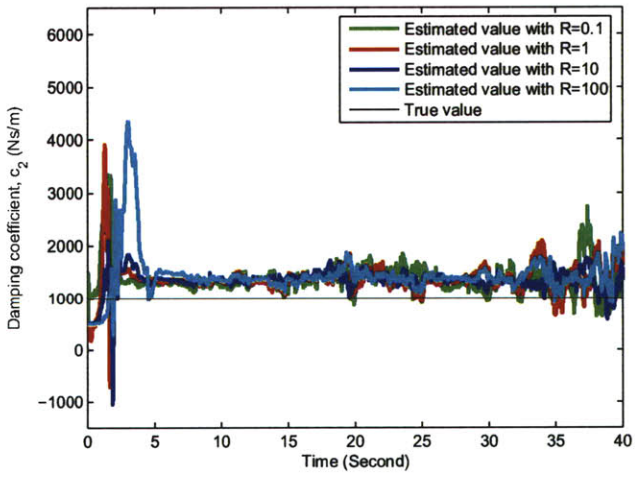

Figure 4-154: Comparison of estimated damping coefficient (c_2) with different levels of measurement noise covariance (R) for the case of stiffness dropping of the nonlinear 2DOF model (SNR=20).

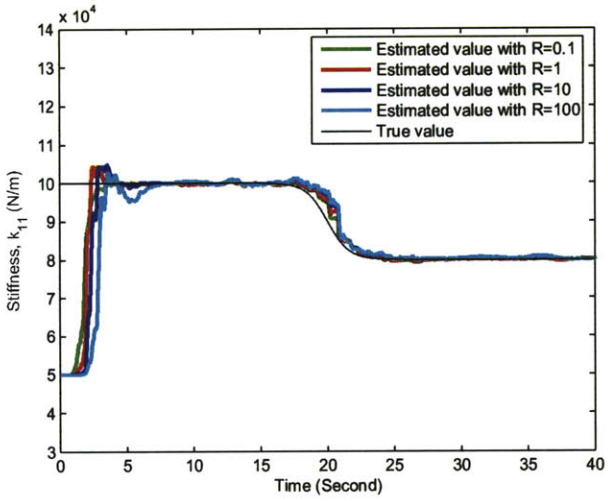

Figure 4-155: Comparison of estimated stiffness (k_{11}) with different levels of measurement noise covariance (R) for the case of stiffness dropping of the nonlinear 2DOF model (SNR=50).

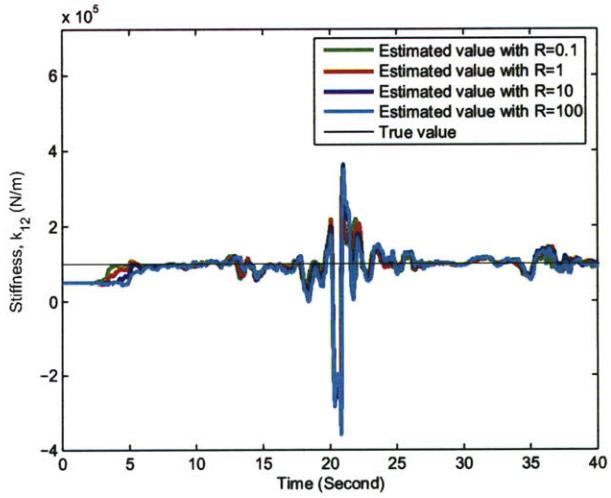

Figure 4-156: Comparison of estimated stiffness (k_{12}) with different levels of measurement noise covariance (R) for the case of stiffness dropping of the nonlinear 2DOF model (SNR=50).

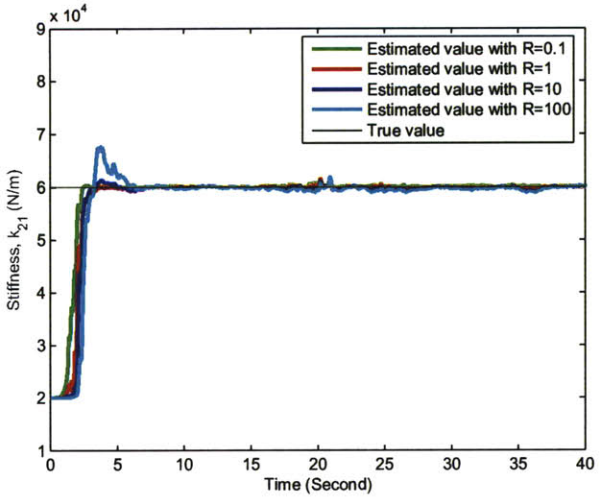

Figure 4-157: Comparison of estimated stiffness (k_{21}) with different levels of measurement noise covariance (R) for the case of stiffness dropping of the nonlinear 2DOF model (SNR=50).

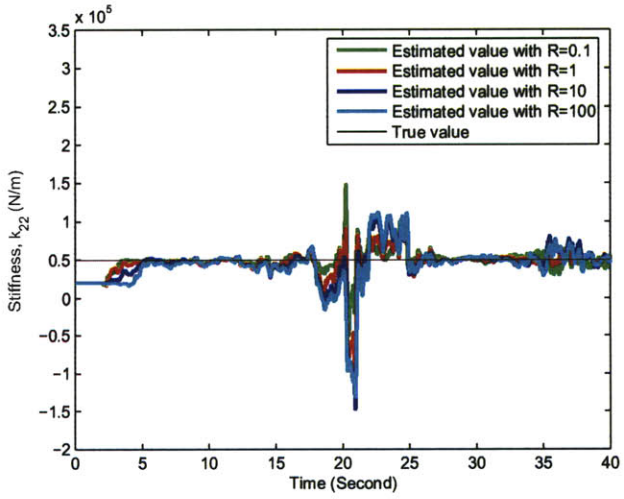

Figure 4-158: Comparison of estimated stiffness (k_{22}) with different levels of measurement noise covariance (R) for the case of stiffness dropping of the nonlinear 2DOF model (SNR=50).

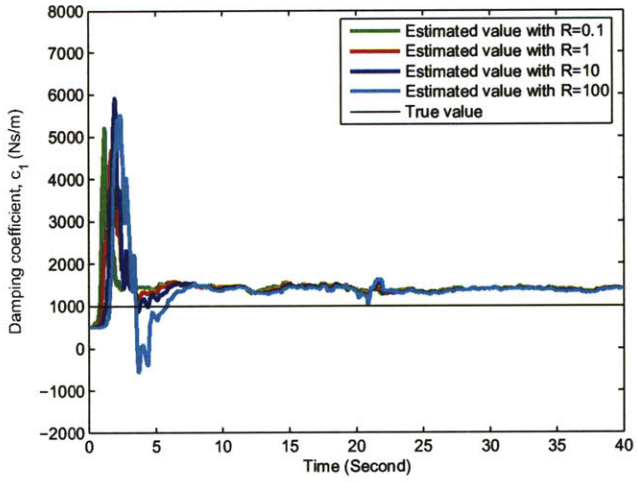

Figure 4-159: Comparison of estimated damping coefficient (c_1) with different levels of measurement noise covariance (R) for the case of stiffness dropping of the nonlinear 2DOF model (SNR=50).

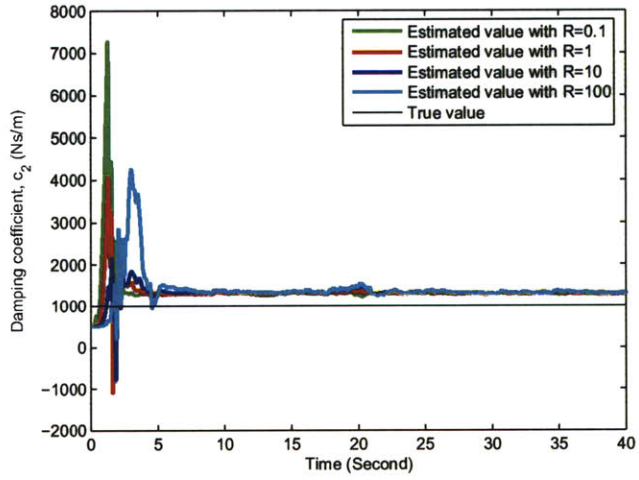

Figure 4-160: Comparison of estimated damping coefficient (c_2) with different levels of measurement noise covariance (R) for the case of stiffness dropping of the nonlinear 2DOF model (SNR=50).

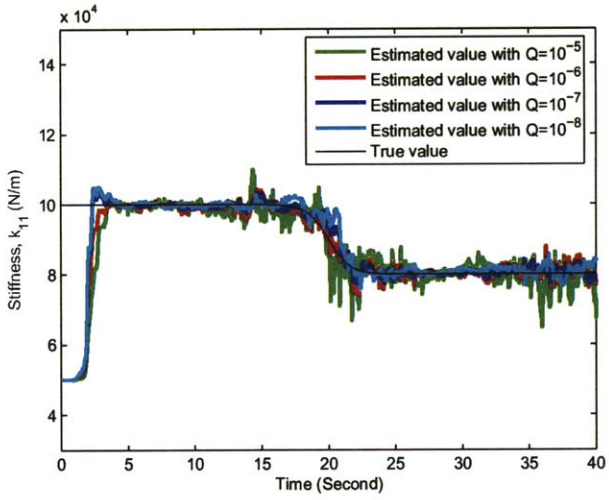

Figure 4-161: Comparison of estimated stiffness (k_{11}) with different levels of process noise covariance (Q) for the case of stiffness dropping of the nonlinear 2DOF model (SNR=20).

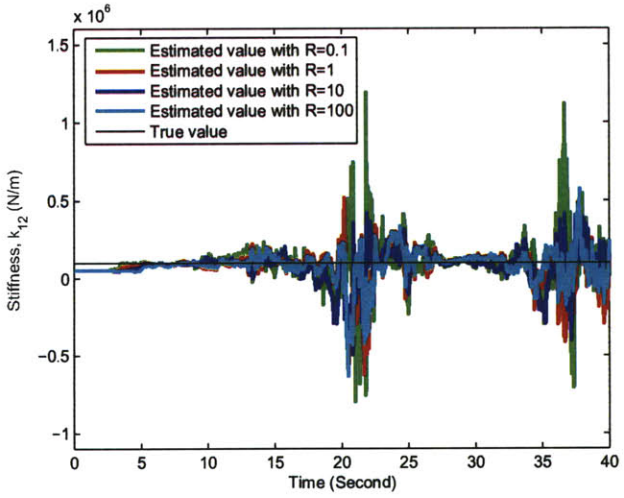

Figure 4-162: Comparison of estimated stiffness (k_{12}) with different levels of process noise covariance (Q) for the case of stiffness dropping of the nonlinear 2DOF model (SNR=20).

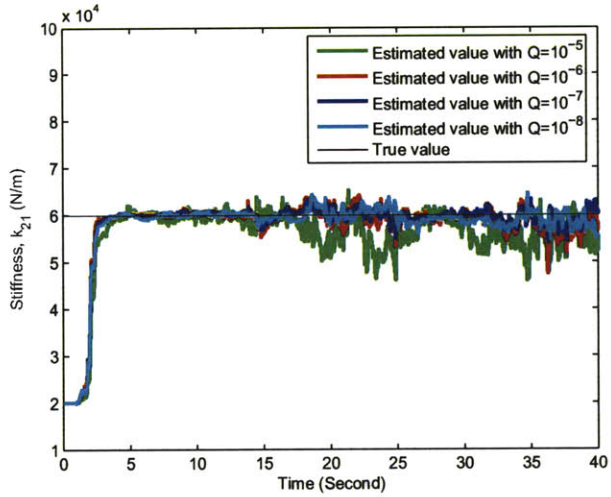

Figure 4-163: Comparison of estimated stiffness (k_{21}) with different levels of process noise covariance (Q) for the case of stiffness dropping of the nonlinear 2DOF model (SNR=20).

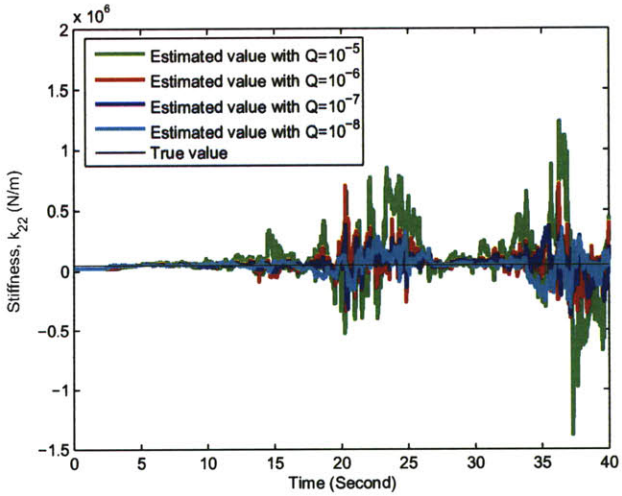

Figure 4-164: Comparison of estimated stiffness (k_{22}) with different levels of process noise covariance (Q) for the case of stiffness dropping of the nonlinear 2DOF model (SNR=20).

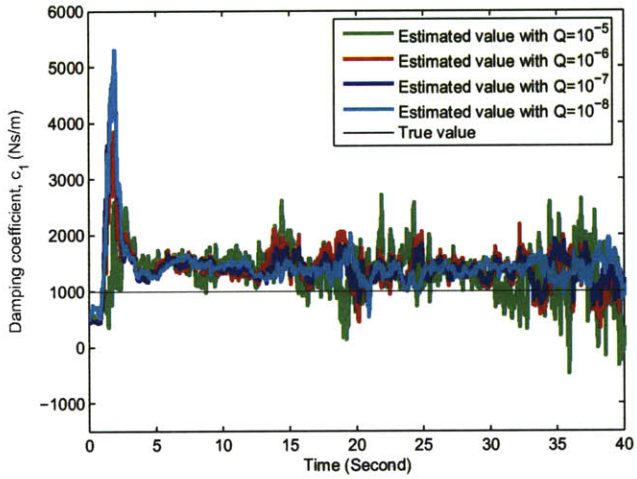

Figure 4-165: Comparison of estimated damping coefficient (c_1) with different levels of process noise covariance (Q) for the case of stiffness dropping of the nonlinear 2DOF model (SNR=20).

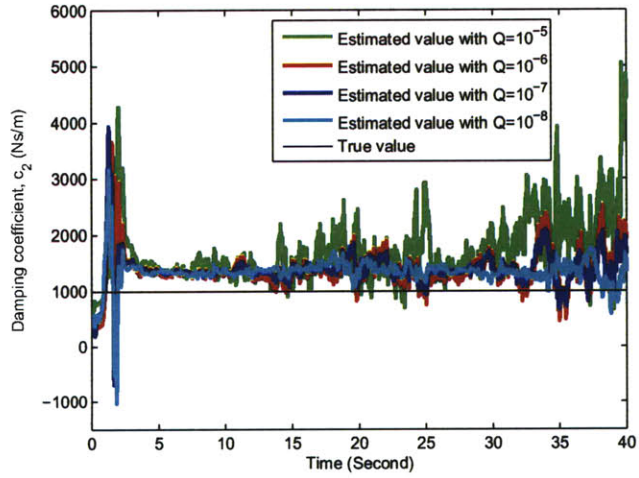

Figure 4-166: Comparison of estimated damping coefficient (c_2) with different levels of process noise covariance (Q) for the case of stiffness dropping of the nonlinear 2DOF model (SNR=20).

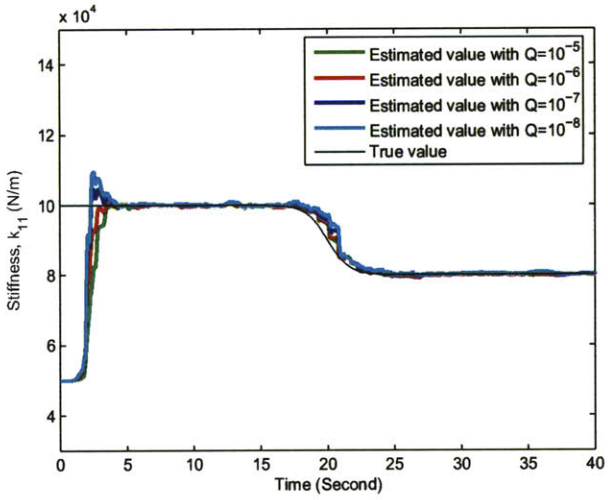

Figure 4-167: Comparison of estimated stiffness (k_{11}) with different levels of process noise covariance (Q) for the case of stiffness dropping of the nonlinear 2DOF model (SNR=50).

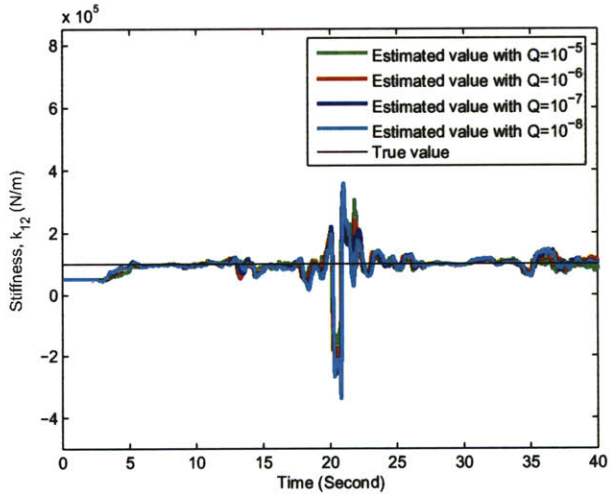

Figure 4-168: Comparison of estimated stiffness (k_{12}) with different levels of process noise covariance (Q) for the case of stiffness dropping of the nonlinear 2DOF model (SNR=50).

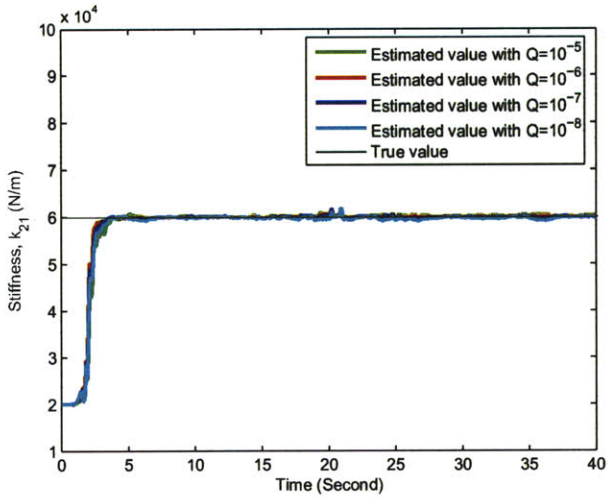

Figure 4-169: Comparison of estimated stiffness (k_{21}) with different levels of process noise covariance (Q) for the case of stiffness dropping of the nonlinear 2DOF model (SNR=50).

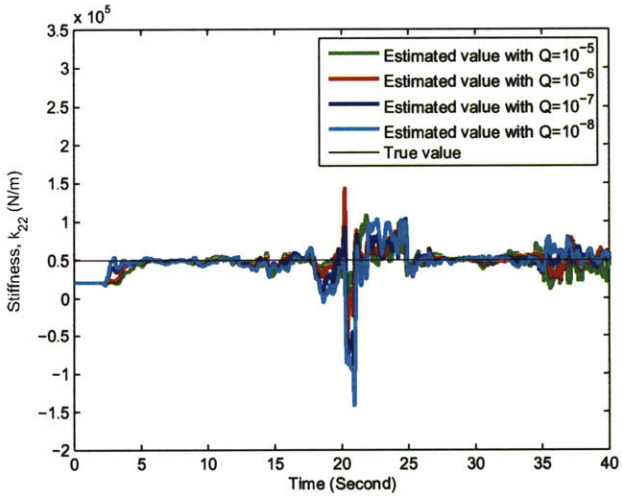

Figure 4-170: Comparison of estimated stiffness (k_{22}) with different levels of process noise covariance (Q) for the case of stiffness dropping of the nonlinear 2DOF model (SNR=50).

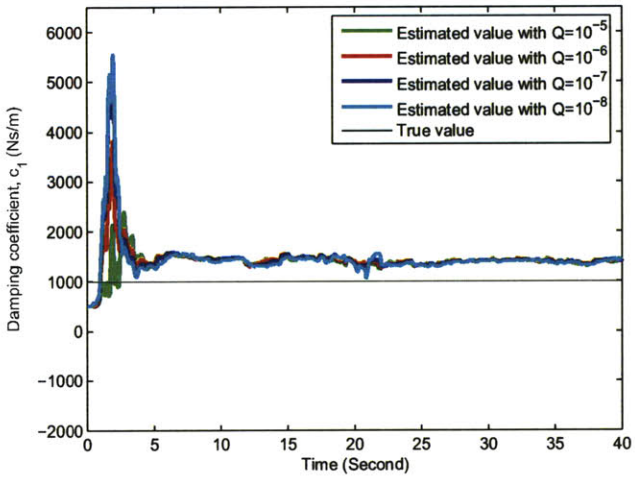

Figure 4-171: Comparison of estimated damping coefficient (c_1) with different levels of process noise covariance (Q) for the case of stiffness dropping of the nonlinear 2DOF model (SNR=50).

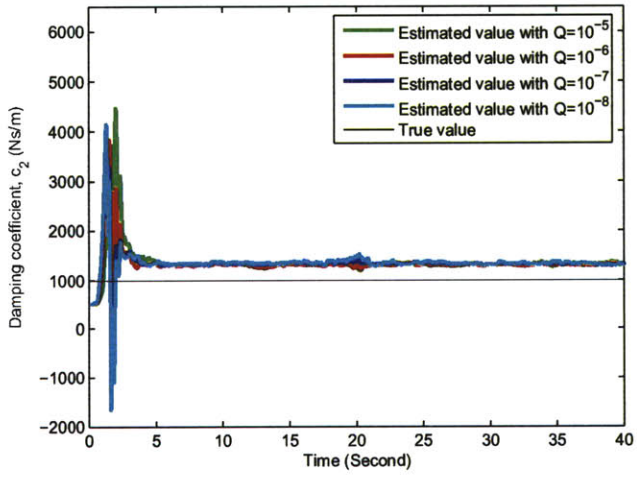

Figure 4-172: Comparison of estimated damping coefficient (c_2) with different levels of process noise covariance (Q) for the case of stiffness dropping of the nonlinear 2DOF model (SNR=50).

4.3 Chapter Summary

The application of the Kalman filter was carried out in this chapter. We implemented the ordinary Kalman filter to estimate the constant structural parameters of a linear SDOF dynamical system, and from the results, it was found that the stiffness is accurately estimated, but there exists a slight overestimation on the damping coefficient. The adaptive extended Kalman filter was utilized to perform estimations on time-varying parameters in a linear and nonlinear structural system. The results reveal that the proposed algorithm works well on estimating linear-related parameters for the dynamical system which has lower level of noise.

Chapter 5

Conclusion and Outlook

Based on the simulation results in Chapter 4, conclusions of this these work were carried out in this chapter along with recommendations on selection appropriate tunable noise covariance. The possible direction for further works related to this research is stated at the end.

5.1 Conclusion

Structural engineers are always taking safety as the primary and most important concern when designing a structure. Not only because civil structures provide living spaces and shelter humans from extreme events, but also because they are involved in the economics and environmental issues. A structure which has self-diagnosis function to provide information about its health condition is desired. To that end, many algorithms were proposed to perform system identification and damage detection in real-time. In this research, an adaptive extended Kalman filter was adopted to evaluate the health of structures. After implementing the proposed algorithm, some conclusions were found as fellows:

- The ordinary Kalman filter works well on estimating constant stiffness in linear structure, but there is a slight overestimation on the damping coefficient. Fortunately, damping is not important when detecting possible damage in structures.

- The adaptive extended Kalman filter is a technique to estimate structural parameters for nonlinear systems and for the system with stiffness change. This method can successfully predict stiffness from low noise-contaminated (2% noise in our case) data. But similarly, it only provides acceptable estimated damping. The simulation results also reveal that this mothod can not provide accurate estimations on parameters related to nonlinear terms.

- High noise-contaminated (5% in our case) data result in inaccurate estimations and a possible reason is because the broad frequency range of the input forces.

- For the cases of simulating damage in a structure, constant parameters have a slight jump when damage occurs. This little jump indicates that some structural parameters may be changed.

- When using the ordinary Kalman filter, the measurement noise covariance and process noise covariance are suggested to be small like on the order of $R = 10^{-1}\mathbf{I}$ and $Q = 10^{-8}\mathbf{I}$.

- The measurement noise covariance and process noise covariance are suggested to be on the order of $10^{2}\mathbf{I}$ and $10^{-8}\mathbf{I}$ for nonlinear systems and systems with time-varying parameters. But for low noise-contaminated system, the noise covariances could be arbitrary numbers.

5.2 Outlook

This section describes future research work relating to the Kalman filter. Accurate estimations rely on the stability of the Kalman filter so that this issue has received attention for a long time. . An incorrect observed measurement will lead to inaccurate estimations, as a result, the estimated parameters can not reflect the true structural behavior. Therefore, making sure the observed outputs are always correct is an issue that requires further research.

This thesis provides a technique to narrow the possible damage locations from

global to local; therefore, in order for the filter to provide accurate results, the local damage detection algorithms should also be to be sufficiently accurate. Existing techniques mostly work for determinate structures only, but civil structures are indeterminate in reality. A complete strategy for detecting damage in a large-scale indeterminate structure is always desired.

Bibliography

[1] M. M. Abdullah, A. Richardson, and J. Hanif. Placement of sensors/actuators on civil structures using genetic algorithms. *Earthquake Engineering and Structural Dynamics*, 30(8):1167–1184, 2001.

[2] H. Asada. Identification, estimation, and learning. Lecture Notes, Department of Mechanics, MIT, February 2009.

[3] O. Büyüköztürk and T. Y. Yu. Structural health monitoring and seismic impact assessment. *5th National Conference on Earthquake Engineering*, May 2003.

[4] J. S. Bendat and A. G. Pierso. *Engineering Applications of Correlation and Spectral Analysis.* Wiley, New York, second edition, 1993.

[5] R. Brown and P. Hwang. *Introduction to Random Signals and Applied Kalman Filtering.* Wiley, third edition, 1997.

[6] K. Chintalapudi, T. Fu, J. Paek, N. Kothari, S. Rangwala, J. Caffrey, R. Govindan, E. Johnson, and S. Masri. Monitoring civil structures with a wireless sensor network. *IEEE Internet Computing*, 10(2):26–34, 2006.

[7] R. A. Collacott. *Structural Integrity Monitoring.* Chapman and Hall, 1985.

[8] S. W. Doebling, C.R. Farrar, M.B. Prime, and D.W. Shevitz. Damage identification and health monitoring of structural and mechanical systems for changes in their vibration characteristics. Report la-13070-ms, Los Alamos National Laboratory, Los Alamos, NM, 1996.

[9] M. F. Elkordy, K. C. Chang, and G. C. Lee. A structural damage neural network monitoring system. *Computer-Aided Civil and Infrastructure Engineering*, 9(2):83–96, 2008.

[10] D. J. Ewing. *Modal Testing: Theory and Practice.* Wiley, New York, 1984.

[11] I. Flood. Simulating the construction process using neural networks. *Proceedings of 7th International Symposium on Automation and Robotics in Construction, ISARC*, 1990.

[12] I. Flood. Solving construction operational problems using artificial neural networks and simulated evolution. *Proceedings of CIB W-55 and W-65 Joint Symposium on Building Economics and Construction Management*, 6, 1990.

[13] C. P. Fritzen, G. Mengelkamp, G. Dietrich, W. Richter, C. Cuerno, J. Lopez-Diez, and A. Güemes. Structural health monitoring of the ARTEMIS satellite antenna using a smart structure concept. *2nd European Workshop on Structural Health Monitoring*, 2004.

[14] J. A. Gubner. *Probability and Random Processes for Electrical and Computer Engineers.* Cambridge University Press, 2006.

[15] J. He and Z. F. Fu. *Modal Analysis.* Butterworth Heinemann, 2001.

[16] N. A. Hoult, P. R. A. Fidler, I. J. Wassell, P. G. Hill, and C. R. Middleton. Wireless structural health monitoring at the Humber Bridge UK. *Proceedings of the Institution of Civil Engineers. Bridge Engineering*, 16(4):189–195, December 2008.

[17] G.W. Housner, L. A. Bergman, T. K. Caughey, A. G. Chassiakos, R. O. Claus, S. F. Masri, R. E. Skelton, T. T. Soong, B. F. Spencer, and J. T. P. Yao. Structural control: Past, present, and future. *Journal of Engineering Mechanics*, 123(9):897–971, 1997.

[18] K. Kahl and J. S. Sirkis. Damage detection in beam structures using subspace rotation algorithm with stain data. *AIAA Journal,*, 34(12), 1996.

[19] R. E. Kalman. A new approach to linear filtering and prediction problems. *Transactions of the ASME–Journal of Basic Engineering*, 82(Series D):35–45, 1960.

[20] R. E. Kalman and R. S. Bucy. New results in linear filtering and prediction theory. *Transactions of the ASME–Journal of Basic Engineering*, 82(Series D):95–108, 1961.

[21] N. V. Kirianaki, S. Y. Yurish, N. O. Shpak, and V. P. Deynega. *Data Acquisition and Signal Processing for Smart Sensors.* Wiley, first edition, 2002.

[22] K. B. Lim. Method for optimal actuator and sensor placement for large flexible structures. *Journal of Guidance, Control, and Dynamics*, 15:49–957, 1992.

[23] J. W. Lin and R. Betti. On-line identification and damage detection in non-linear structural systems using a variable forgetting factor approach. *Earthquake Engineering and Strucutral Dynamics*, 33(4):419–444, 2004.

[24] T. K. Lin, Y. L. Chu, K. C. Chang, C. Y. Chang, and H. H. Kao. Renovated controller designed by genetic algorithms. *Earthquake Engineering and Structural Dynamics*, 38(4):457–475, 2009.

[25] P. L. Liu. Identification and damage detection of trusses using modal data. *Journal of Structural Engineering*, 121(4):599–608, 1995.

[26] C. H. Loh, C. Y. Lin, and C. C. Huang. Least-squares estimation with unknown excitations for damage identification of structures. *Journal of Engineering Mechanics*, 126(7):693–703, 2000.

[27] Jr. V. Lopes and S. da Silva. Semigroups of recurrences. In Lopes Jr. V. Inman D. J., Farrar C. R. and Steffen Jr. V., editors, *Damage Prognosis for Aerospace, Civil and Mechanical System*, chapter 8, pages 177–199. Wiley, 2005.

[28] L. Ludeman. *Random Processes- Filter, Estimation, and Detection.* Wiley, 2003.

[29] J. P. Lynch. An overview of wireless structural health montitoring for civil structures. *Philosophical Transactions of the Royal Society of London, Series A, Mathematical and Physical Sciences*, 365(1851):345–372, 2007.

[30] J. P. Lynch, A. Sundararajan, K. H. Law, and A. S. Kiremidjian. Embedding algorithms in a wireless structural monitoring system. *Proceedngs of International Conferences on Advances and New Challenges in Earthquake Engineering Research*, August 2002.

[31] J. P. Lynch, A. Sundararajan, K. H. Law, A. S. Kiremidjian, E. Carryer, H. Sohn, and C. R. Farrar. Field validation of a wireless structural monitoring system on the alamosa canyon bridge. *SPIE's 10th Annual International Symposium on Smart Structures and Materials*, August 2003.

[32] O. Maruyama and M. Hoshiya. System identification of an experimental model by extended Kalman flter. *Proceedings on Structural Safety and Reliability, ICOSSA*, 2001.

[33] Paul E. Mix. *Introduction to Nondestructive Testing.* Wiley, second edition, 2005.

[34] J. Paek, K. Chintalapudi, R. Govindan, J. Caffrey, and S. Masri. A wireless sensor network for structural health monitoring: performance and experience. *Proceedings of the 2nd IEEE Workshop on Embedded Networked Sensors*, pages 1–9, 2005.

[35] A. K. Pandey and M. Biswas. Damage detection in structures using changes in flexibility. *Journal of Sound and Vibration*, 169(2):3–17, 1994.

[36] M. Papatheororou, C. A. Talor, and N. A. J. Lieven. Optimal sensor locations for dynamic verification. *The 4th European Conference on Structural Dynamics*, pages 587–592, June 1999.

[37] J. S. Pei, C. Kapoor, T.S. Graves-Abe, Y. P. Sugeng, and J. P. Lynch. An experimental investigatopn of the data delivery performance of a wireless sensing unit designed fo structural health monitoring. *Structural Control and Health Monitoring*, 15:471–504, 2008.

[38] D. J. Pines and P. A. Lovell. Conceptual framework of a remote wireless health monitoring system for large civil structures. *Smart Materials and Structures*, 7(5):627–636, 1998.

[39] Y. Qian and A. Mita. Acceleration-based damage indicators for building structures using neural network emulators. *Structural Control and Health Monitoring*, 15:901–920, 2007.

[40] D. E. Rumelhart, G. E. Hinton, and R. J. Williams. *Learning Internal Representations by Error Propagation.* MIT Press, Cambridge, MA, USA, 1986.

[41] D. Simon. Kalman filter. *Embedded System Programming*, pages 72–79, 2001.

[42] S. Soyoz and M. Q. Feng. Instantaneous damage detection of bridge structures and experimental verification. *Strucutral Control and Health Monitoring*, 15(7):958–973, 2008.

[43] Jr B. F. Spencer, M. E. Ruiz-Sandoval, and N. Kurata. Smart sensing technology: opportunities and challenges. *Structural Control and Health Monitoring*, 11(4):349–368, 2004.

[44] E.G. Straser and Kiremidjian A.S. A modular visual approach to damage monitoring for civil structures. *Proceedings of SPIE v2719, Smart Structures and Materials*, pages 112–122, 1996.

[45] N. Tomonori and B. F. Jr. Spencer. Structural health monitoring using smart sensors. Technical Report NSEL-001, Newmark Structural Engineering Laboratory, Department of Civil and Environmental Engineering, University of Illinois at Urbana-Champaign, November 2007.

[46] K. Tribikram. *Advanced Ultrasonic Methods for Material and Structure Inspection.* ISTE, 2007.

[47] F. Wong, A. Tung, and W. Dong. Seismic hazard prediction using neural nets. *Proceedings of 10th World Conference on Earthquake Engineering*, pages 339–343, 1992.

[48] Q. Xia, M. Rao, Y. Ying, and X. Shen. Adaptive fading Kalman filter with an application. *Automatica*, 30(8):1333–1338, 1994.

[49] J. N. Yang, S. Lin, H. W. Huang, and L. Zhou. An adaptive extended Kalman filter for structural damage identification. *Structural Control and Health Monitoring*, 13:849–867, 2006.

[50] J. N. Yang, S. Pan, and S. Lin. Least-squares estimation with unknown excitations for damage identification of structures. *Journal of Engineering Mechanics*, 133(1):12–21, 2007.

[51] I C. Yeh. Design of high-performance concrete mixture using neural networks and nonlinear programming. *Journal of Computing in Civil Engineering*, 13(1):36–42, 1999.

[52] L. Zhou, S. Wu, and J. N. Yang. Experimental study of an adaptive extended Kalman filter for structural damage identification. *Journal of Infrastructure Systems*, 14(1):42–51, 2008.